2017

Shear Induced Fiber Alignment and Acoustic Nanoparticle Micropatterning during Stereolithography

Doruk Erdem Yunus
Lehigh University

Shear Induced Fiber Alignment and Acoustic Nanoparticle Micropatterning during Stereolithography

by

Doruk Erdem Yunus

Presented to the Graduate and Research Committee

of Lehigh University

in Candidacy for the Degree of

Doctor of Philosophy

in

Mechanical Engineering

Lehigh University

August 2017

Approved and recommended for acceptance as a dissertation in partial fulfillment of the requirements for the degree of Doctor of Philosophy

Doruk Erdem Yunus

Dissertation Title: Shear Induced Fiber Alignment and Acoustic Nanoparticle Micropatterning during Stereolithography

_____

Date

_____

Dissertation Director: Dr. Yaling Liu

_____

Accepted Date

Committee Members:

_____

Committee Chair: Dr. Yaling Liu

_____

Dr. Alparslan Oztekin

_____

Dr. Brandon Krick

_____

Dr. Chao Zhou

ACKNOWLEDGMENTS

Above all, I want to express my sincere appreciation to my respected advisor, Prof. Yaling Liu. Not only did he provide his continuous support for my Ph.D. studies, but he also patiently helped and guided me in my analytic thinking, scientific writing, and academic pursue. His enthusiasm and hands-on experience in research helped and motivated me significantly. His accessibility, precise forethoughts, and willingness to help made my studies and dissertation possible.

I would also like to thank to all of my doctoral committee members, Prof. Chao Zhou, Prof. Brandon Krick, and Prof. Alparslan Oztekin. I am very grateful for their precious time, valuable advices, consideration, and encouragement.

I also appreciate Mrs. JoAnn Casciano, Mrs. Allison Marsteller, Mrs. Barbara McGuire, and Mrs. Jennifer Smith for their dedicated work, assistance, and kindness. Countless thanks to all of my lab mates and friends, Dr. Jifu Tan, Dr. Anthony Thomas, Dr. Shunqiang Wang, Dr. Yihua Zhou, Mr. Ran He, Mr. Wentao Shi, Mr. Salman Sohrabi, Mr. Christopher Uhl, Mr. Onur Denizhan, and Mr. Orhan Kaya for their cooperation, contributions, moral support, and friendship.

Last but not least, I would like to thank to my family and dedicate this work to them, my beloved wife Jaharah Yunus, my parents Samira Koc and Semseddin Yunus, my sister Gurbet Ozge Mert. Without their tremendous support, encouragement, and continuous patience, my education for over 20 years would not be possible.

TABLE OF CONTENTS

LIST OF FIGURES

ABSTRACT

The stereolithograpy method, which consists of a light source to polymerize the liquid photocurable resin, can produce structures with complex shapes. Most of the produced structures are unreinforced neat pieces. The addition of reinforcement, such as fibers and particles are regularly utilized to improve mechanical properties and electrical conductivity of the printed parts. Added fibers might be chosen as short or continuous fibers and the properties of the reinforced composite materials can be significantly improved by aligning the fibers in preferred directions. The first aim of this dissertation is to enhance the tensile and flexural strengths of the 3d printed composites by using shear induced alignment of short fibers. The second aim is to print parts with conductive embedded microstructures by utilizing acoustic patterning of conductive particles. Both aims are utilized during the stereolithography process.

A lateral oscillation mechanism, which is inspired by large amplitude oscillatory shear test, was designed to generate shear flow. The alignment method, which combines the lateral oscillation mechanism with 3d printed wall patterns, is developed to utilized shear flow to align the fibers in the patterned wall direction. Shear rate amplitude, fiber concentration, and patterned wall angle were considered as parameters during this study.

The stereolithography device incorporated with oscillation mechanism was utilized to produce short fiber reinforced ceramic composites and short nanofiber reinforced polymer composites. Nickel coated short carbon fibers, alumina and silica short fibers were used to reinforce the ceramic matrix with different fiber contents. The printed walls were demonstrated to align the short fibers parallel to the wall which was different from the oscillation direction up to 45°. The flexural strength of the ceramic

matrix was improved with the addition and alignment of the short fibers. The alumina nanofibers were used as reinforcement in the photocurable polymer resin. The alumina nanofibers were treated with a silane coupling agent to improve interfacial bond between alumina fibers and polymer resin matrix. The aligned specimen demonstrated improvement in tensile strength with increasing nanowire content and their alignment.

A hexagon shaped acoustic tweezer was incorporated into the stereolithography device to pattern conductive micro- and nanoparticles. This new approach for particle microstructuring via acoustic aligning during the stereolithography was used to produce embedded conductive microstructures in 3d printed parts. The acoustic tweezer was used to pattern the conductive particles into horizontal, 60°, and 120° parallel striped lines. The influence of the particle percentage content onto the electrical resistivity and thickness of the patterned lines were also investigated for different materials such as copper, magnetite, and carbon fiber. The copper patterns show less resistance to electrical currents compare to magnetite and carbon nanofiber patterns. Additionally, the influence of the particle concentration to the height of the pattern was studied and the data was utilized to achieve conductivity along z-axis. Later, this approach was used to fabricate examples of embedded conductive complex 3D microstructures.

Chapter 1: Introduction

1.1 Background and Motivation

Additive manufacturing (AM) techniques have been promising and valuable for solving the design diversification and customization problems of conventional methods. The implementation of the techniques allowed the users to complete different iterations and adjustments of the design quickly, whereas it would typically be completed in months by traditional methods. The option of adding materials selectively and conveniently when they are needed will eventually reduce the waste and cost of the parts. Ultimately, industrial designers will design products digitally with computer aided design (CAD), later to be acquired, modified, and produced with personalized 3d printers by users.

Recently, the concept of personalized factory in every home has become more feasible. Commercial or custom-made desktop 3d printers are readily available for the user to produce their digital models. Currently, the most commonly used material is thermoplastics, but recently professional quality production devices with more material options such as, thermosetting polymers, ceramics, and metals have been developed. However, these devices are still restricted by the lack of quality materials. Material option limitations are much greater for AM compared to conventional methods [1].

Since the beginning of 1980's, many AM methods have been established. Over the last thirty years, these methods have been named: freeform fabrication, additive

processing, rapid manufacturing, additive manufacturing, additive fabrication, direct digital manufacturing, etc. [2]. However, most of these methods produce parts with relatively low mechanical strength which makes them not suitable for high strength purposes [3]. As a result, more complex parts and structures, with applications through wide-ranging industries such as medical [4], electronics [5-7], and composites [8, 9] have gained significant attention from researchers.

The addition of fiber and particle reinforcement into the 3d printed polymer during fused deposition modeling (FDM) [8, 10], stereolithography (SLA) [11, 12], ink-jet printing [13] was successfully used for fabrication of reinforced polymer composites (RPC). For example, ink-jet printing has the capability of printing multiple materials (up to 14) in a single build [14]. Ink-jet printing, which is a fairly new variation of AM, also has advantages in scalability and material mixing, in addition to better surface finish and speed. Shear-induced alignment of fiber reinforcement is readily available for FDM and inkjet printing. Short fiber alignment along the extrusion direction is partially obtained as a result of shear, which is generated during flow through the nozzle [8, 10, 13]. However, FDM does not generate preferred surface finish and is a significantly slower method in contrast to SLA and Ink-jet printing. However, the FDM extruding and ink-jet heads are prone to clogging and the addition of reinforcement increases the possibility of clogging in the nozzle. Therefore, alternative options for alignment and manipulation of fiber or particulate positions can solve the related problems of FDM and ink-jet methods.

The short fiber alignment during SLA was demonstrated by electrical field [15-17] , magnetic field [11], and acoustic field [12]. However, using magnetic or electric fields require the material of the reinforcement to have specific magnetic and electrical

properties. In contrast, acoustic field can be used for fiber and particle manipulation, alignment, and microstructuring without too many material limitations [12, 18-20]. The acoustic field is a useful method to distribute and pattern particles towards pressure nodes or anti-nodes in the matrix medium. Although, acoustic radiation forces arrange the fibers in the form of strands of long parallel lines, increased fiber volume concentration causes the individual fibers to have a higher amount of misalignment [21]. While acoustic alignment is a good option for micropaterning and microstructuring with unique acoustic patterns, flow-induced alignment can be a good alternative for better fiber distribution and alignment without material limitations during SLA manufacturing.

1.2 Aim and Scope

The aim of this dissertation is to investigate new methods to produce composite parts with improved strength or functionality by employing SLA as an additive manufacturing technique. Two methods were focused to achieve the aim. The first method is shear-induced alignment of fibers via lateral horizontal shaking device, which is inspired by large amplitude oscillatory shear test. The second method is acoustic microstructuring of electrically conductive particles to fabricate embedded micro wire patterns.

The main objective of shear induced alignment method is to develop an approach to enhance and tailor mechanical properties of the 3D printed parts without reinforcement material limitations forced by the technique to align the fibers during SLA. The second objective of the method is the produce polymer and ceramic composites with aligned fibers to investigate flexural strength (See Ch. 3) and tensile strength (See Ch. 4) enhancements by the suggested method. The main objective of the acoustic micro

patterning is to produce parts embedded with electrically conductive wire structures. The second objective of this approach is to investigate the conductivity achieved with different materials and line widths (See Ch. 5).

1.3 Additive Manufacturing

3D printing or additive manufacturing has become mainstream, even for people not directly involved with the industry and research. As a result, cheaper and more common forms of 3D printing are entering in domestic settings. However, 3D printing and additive manufacturing refer to a big spectrum of different technologies and methods. A standard definition of AM technologies to include all these methods and technologies is define by ASTM as "the process of joining materials to make objects from 3D model data, usually layer upon layer, opposed to subtractive manufacturing methodologies, such as traditional machining" [22]

The most important benefits of AM can be listed as [23]:

- Provides more freedom and flexibility during design, optimization, and innovation
- Has a smaller environmental footprint because it generates less waste and consumes less electricity
- Provides better date and time predictions, therefore enhances the production flexibility and time management
- Reduces production costs by eliminating the required tools and makes production of low quantity specialized production cheaper and more feasible

1.4 Additive Manufacturing Methods

Although there are several AM methods, they all follow some essential processes. For example, 3D objects which will be produced need to be designed in a 3D engineering CAD software, such as SOLIDWORKS®, CATIA®, AutoCAD®, PTC Creo®. These professional engineering programs provide tools to simulate assembly, mechanical strength, and can also convert the model to an STL file. STL files describe a standardized file format for AM consisting of triangulated surface representation by approximating the model's surface features in a 3D Cartesian coordinate system. The STL file is uploaded to AM software to be sliced into a G-code format which is made up of lines in 3D Cartesian coordinate system to instruct the 3d printer. The 3d printer deposits the material layer by layer based on G-code data until the model is completed. After the completion of the build process, some of AM techniques may require post processing methods to increase mechanical strength of the completed piece [24].

Currently there are seven additive manufacturing process classifications. These processes are binder jetting, directed energy deposition (DED), fused deposition modeling (FDM), inkjet printing, selective laser sintering (SLS), laminated object manufacturing (LOM), and stereolithography (SLA). These categories can be distinguished more by the materials, dimensional accuracy or the energy sources.

The SLA systems use a process of photopolymerization by an ultraviolet (UV) light source to cure photosensitive liquid resin in a layer by layer fashion. Normally, high-speed mirror galvanometers are operated to guide the UV light beam across the liquid polymer resin surface by following the direction of the G-code generated by AM software. When a layer is cured, the platform is moved as much as the desired thickness

of the next layer and the same process is repeated until the whole piece is finished. A motorized wiper can be utilized to generate uniform layer thickness. After the completion of the process, the excess resin should be rinsed away with isopropyl alcohol or ethyl alcohol. If the support structures exist, they should be removed. Finally, the piece should be post-cured in a suitable UV light oven to complete the curing process [25]. The SLA systems provide better quality and surface finish compared to the FDM systems, however removal of the piece from the platform or removal of the support structures can be difficult and the manufactured part can be damaged [26].

The SLS systems use a high power CO_2 laser to melt the powder, which is spread along a flat base with desired thickness. The CO_2 laser follows the direction of the G-code generated by the AM software to generate the patterned shape. The melted powder particles fuse together to generate a sintered solid object. When a layer pattern is sintered, a rolling mechanism spreads the next layer of meltable powder onto the previous one and then the same method is repeated until the whole model is sintered together. The SLS system is similar to the SLA system, except the requirement of the support structure. The unmelted powder holds the sintered parts in position and acts as a support. The parts may require sanding if a specific surface roughness is desired. However, the SLS system uses a very powerful laser which requires high power and the surface finish is not as good as the SLA system [26].

FDM is a material extrusion based AM system which uses an extruding mechanism with a hot-end nozzle to deposit thermoplastic polymer material as a layer on a building platform. The hot-end nozzle heats the thermoplastic filament into a softer semi-liquid state as the extruding mechanism pushes the filament through the hot nozzle

to be deposited on the platform surface. While filament is deposited on the surface, XY stage follows the G-code and patterns the desired shape for each layer. After the new layer hardens and bonds to previous layer, Z-axis moves the platform for the next layer [24]. The post-processing consists of separating the support structure from the solid model and some dimensional netting, such as sanding and honing. The FDM process is slow and not precise compared to some other AM techniques, but it is cheaper and easier to change materials in use with some other options [26].

The LOM method of AM was founded by the Helisys Inc. in 1985 [24]. In contrast to other methods, The LOM process starts with an adhesive coated thin plastic or paper sheet. The sheet is heated and bonded on the surface with a roller and paper is cut and shaped by a laser. The excess part of the sheet is removed after shaping and the next sheet is bonded to the previous layer. This process continues until the model is complete. The completed pieces are generally finished by polishing and sanding for desired surface finish [26]. Despite being relatively inexpensive and fast even for large volumes, extensive post-processing after the completion of the layer stacking requires the model to be well designed [27].

1.5 Applications and Progress

Because of the good precision of the completed pieces and the enhancement of the efficiency during automation practices, AM has been used in numerous industries. The spread of CAD software at the end of 20^{th} century enabled the progress of AM technology to infiltrate into these industries [26]. While new methods are emerging and existing technologies are evolving, the applications of additive manufacturing also continue to grow. For example, NASA used FDM method to produce more than 70 parts

of the mars exploration rover [28]. Piper Aircraft replaced CNC machined parts of their hydroforming device with 3d printed ones to reduce production costs and material surplus during their personal jet manufacturing line [29]. The SLA process was utilized in the medical field to save time and cost for the custom prototyping of cranioplasty [30]. There are many other industries where AM processes have been used for method and process development, such as jewelry [31], electronics [32], automotive [33], and biomedical [34].

Research interest and attention for expanding industry applications of AM resulted with further progress in AM methods themselves and new approaches. He et al. [35] developed a efficient and economical method to produce micro-wavy pattern, such as herringbone [36] by using direct image lithography and a model to calculate grayscale Gaussian distribution. He et al. [37] also used similar model for developing a method of dual projection to manufacture circular microfluidic channels. The particle transport, deposition, and binding test results during the study compliments with the literature expectations [38-42] and demonstrates the practicality of the fabrication method. Optimization studies of 3d model orientation [43] and G-code algorithms [44] also improve build time and accuracy. Development of hybrid CNC/AM system, which combines CNC and FDM techniques, is a useful progress for functionality and optimized build time [45]

1.6 Stereolithography

Hull [46] described the SLA system as a system which consists of a laser, a liquid resin VAT, a platform, and a computer to produce solid 3D objects from a photosensitive liquid medium (see Fig 2-1). Similar approaches of 3D printing have suggested the use

of photomask and injection or spraying liquid resin droplets delivery systems during the process [47, 48]. During these suggested systems, after deposition of a layer by light source, the platform is moved by the layer thickness to create necessary space for next layer.

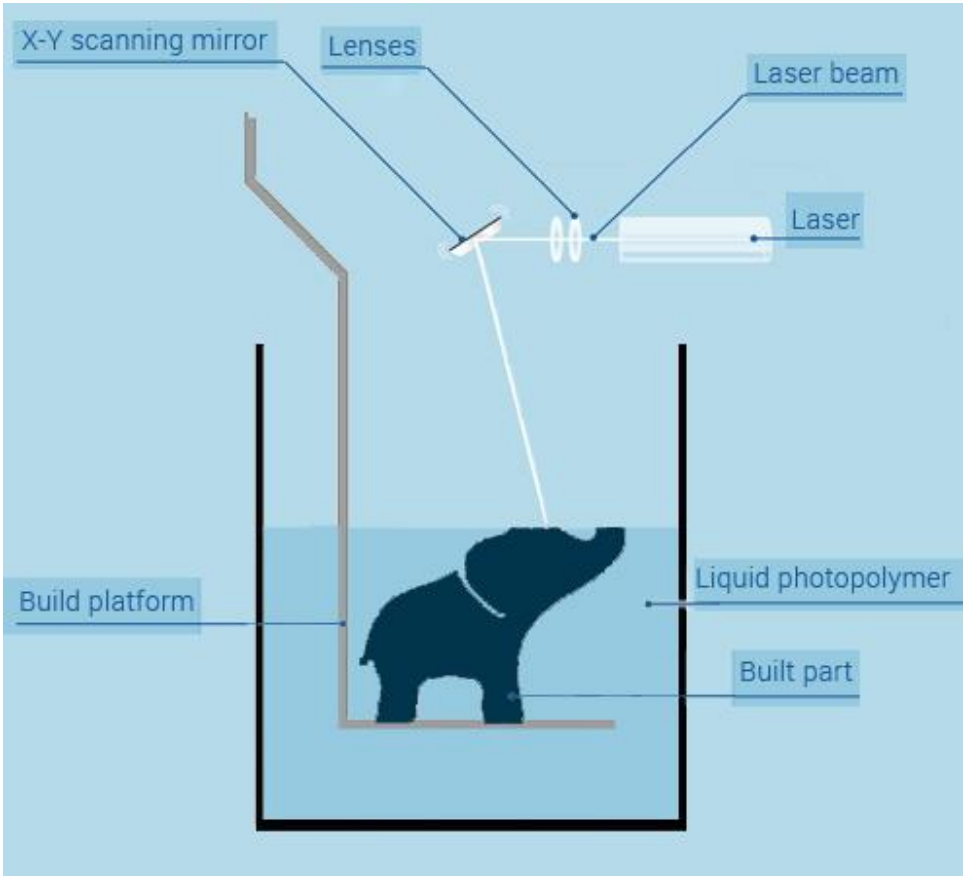

Figure 1-1 Schematic illustration of mirror-based top down SLA machine

The projection based SLA AM method has been utilized in these studies. In 1992, Jacobs explained important parameters of the process, such as curing depth, light energy distribution, X-Y scanning speed, width of curing [49]. These equations also apply to other slightly different methods, including Projection based SLA [50, 51] and Scanning-Projection based SLA [52, 53], and etc.

1.6.1 Curing Mechanism of Polymer Resins

Photopolymerization is typically a complex chemical reaction which uses a radiation source to solidify polymeric materials. Various industries such as coating, adhesive, and additive manufacturing make use of photo sensitive materials because of their optical and chemical properties [54].

Free radical photoinitiation (FRPI) and cationic photoinitiation (CPI) are two general and different mechanisms [55]. While CPI is generally related with epoxy monomer applications, FRPI is mainly related with acrylate monomer applications. Photoinitiation processes consist of initiation, propagation, and termination for both mechanisms [56]. In all three studies of this dissertation, acrylate monomer systems were used.

An acrylate monomer system consists of acrylate monomers, photo-initiator, and UV dye. The photo-initiator is added into the resin to absorb the photon and release free radicals. Free radicals initiate polymerization process by breaking the acrylate monomer's carbon-carbon bonds leading to polymerization and crosslinking. This process, which occurs from the absorption of the photon to the start of the polymerization, is called the initiation process. Acrylate systems are much more reactive to the initiation by radicals than cationic systems, as a result acrylate materials crosslinks much faster than epoxy solutions [55]. The initiation process is followed by the propagation step, which is a chain reaction between activated acrylate monomers and other monomers/cross-linkers. The termination step follows the propagation step when the chain reaction is stopped by combination of two radicals. Additionally, oxygen inhibits the polymerization process by reacting with the free radicals and forming

peroxides. This feature of oxygen is used in bottom up SLA system to separate cured layer from the bottom of the VAT [57].

Cationic resin systems contain cationic form of photoinitiator which splits into a free radical and a cation when exposed to photons. The cation parts start the polymerization and crosslinking process and build the final crosslinked structure which is desired. However this process is much less reactive compared to FRPI systems and usually it is not effected by the oxygen [58]

1.6.1.1 Free Radical Photopolymerization

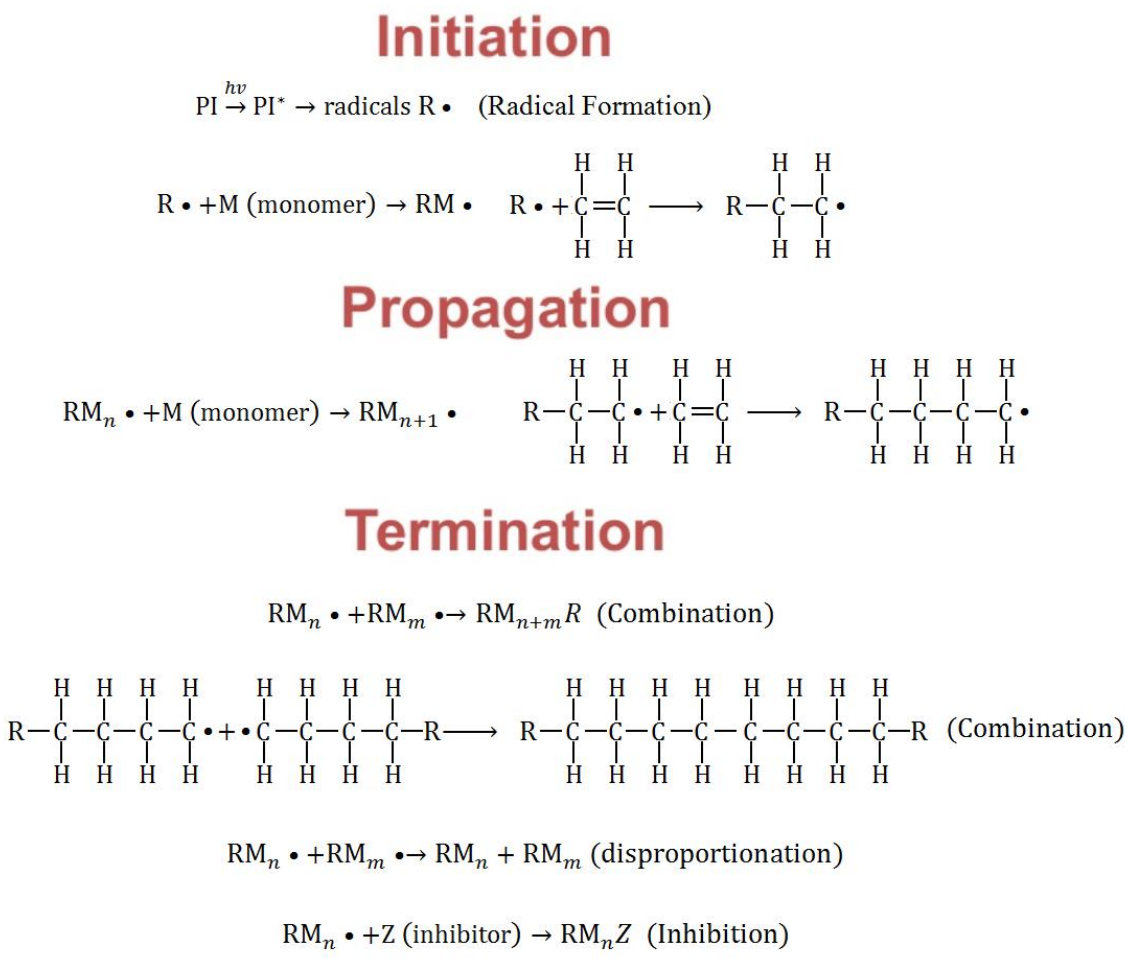

Figure 1-2 Schematic illustration of the free radical polymerization process.

The stereolithography method started the use of acrylate monomer resin which is exothermic free radical photopolymerization system [59]. Initiation, propagation, and termination are the fundamental stages of this free radical photopolymerization process (see Fig 1-2). At the initiation stage, photons from the light source are absorbed by the photoinitiator; as a result of this absorption, photoinitiator generates free radicals (R •). Then, free radicals activate the chain reaction by bonding with the monomers (M). If there is oxygen in the environment, generated free radicals bond with existing oxygen molecules to form inactive peroxides. The polymerization does not progress to propagation stage, until all oxygen or similar inhibition molecules are consumed by free radicals. A sufficient level of light exposure (E*) is required to overcome such a inhibition effect [57].

The propagation stage starts at different locations where the radicals are initiated. The radicals expand to a macroradical and then resin turns into a crosslinked gel at the location of the light exposure. As the polymerization continues, the gel becomes more viscous. The propagation stage is generally terminated by recombination, disproportionation, and inhibition. Inhibition is commonly observed where exposure to oxygen occurs, such as thin films and top surface of liquid resin. Oxygen diffuses into the liquid resin and hinders the initiation stage and existing radicals [60].

Monomer conversion during free radical photopolymerization is known to be a low degree reaction. The completion of the polymerization by post curing is a requirement for high strength applications. The parts, which are produced by SLA system, have a certain degree of shrinkage based on the material. The shrinkage of the parts without sufficient amount of mechanical strength can cause distortion and cracking

of the pieces. Distortion, cracking, and shrinkage can be calculated and prevented by model optimization [61].

1.6.1.2 Cationic Photopolymerization

Triarylsulfonium and diaryliodonium are most commonly used onium salt for cationic photopolymerization. When light is exposed to triarylsulfonium, the photodecomposition process starts with photolysis of a Bronsted acid, which is a catalyst for epoxide polymerization. The cationic photopolymerization began with photo-induced protonation of epoxide group and progress by a chain reaction. However, the polymerization process is not terminated instantaneously and it can last many hours or even days [62, 63].

1.6.2 Light Absorption

The SLA system works by curing liquid resin layer by layer based on polymerization of the resin by absorbed light on the surface of the liquid. The absorption of light on the surface is defined by the Beer-Lambert Law which defines the correlation between curing thickness, light penetration distance, energy of the light exposure per surface area, and exposure threshold of the resin [35, 64]. The exponential gradient of the curing profile is provided by The Beer-Lambert law as:

$$C_d = D_p \ln(E/E_c) \tag{1.1}$$

where C_d is the curing thickness, D_p is the light penetration distance of the monomer system, E is the energy of the light exposure on the surface of the liquid resin, and E_c, is the exposure threshold of the monomer system.

The distribution of energy for an emitted light is not uniform due to dimensional aberrations, optical scattering, spatial inconsistencies, and light distortions. As a result, emitted light will get diffused and forms a quasi-Gaussian distribution [65]. Fig. 1-3 demonstrates the curing profile and light energy distribution for ideal and actual situations.

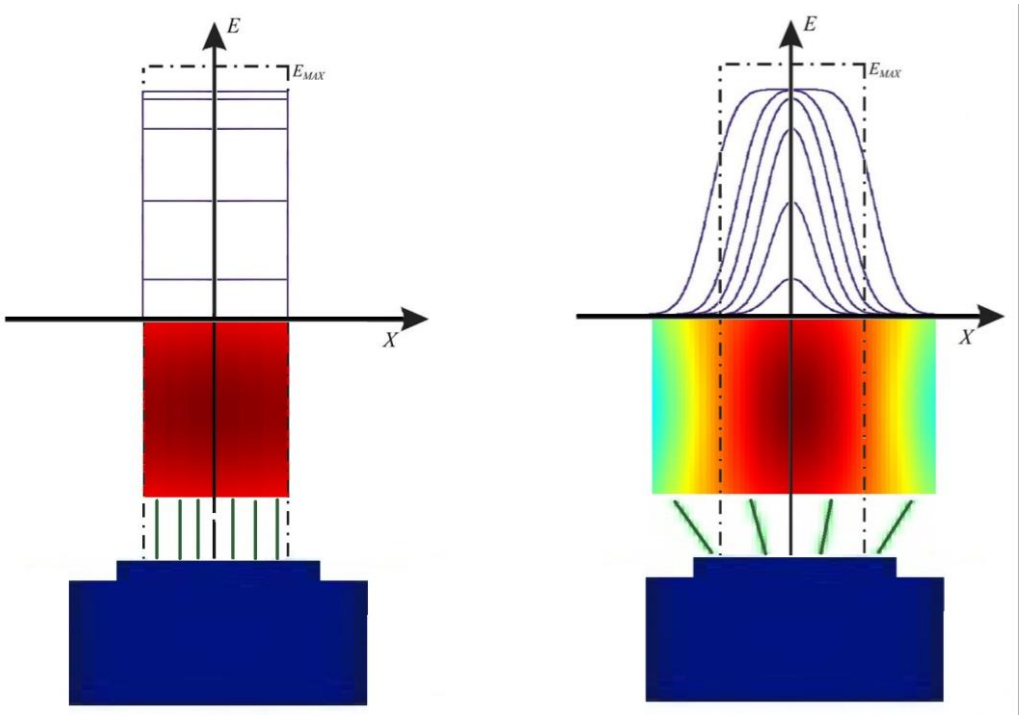

(a) (b)

Figure 1-3 Schematic drawing of curing profile and the light energy distribution: (a) Ideal case without diffusion, (b) Quasi-Gaussian distribution

1.7 Material selection for Additive Manufacturing

Majority of the AM systems are dedicated on the rapid prototyping polymers, ceramic, and metals. Similarly, enhancing abilities of these systems in the sense of material quality, cost of the process, dimensional accuracy and production speed is the main objective of many research studies. Manufacturing particle or fiber reinforced

composite parts by mixing the reinforcement with the AM material to improve many properties; such as mechanical, electrical, and thermal properties is the topic of those research studies [66-70]. Additive manufacturing of ceramic reinforced polymer composites have also inspired additive manufacturing of ceramic materials. Nowadays, most of the fabrication of ceramic using AM starts with 3d printing green pieces which consist of 50-60% ceramic particle and 40-50% remaining polymer. These polymer/ceramic composite pieces are processed by sintering in high temperature to remove polymer material and bond the ceramic particles together.

1.7.1 Composite Fabrication

Today, the innovations in AM methods gave opportunity to progress in AM of composite materials. AM techniques which have been utilized for composites production are fused deposition modeling [71], selective laser sintering[72], laminated object manufacturing [73], direct ink writing [8, 74], and stereolithography [75, 76]. Most of the time, these methods are utilized for composite production in order to enhance mechanical properties of polymer matrix which is most available additive manufacturing material.

1.7.1.1 Fused Deposition Modeling of Composites

FDM method is the cheapest method of additive manufacturing. As a result, it was one of the earlier methods to be employed for composite additive manufacturing. Reinforcement can be incorporated by using a reinforced thermoplastic filament. Carbon black and carbon fiber are most commonly used reinforcement during FDM process. Carbon black is mainly used as reinforcement for its electrical conductivity. Carbon black particle reinforced polycaprolactone (PCL) was utilized for electronic sensor manufacturing by Leigh et al. [5] as a cost effective electrically conductive material.

They used a commercial desktop FDM device to extrude a conductive filament with 15wt% filler content.

Shofner et al. [77] prepared short carbon fiber reinforced Acrylonitrile-butadiene-styrene (ABS) filaments suitable for the FDM method. They utilized Banbury mixing method to achieve uniform mixing and dispersion of short fiber reinforcement into ABS polymer. The mixed material was granulated and extruded as a filament to use during FDM process. The results of the study demonstrate the alignment of the fibers in the extrusion direction as a result of the shear generated by the flow through the hot nozzle. However, short fiber reinforcement of the material in FDM method reaches its optimum properties around 5wt% short fiber content and further improvement of the content increases the filament buckling failures and discontinuities [9, 78]. Using continuous fiber as the reinforcement was suggested as a solution to this issue by Matsuzaki et al. [71]. The method suggested allows deposited layer to contain 40-50% fiber content.

1.7.1.2 Selective Laser Sintering of Composites

The SLS process can utilize the composite powder mix of reinforcement filler and matrix material to fabricate composite materials. Kenzari et al. [72] mixed 30% quasicrystal filler with 70% nylon particles to use as the raw material for SLS method. They produced leak-tight quasicrystal reinforced polyamide based composite with enhanced friction and wear resistance properties.

1.7.1.3 Laminated Object Manufacturing of Composites

Klosterman et al. [73] used LOM process to manufacture glass fiber reinforced epoxy polymer composite by using composite sheets instead of laminated 2d sheets. They utilized the vacuum bagging method to finalize the process. The method can

achieve 1% dimensional accuracy in X-Y axis and 8% accuracy in Z axis due to lamination and vacuum bagging process. The method uses laser to shape the layer, therefore surface quality of the produced parts is reduced by edge burning.

1.7.1.4 Direct Ink Writing of Composites

This method is very similar to the FDM process. DIW devices extrude colloidal inks while FDM extrude quasi-liquid thermoplastic melt. Deposited layers can be cured by photopolymerization [79], evaporation [74], or thermal curing [8]. The method was used to build different forms of composite examples, such as carbon nanotube reinforced polymer nanocomposite microcoils [80], ceramic reinforced polymer nanocomposites [79], locally aligned cellulose fiber reinforced hydrogel composite [81], multiwall carbon nanotube reinforced conductive nanocomposite [74], high resolution composite scaffold made of polylactic acid (PLA) and calcium phosphate [82].

Before DIW method starts, direct ink material mix should be ready to use except the devices with multiple extrusion heads. Multi-nozzle systems can produce parts with different composition by depositing different material with different amounts independently [83]. This method is capable of producing composites with higher filler content and more complex structure, however its resolution is limited by the extrusion head and ink properties [79].

1.7.1.5 Composite Stereolithography

The SLA system can easily produce composite parts by adding suitable reinforcement into liquid photocurable resin for enhancing required material properties. Based on the desired enhancement, short fiber or particle can be used as the reinforcement. Short fiber reinforcement is used commonly for SLA composite

applications to enhance the mechanical strength of the polymeric composite [11, 21, 75]. Nano-scale reinforcement addition into photocurable polymeric resin can also be used in structural or functional applications to increase mechanical, electrical, and/or thermal properties of manufactured pieces by SLA [64, 76, 84]. Different reinforcement material options were demonstrated to work for composite fabrication by SLA, such as carbon fiber [85] , glass fiber [75], silica [84], alumina [86], cellulose [76], and barium titanate [87].

The properties of resin, reinforcement, and their mixture, such as aspect ratio of the reinforcement, surface functionalization, concentration of the reinforcement have significant impact on the rheological properties of the liquid resin. Reinforcement concentration has significant influence on the viscosity of the resin and its influence becomes more important at high volume fraction applications including ceramic composites due to low fluidity of the resin [75, 85]. Aspect ratio and the concentration of the reinforcement have substantial effect on the mechanical properties of the composite materials. In optimal volume fractions, fiber reinforcement with proper aspect ratio can increase flexural and tensile strength, when agglomeration is prevented and fibers are well dispersed [84, 88]. However, the improvements which can be achieved by low volume fractions are not adequate for the applications of current composite industry. A solution for viscosity issue of the high solid loading is using a viscosity modifier to increase the fluidity. A diluting agent has been used in photocurable resins to achieve 10-40% solid loading with adequate viscosity by researchers [89-91]. Goswami et al. [90] achieved up to 40 vol% solid loading of alumina by using decalin as a diluent with TH2080 monomer and by ball milling the slurry for 5h.

Surface functionalization or interface modification is another important parameter which effects functionality and material properties of the composites. McCall et al. [87] chemically treated surface of BTO nanoparticles to achieve better mechanical-to-electrical conversion in photocurable resin with 10 wt% BTO nanoparticles and CNTs. Chiu et al. [92] used silane treatment to modify the surface of the bamboo fiber for reinforcement of polyester diacrylate photolithography resin. The treatment resulted with an increase in surface hardness of the composite, tensile strength, and fracture strain of the composite.

1.7.2 Ceramic Fabrication

Ceramic fabrication by additive manufacturing technique contains 3 different stages: slurry preparation, production of green part, and sintering. The AM method commonly used to produce green parts consist of selective laser sintering [93], fused deposition modeling [94], binder/ink jetting [95], laminated object manufacturing [96], and stereolithography [97]. The process of green part fabrication depends on AM process chosen for fabrication, however, most of the methods include sintering stage which polymeric binder removed and ceramic particles bonded together.

1.7.2.1 Selective Laser Sintering of Ceramics

The SLS systems are mainly used for metallic fabrication due to their capabilities to handle residual stress cause by thermal gradients. If the system is used for ceramics, accumulated inner stresses consequently results with crack development in the fabricated piece. One of the suggested approaches to prevent crack development during fabrication is reducing thermal gradients by heating the ceramic powder to a higher temperature (e.g. 1600°C) before using the laser to melt the particles together [93]. This method releases

inner mechanical stresses considerably as result of reduction of the thermal gradients. However, if the deposition of ceramic powders for the next layers is done with cool powders instead of preheated ones, it can still cause crack development in the ceramic layer.

1.7.2.2 Fused Deposition Modeling of Ceramics

These methods based on the approach of depositing the ceramic particle and thermoplastic polymer mixture via extrusion through hot nozzle and fast solidification of the quasi-liquid melted polymer. Ceramic filled thermoplastic filament can be mixed prior to the whole process [94, 98] or simultaneously with the extrusion [99]. Scheithauer et al. [99] formulated the mixture simultaneously with the deposition process by mixing stainless steel and zirconia powders with thermoplastic binder at 100°C. The system was depositing the prepared mixture onto a platform heated to 80°C temperature.

Binder removal and sintering can provide finished pieces with density reaching close to 99% of the bulk density of the ceramic. A similar approach called Freeze Form Extrusion Fabrication (FEF)[100] extrudes aqueous based alumina paste and solidifies the paste immediately after the deposition of the paste on the surface layer by layer. This process can support bigger build size and higher volume fraction of the ceramic fillers with density up to 98% of bulk density.

1.7.2.3 Binder/Ink Jetting of Ceramics

The ink-jet approach of ceramic fabrication uses pre-ceramic polymer precursor which can derive ceramic material or ceramic suspension which polymer binder can be removed. Mott et al. [95] used pre-ceramic polymer precursor, which can derive silicon carbide by pyrolysis, to fabricate silicon carbide parts. Ceramic production with ink jet

printing has more material options, but volume concentration of the ceramic particles is limited due to the viscosity issues. Due to the viscosity issues, Ebert et al. [101] used only 27 vol% of solid loading for their zirconia suspension during their ink-jet printing of dental applications.

Binder jetting method is a similar application to the ink-jet method. While ink-jet printers deposit a ceramic suspension or pre-ceramic polymer precursor, binder jetting devices deposit a liquid binder on a ceramic powder mixture. The binder jetting approach can reach the same density of the ceramic powder mixture used. By adding apatite–wollastonite glass powder as a reinforcement into hydroxyapatite powder which is a mineral form of calcium apatite, Suwanprateeb et al [102] enhanced the mechanical properties of composite prosthetic bone implant, such as flexural modulus and strength produced with binder jetting.

1.7.2.4 Laminated Object Manufacturing of Ceramics

The LOM technique is used by Gomes et al. [96] to produce green parts by using ceramic laminates as the process layers. They used water-based ceramic powder suspension to form a ceramics laminate, which was the raw material of the LOM ceramic method. Ceramic laminates were shaped by laser and bonded on the previous layers with adhesive agent solution. However the method wastes big amount of the ceramic laminates without achieving a good finish surface.

1.7.2.5 Stereolithography of Ceramics

In a similar way with composite fabrication via stereolithography, dense green part for ceramic fabrication can be printed by adding ceramic powders into photocurable polymeric resin. SLA approach can produce parts with better resolution, surface, and

functional structures, such as ceramic based scaffold [103, 104]. As it was mention in section 1.7.1.5, during SLA process with high volume fraction of additive particles, a diluent can be used to reduce the viscosity of the suspension [90]. It is very common to use deionized water to lower the viscosity of the slurry; however fabricated green body has low mechanical strength when aqueous ceramic slurry is used. Resin based ceramic slurry has higher mechanical strength as a green part, but the viscosity needs to be reduced with diluent such as decalin [90] and colloidal silica [97].

Other possible solutions for viscosity are using wiper blade or casting mechanism to spread the highly viscous ceramic slurry as a uniform layer [105-107] or using UV-active preceramic monomer for SLA of ceramic [108, 109]. Wiper blade and casting mechanisms require much bigger devices compare to the building platform. Preceramic monomer for ceramic production can produce much better mechanical properties compared to other slurry options; however it can only fabricate Si-based ceramic parts.

Chapter 2: Literature Review: Fiber Alignment and Acoustic Particle Patterning

2.1 Short-fiber Composites

Fibers, which can be synthetic or natural materials with high aspect ratio, are extensively used to reinforce composites. The addition of fibers is used to enhance mechanical, thermal, and electrical properties of the matrix material. They are also used in a wide range of applications as a result of their strength and durability. Conventional materials, such as metal components are substituted by fiber composite materials in many industries including transportation, construction, aerospace, and electronics.

2.1.1 Mechanical Properties

The material properties of the composites are based on matrix material, fiber material, fiber length, fiber orientation, and the interfacial strength between fiber and matrix. Even though continuous fibers are much more suitable as reinforcement for mechanical property improvement, short fibers can achieve similar properties if higher aspect ratio fibers are used with the right volume fraction [110]. Higher short fiber content enhances the properties of the composite, but it limits the fabrication and post-processing. Surface modification can help by improving inter-layer bonding and viscosity adjustments [75, 111]. The influence of short fibers are based on the their distribution and orientation in the mixture of fiber and matrix [110]. Therefore, to approach similar level

to the continuous fiber reinforcement, orientation and length of the short fiber needs to be considerably controlled and optimized [112].

The force distribution in a composite during an applied force is relative to the specified material. The relation between carried stresses by a fiber and matrix and applied forced is defined as "Rule of Mixture". "Rule of Mixture" is a weighted mean which estimates properties of composite materials [113].

$$E_c = fE_f + (1 - f)\,E_m \tag{2.1}$$

where f is the fiber volume fraction, E_m is the material property of matrix, E_f is the material property of fiber, and E_c is the material property of composite.

When a composite material is exposed to an external force, internal and external stresses are generated on that composite material. Especially the tips of the fibers develop stresses as a result of the shear load on the interfacial region in between the fiber and matrix.

The material strength of the composite parts are determined by the volume fraction of the fiber, fiber aspect ratio, the length and diameter of the fibers, failure strain and their relationship [114]. During the directed carbon fiber preforming method, it has been reported that the fiber orientation is effected by fiber length and tow size [115]. The study shows that increased fiber length provides greater alignment and larger tow size increases the alignment because of restricted movement of the fibers due to increases in weight of the fiber with larger tow [115]. Increased concentration of the internal stresses at the edges of fibers, short fiber length should be optimized to sustain the applied forces on the composite material and provide the necessary flexibility to the fibers for the manufacturing process [116].

2.1.2 Fiber Length Distribution

The short fiber reinforced composites will not have comparable tensile and flexural strength to the continuous fiber reinforced composites due to the shear stress concentration at the tips of the fibers [113, 117, 118]. In contrast, Young's modulus and stiffness of the short fiber and continuous fiber reinforced composites are similar. Microscopy inspection showed that cracks at the tip of the fiber will progress further into the matrix. However, better shear yielding and shear fracture along the fiber direction was demonstrated at the interfacial region between fiber and matrix when shear band was extended at the tips of the short fiber [119]. Higher aspect ratio of the fiber will cause larger internal shear stresses and failure. As a result, short fiber reinforced composites bears less loads when the shear stress profile is not completely developed along the fiber length.

Continuous fiber reinforced composites are more labor intensive than its short fiber counterpart, therefore short fiber reinforced composite are usually quicker and cheaper [120]. The short fiber reinforced uncured resins have increased drapability which is defined as the tip deflections ratio per minute, thus they can be used to produce more complex shapes with reduced longitudinal modulus.

2.1.3 Fiber Volume Fraction

When compared the neat matrix material, short fiber reinforced composites have increased material properties. In the studies of Fu et al. [114], the optimum mechanical strength was achieved with 25% volume fraction of the aligned short carbon fiber reinforced polypropylene composite with the fiber length longer than 800 μm. The minimum volume fraction which provides any improvement of the desired property is

called the critical volume fraction (CVF) [121]. CVF describes the minimum value of volume fraction of short fibers which is required for them to transport the applied force with a low percentage of the inner stress applied to the matrix [113]. While CVF is required for any improvements, a high fiber volume fraction can cause an opposite effect on the material properties [114, 115, 122]. This is mainly caused by fiber end initiated failure and might be prevented by increasing the length of the short fibers [123].

2.1.4 Fiber Alignment Methods

The short fibers inside the matrix can be aligned or randomly orientated. Randomly orientated short fibers provide high drapability. Material properties of randomly orientated composites can be very variable [115, 121], while aligned fiber reinforced composites provide regularly good mechanical properties [114, 124, 125]. Alignment of the short fibers is essential for approaching the mechanical properties of that exhibited by the continuous fiber reinforced composites.

Determination of the fiber alignment in a composite material requires careful examination for position, distribution, and orientation of the fibers. The location of the elliptical cross-section to the reference x-y-z axis is commonly used to calculate the degree of fiber alignment. In Figure 2-1, θ shows the orientation angle of the defined fiber with respect to z axis, while ϕ shows the orientation angle with respect to x-z plane. θ and ϕ angles with the fiber length are all that is required to define the 3D orientation of a fiber [126].

Figure 2-2 shows the depiction of the elliptical cross-section of the fiber model, which can be used to calculate the angle ϕ of misalignment, compared to the fiber with the alignment of the vertical θ angle [111].

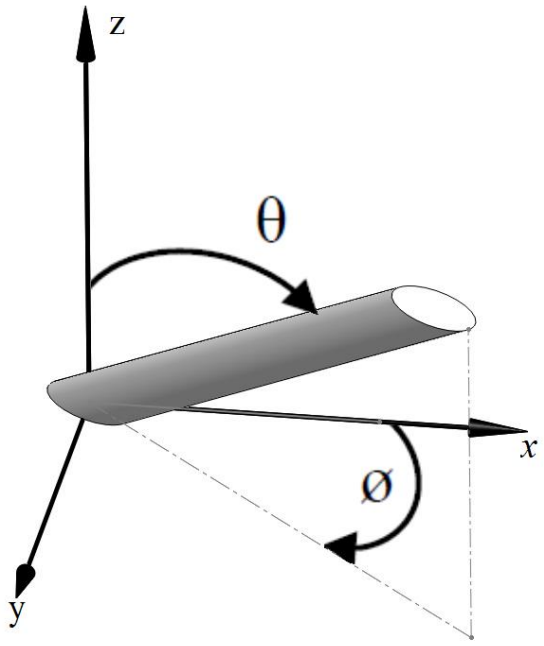

Figure 2-1 Description of the fiber alignment with θ and Ø angles to the z-axis

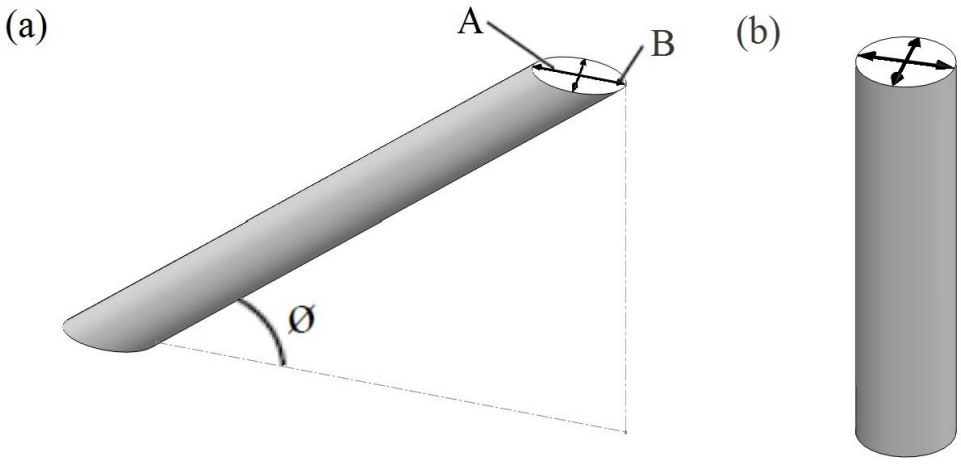

Figure 2-2 Schematic illustration of misaligned and aligned fibers; (a) demonstrates a misaligned fiber with a misalignment angle of Ø. A and B are the radiuses of the elliptical cross-section of the fiber, (b) a vertically aligned fiber on z-axis with 100% orientation.

A microscope image of the polished fiber tips can give the information necessary to determine the fiber orientation. This single sectioned, two dimensional fiber alignment analysis has some disadvantages when a wide range analysis of orientation distribution is present [126]. The cross-section of the fiber depicted in Figure 2-2 can be used to calculate the angle Ø of misalignment by Eq. 2-2.

$$Ø = \cos^{-1}(B/A) \tag{2.2}$$

Even though high material properties can be obtained by aligning short fibers in composite materials, it is hard to produce composite materials with well aligned and dispersed short fibers throughout the composite. Some of the methods which are used to align short fibers include: hydrodynamics [120], extrusion [127], electrostatics[128], and magnetics [11].

2.1.4.1 Hydrodynamics

The hydrodynamic alignment methods use a very viscous liquid fiber suspension to create composite parts with aligned short fibers by sending the suspension along a converging nozzle. The fibers in the suspension follow the streamlines in the fluid flow. Injection molding and extrusion use the hydrodynamic flow technique and this method was reported being capable of aligning over 90% of the short fibers in the suspension with the range of +/-15° accuracy [129].

Papthanasiou stated that existence of the short fibers in the fluid results with alteration of the velocity field[120]. As the fiber travels with fluid, velocity on the fiber surface generates a mismatch and result with the rotation of the fiber by disturbing the fluid around the fiber. Thin fiber generates smaller mismatch and results with slower rotation of the fiber out of the alignment. A short fiber with high aspect ratio in a flowing

suspension aligns quickly, leaves the alignment slowly and realign quickly when rotates out of the aligned direction. As a result, most of the fibers with high aspect ratio will stay aligned along the streamlines most of the time and easier to align [120, 130].

To achieve alignment of a plastic rod, the rod was flown in a direction several times in an epoxy slurry [131]. The motion of the rod through the slurry was adequate to achieve the fiber alignment. Compared to the randomly orientated fiber reinforced composites, the aligned ones had 100% more tensile strength and 90% more stiffness, agreeing with the prediction of the computer model[120]. While the fracture of matrix and debinding of the short fibers are more common with low value of fiber alignment, the breakage and pull-out of the fibers are mainly observed in highly aligned short fiber reinforced composites [130, 132].

2.1.4.2 Extrusion

In an investigation of short fiber reinforced composites produced by freeform extrusion with syringe extrusion and hot plate post curing system was done by Calvert et al. [133]. They found that increase of the fiber length resulted with increase of the Young's modulus. Their results restated that longer short fibers considerably enhance the mechanical properties [115, 117] including increase of the Young's modulus, reduction of the yield strain without any visible change on the yield stress.

In an another study, material properties of extruded polypropylene composite with the reinforcement of short fibers were predicted with the models of Cox [134] and Fukuda et al. [135] by examining the length, distribution and material properties of the short fibers [136]. The study revealed that the improvement of the short fiber alignment in the direction of the extrusion was the result of higher extrusion ratio. Uniform

orientation was achieved in the demonstrated section of the extruded polymer by ram extrusion, which is commonly used for production of polymer tubing, profile, and rod in industry.

The extrusion method was also demonstrated to align short fibers during a two staged method to produce carbon fiber reinforced prepregs [116]. In the first stage, liquid suspension of short carbon fiber and thermoplastic polymer were aligned by extrusion through a nozzle on a sloped rail. Then, the extruded mixture was processed to rotatory mandrel for the second stage of the alignment process. The method achieved ±4° of alignment accuracy with a reported material properties which is 80-94% of the continuous fiber reinforced counter parts.

Injection molding and extrusion of the short fiber reinforced polymer composites can achieve 85-95% degree of alignment; however these methods have certain drawbacks [116, 137, 138]. These methods require the suspension to be mixed before the process and mixing often causes fiber damage which leads to reduction of the fiber length and strength of the produced composite parts. This damage increases with higher fiber content and extrusion speed. Additionally, fibers should be dispersed in the suspension to avoid any blockages during the process.

2.1.4.3 Electrophoresis

Electric field induced alignment techniques of short fibers require conductive fibers. An electric field generated by the electrodes orients the fibers along the field lines [17, 139-141]. An electrical field was used by Chirdon et al. to align short fiber reinforced in a photocurable resin [139]. Glass fiber with diameter of 15μm and 120 μm lengths were mixed with the resin and the suspension were placed in a container with

embedded aluminum electrodes. The photocurable resin was solidified by a 1 mW He–N laser with 633 nm wavelength while the electrical field is still applied on the short fibers.

2.1.4.4 Magnetics

Currently, magnets which are strong enough to align reinforcements are easily accessible and allow remote contactless alignment and spatial control of reinforcement. Additionally, magnetic fields are not influenced by static charges on the surface or any surface chemistry compared to the electrophoresis method [142]. The size of the fibers has significant effect on the necessary magnetic torque of the fiber alignment. For nano scale particles, the process is dominated by the thermal forces, while the process for larger particles is dominated by gravitational forces. As a result, optimum alignment of the particles via magnetic field occurs when the size of the particles is a few micrometers [143, 144]. During studies of Takeyama et al. [144] the strength of the magnetic field required for alignment of single walled carbon nanotubes was 40 T, while it was by Erb et al. [143] as 10 T for 10μm particles.

Yamashita et al. [145] aligned short graphite fibers in a resin suspension using the magnetic field. They defined the critical concentration of the suspension and investigated the influence of the fiber content on the magnetic alignment and orientation of the short fibers. They demonstrated that fiber aligned along the magnetic field when they are coated with ferromagnetic material, such as nickel. If fiber content is increased too high, fiber-to-fiber interactions limit the alignment of the fibers.

2.1.5 Flow Induced Alignment

Existing methods for the orientation of short fibers in a bulk suspension flow use models which include the orientation of the fibers and the added stress caused by the

fibers. The added stress is related with the orientation of the fibers and the couple orientation to the momentum equations. For an accurate estimation of the microstructure of short fiber in the composite, material related parameters of the equation should be defined right. Similar methods are also used to analyze effect of shear flow in other objects, such as alignment, tumbling, deformation [146].

The use of rheology is common for determining the material related parameters of the equation. In this approach, flow field and testing conditions, including temperature of the suspension and shear rate applied, are well controlled to simplify the equation of the model. By using an accurate added stress, the material related parameters can be calculated without any measurement of the actual fiber orientation.

2.1.5.1 Orientation Theory

Most of the calculations related with the particle orientation branched from Jeffery's study which is governed by continuum mechanics [147]. He derived related fundamental governing equations of the rotational motion of an elliptical particle in a flow. This calculation was expanded by additional term, which is referred to as isotropic rotary diffusion, to include the influence of the fiber-to-fiber interaction onto the fiber orientation [148]. Additional modifications of the equations have been studied, such as anisotropic rotary diffusion [149], slowed kinetics[150], interactions between fibers [151], and flexible fiber [152, 153]. Some of these different models contain parameters for length, flexibility, and concentration of the fibers, while others account for them by phenomenological parameters. Strautins et al. [152] included additional terms in their model for fiber length and rigidity. Their fiber representation is demonstrated in Fig. 2-3 and the fiber orientation is simplified with a vector from tip to tip.

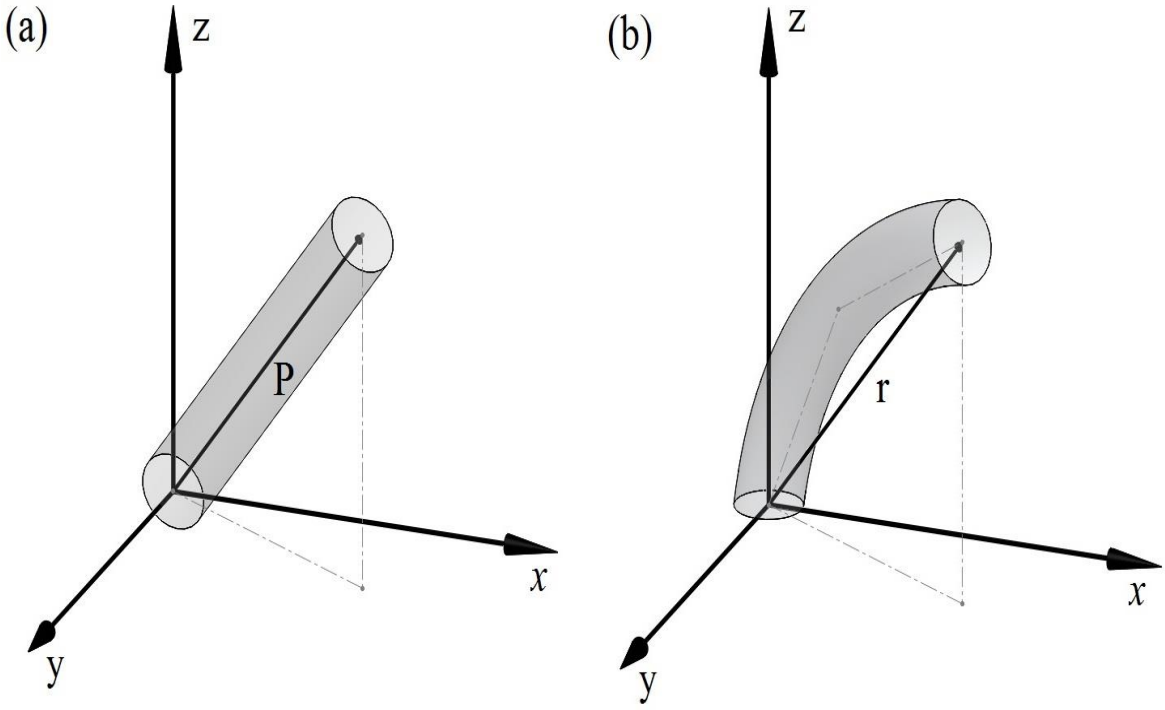

Figure 2-3 Common depictions of fibers: (a) rigid fiber, (b) semi-flexible fiber

Numerical analysis is also used as a different method to analyze a single fiber and can include different fiber dynamics, such as flexibility, interaction between fibers, complex networks, when they are formulated [154-156]. Wang et al. simplified the bending properties of the flexible fibers by modeling them as connected rigid sections [157]. The simplification allowed the model to estimate some phenomena, such as aggregation of the fibers which is harder to calculate with continuum mechanics [158].

2.1.5.2 Stress Theory

The addition of fibers in the matrix generates additional stress around the fiber surface which is contributed by both fibers and the matrix. The fiber related contributions can be listed as; stress on a fiber caused by tension force [159], interaction with another fiber [151], movement and deformation of the flexible fiber [153]. As the aspect ratio of

the fiber increases, influence of the flexibility and interactions between fibers also increases. Rajabian et al. [153] and Keshtkar et al. [160] used thermodynamic models to include flexibility of the fiber and the interactions between fibers. They used empirical parameters for their models because of absence or the complexity of the stress calculation; therefore most of the recent researches are untested except the authors' own study.

2.1.5.3 Rheology

Rheological analysis of shear flow was performed in many studies for observing the relation between fiber orientation and stress, which was used to measure the stress values as a reflection or substitute of the orientation of the fibers [161, 162]. As the fibers aligned in the flow of the suspension, shear stress also grows within the suspension. The biggest variances in a fiber suspension under steady shear occur at low shear rates, where the suspension displays shear thinning phenomenon.

2.1.5.4 Rheology and Complex Flow Simulations

The main aim of the research is to employ rheology to determine material parameters of the processing flow by using a rheometer under known and simplified circumstances [162, 163]. Subsequently, these independently acquired material parameters can be used to assess fiber orientation model during extrusion or injection molding. Similar studies were also performed for analysis of flexible fiber orientation [164, 165] on a center-gated disk with parameters acquired from previous rheological studies [166].

Meyer et al. [165] used the material parameters obtained from center-gated disk study to an end-gated plate. They improved the orientation predictions of the fibers in the

end-gated plate by fitting the parameters based on the orientation at various locations in the plate. They demonstrated that their orientation model for the analysis of the semi-flexible fibers delivered better predictions compared to the rigid fiber orientation model.

2.1.5.5 Dynamic oscillatory shear

Dynamic oscillatory shear analyses are executed by applying a sinusoidal strain on the material to determine the mechanical response of the material relative to the time. Regimes of the dynamic oscillatory shear analyses are categorized as small amplitude oscillatory shear (SAOS) for the shear strain range where material has linear response and large amplitude oscillatory shear (LAOS) for the shear strain range where material has nonlinear response. As the shear strain is increased at a set frequency, the regime of the material response changes from linear to nonlinear (see Fig. 2-4).

Even though the linear material respond is beneficial during analysis of complex fluids for rheological material property examination, linear respond can only be observed in a small band of shear strain [167]. Therefore, most of the production methods process in the large and rapid strain ranges where behavior is nonlinear and thus, linear viscoelasticity does not apply. Therefore, it can be expected that nonlinear material response characterization offers more accurate estimates for a real process and the investigation of nonlinear material responses for better understanding is essential.

The steady shear nonlinear rheology analysis is commonly used related with the processing speed capabilities of a material and it is very essential for operations such as extrusion and injection molding. But, most of the processing methods especially for injection molding have very high shear strain and very short speed for steady state regime to be established [168]. Additionally, experiments of steady simple shear rate

viscometry have constraints related with the amount of information that can be obtained about microstructure, elastic relaxation, and material options. This method cannot test crosslinked materials or structurally-sensitive materials, while LAOS can be used for various complex fluids as a result of the wide range of strain amplitude and frequency options that can be applied [169].

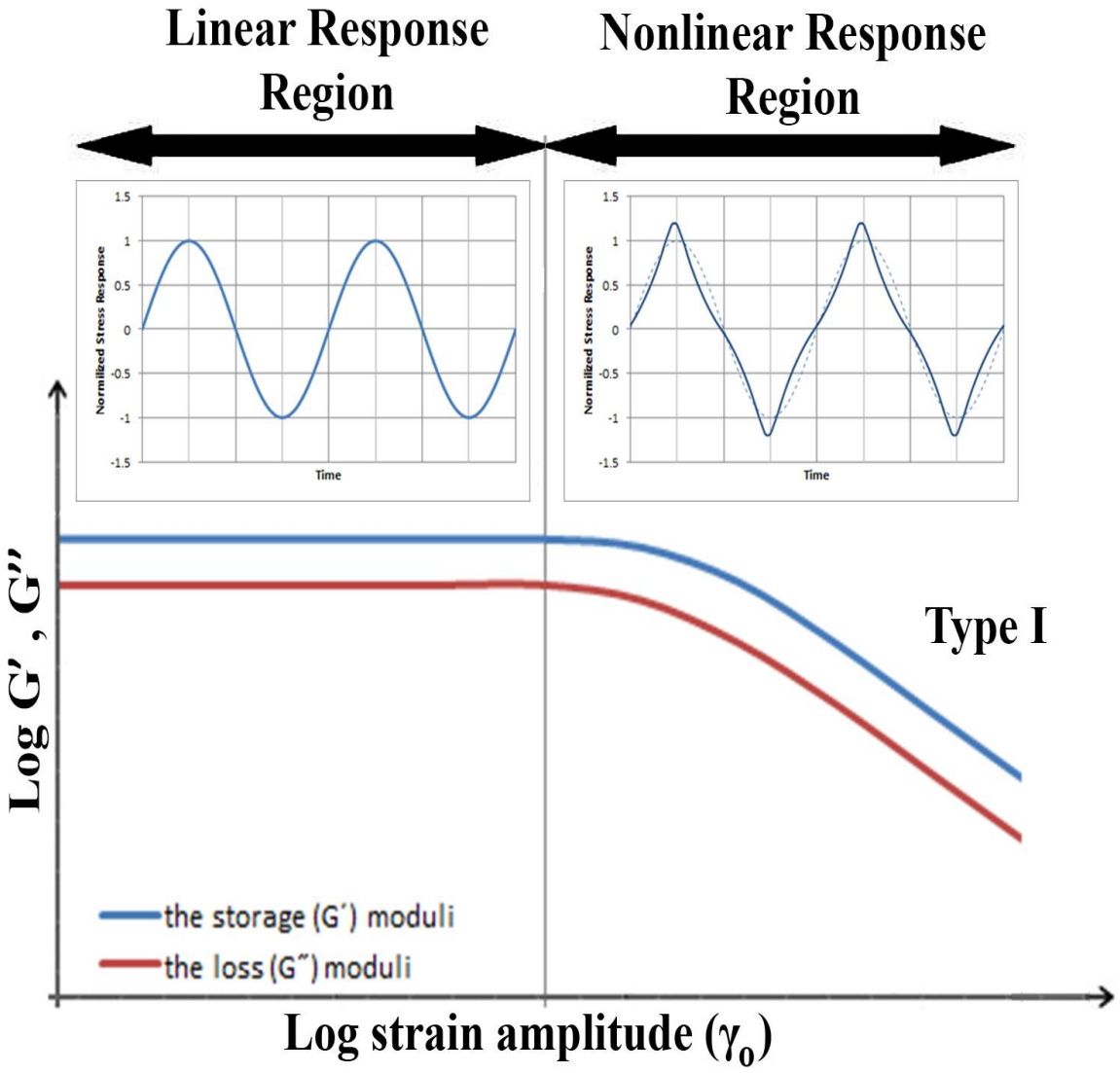

Figure 2-4 Schematic illustration of fixed frequency dynamic oscillatory shear test with linear and nonlinear response regions.

2.1.5.5.1 Fundamental LAOS Behavior

. During an oscillatory shear flow application, the shear strain and shear rate inputs can be described as follows:

$$\gamma(t) = \gamma_0 \sin \omega t \tag{2.3}$$

$$\dot{\gamma}(t) = \omega\gamma_0 \cos \omega t \tag{2.4}$$

Stress during large amplitude oscillatory shear can be defined as an expanded form of a stress during small amplitude oscillatory shear by shift of amplitude and phase and adding higher harmonic terms

$$\sigma(t) = \sum_{n=1,odd} \sigma_n \sin(n\omega t + \delta_n) \tag{2.5}$$

Equation can be rewritten to separate shear strain variable from frequency dependent variable [168]:

$$\sigma(t) = \gamma_0 \sum_{n,odd} [G'_n(\omega, \gamma_0) \sin(n\omega t) + G''_n(\omega, \gamma_0) \cos(n\omega t)] \tag{2.6}$$

or,

$$\sigma(t) = \sum_{n,odd} \sum_{m,odd}^{n} \gamma_0^n [G'_{nm}(\omega) \sin(m\omega t) + G''_{nm}(\omega) \cos(m\omega t)] \tag{2.7}$$

The complex calculations of the conditions for large amplitude oscillatory behavior cause different interpretations of the behavior.

2.1.5.5.2 Different LAOS behaviors

As mentioned before in Section 2.1.5.5, LAOS analyses are done by applying an oscillatory shear strain regime, such as sinusoidal wave, generally with a stable frequency at amplitude where viscous response is nonlinear (see Fig. 2-5). During a nonlinear

viscous regime, which is characterized with $G'(\omega)$ the elastic storage modulus and $G''(\omega)$ the viscous loss modulus, $G'(\omega)$ and $G''(\omega)$ values are generally hard to interpret because of non-sinusoidal response.

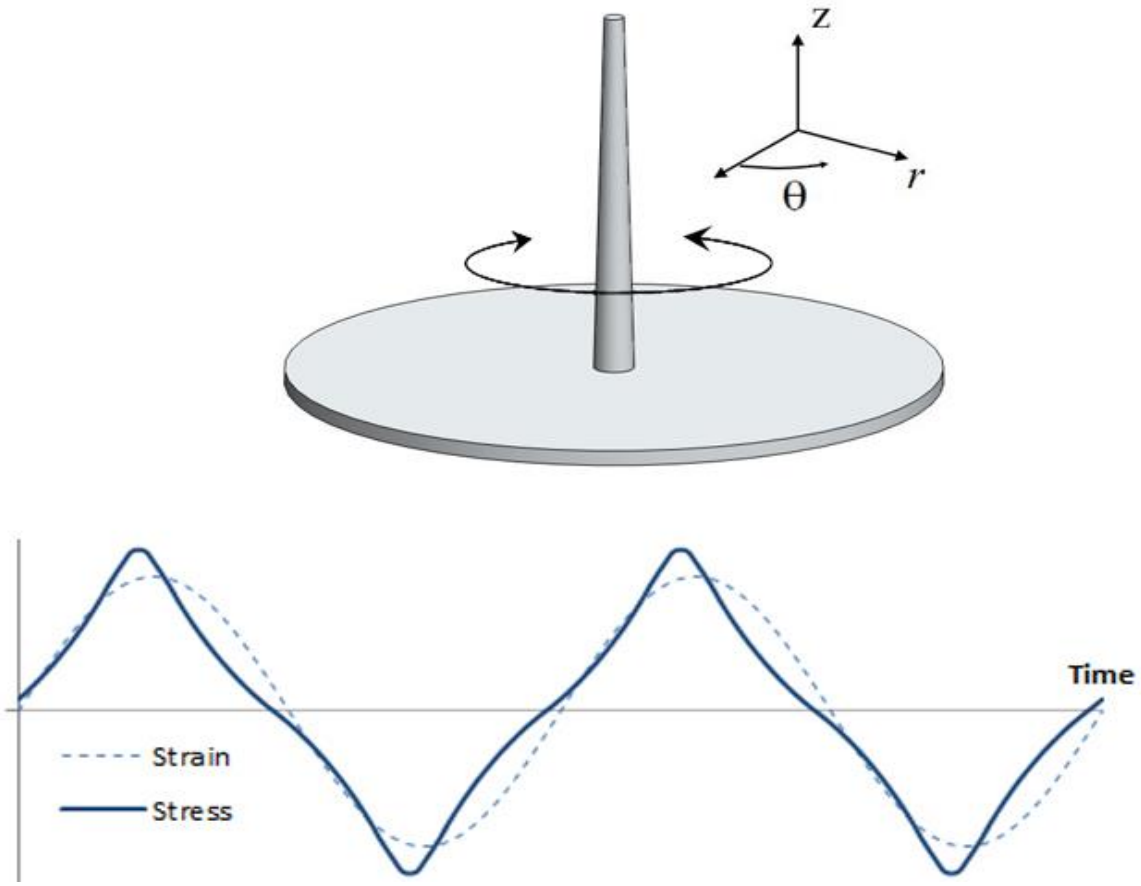

Figure 2-5 Schematic illustration of the LAOS test at a fixed frequency with the resulting distorted sinusoidal stress waveforms.

As a result of being easily obtained from commercial rheology devices, G′(γ0) and G″(γ0) values are commonly involved in the investigation of the LAOS tests. In the LAOS studies distortion of stress response away from the shear strain form are mainly contributed by first amplitude harmonic [168]. Leading-order of the fluid viscous behavior classified 4 types of LAOS behavior [170]:

- **Type I - strain thinning**

Strain thinning is most commonly encountered type of the fluid viscous behavior in LAOS tests of the polymer solutions, resins, suspensions and melts. The cause of the behavior is related with shear thinning behavior which is observed during steady shear flow. Shear thinning as a rheological property is also mostly dominant in polymer based liquid suspensions and it originates from modification of microstructure and orientation of the polymer chain structure by the shear rate. The alignment of the polymer chains parallel to the flow direction decreases local drag forces in the material. Increase of the shear strain increases the accuracy of the flow induced alignment of the structure and also decreases the viscosity of the liquid [171]. Examples of flow induced alignment have been described in recent studies [172-175]. In Ch. 3 and 4, studies based on fiber alignment via strain thinning behavior of polymer suspension under LAOS have been demonstrated.

- **Type II - strain hardening**

Type II strain hardening is the opposite of type I stain thinning. During strain hardening, complex microstructure and network elements generated by the shearing produce stronger interaction between different segments in the fluid which resist to progressing shearing strain. Polyvinyl alcohol/borax solution responds to LAOS with strain hardening as result of temporary crosslink formed between borate anions and hydroxyl groups [176]. The generation of new strain stiffening complex network elements needs to be more than the rate of decline for the existing networks in order for strain hardening to occur. As the large strain increases, the torque rapidly rises and causes the rheological viscous properties to become hard to measure.

- **Type III - weak strain overshoots**

Type III weak strain overshoots behavior is distinguished by a noticeable local maximum in the viscous loss modulus. Materials with type III behavior are commonly referred as "soft glassy materials". The experimental reason for the overshoot in the viscous loss modulus depends on the type of the material. Some of the suggested causes for the behavior are growth of temporary structures effective volume [177], change of flock dimensions in a flocculated polymer suspension [178], and the movement of unstable clusters [179].

- **Type IV - strong strain overshoot**

Type IV material response is observed with a small group of material systems and distinctive by exhibiting an overshoot in the elastic storage modulus and the viscous loss modulus [177]. This behavior might be associated to the weaker strength of the interaction in the molecular level compared to type II and stronger compared to type III. This behavior response occurs less frequently than type III.

2.2 Acoustic Particle Patterning

Noncontact handling technologies to manipulate and control spatial distribution of the small particulates in a fluid suspension based on physical characteristics of particulate have become increasingly important. The magnetic field [11, 180], laser radiation pressure[181], and the acoustic field [182-186] have been used for noncontact handling. The manipulation of the particles by the acoustic field has been gaining more interest for the operations of particle trapping, particle separation, particle alignment, particle detection, particle enrichment, fluid mixing and purification [182]. Sorting, screening, and manipulation operations for micro and nano particulates have also made it

appropriate and advantageous for the acoustic field to be used in biotechnology, additive manufacturing, and microfabrication [183]. Low stresses and forces make non-contact handling by the use of the acoustic field especially desirable for the handling of sensitive and fragile cells compared to contact based handling which includes solid tools capable of rupturing the cell.

Standing acoustic waves, which are formed by designed resonating compartment and corresponding tuned frequency of the acoustic wave, are the main objective of the acoustic patterning application. With the assumption of isolated and well dispersed incompressible sphere particles in the standing acoustic field in inviscid fluid, the force applied on the sphere particle has been described by King in 1934 [187]. The theory has been further extended with compressible particles by Yosioka and Kawasima, the viscosity of the host medium by Doinikov, and the viscous boundary layer correction factor by Settnes and Bruus [188]

The acoustic field has three main effects on the fluid and particles which consist of acoustic radiation force, acoustic streaming and acoustic cavitation. Acoustic radiation force occurs as a result of scattering caused by the affected obstacles in the medium and drives the obstacle toward the pressure nodes or anti-nodes of the acoustic field. Acoustic radiation forces are the main forces used for particle manipulation and they are classified as the primary and secondary radiation forces. While acoustic radiation force is related with scattering effect of particles, acoustic streaming relates to flow of the fluid propagated by the presence of a gradient acoustic momentum flux in the medium [184] and mainly used for acoustic mixing applications [182]. Acoustic streaming as a fluid flow induces a drag force which can overcome the acoustic radiation force and therefore

it is undesired and it needs to be suppressed when acoustic trapping is desired. Lastly, acoustic cavitation is the phenomenon which gas bubbles in the medium are oscillated with the existence of acoustic pressure when intensity is not strong enough to collapse the gas bubble and it takes place with 1MHz and lower frequencies. Ultrasonic cleaning and cellular sonication are the main applications of the process and ultrasonic cavitation can create extra stress or even permanent physical damage to the cells. The frequencies used in this study were between 2-10 MHz and therefore acoustic cavitation was not further explained in the literature review.

2.2.1 Acoustic Radiation Forces

As a result of 2-10MHz acoustic frequency range, acoustic radiation forces and acoustic streaming forces are the main categories to review to achieve better acoustic trapping and alignment performance. Acoustic radiation forces, which propagated as a result of acoustic wave by particulates or obstacles inside of the suspension medium, force the particulates to the pressure node where pressure amplitude is minimum or to the pressure anti-nodes where pressure amplitude is maximum. This process is based on the particulate's physical properties, such as density and compressibility. These radiation forces are categorized as the primary and secondary radiation forces. The primary radiation forces are the main manipulation forces for suspended particles, while the secondary radiation forces are at smaller orders of magnitudes between very short distanced particles.

2.2.1.1 Primary Radiation Forces

The primary radiation force can be decomposed into the primary axial radiation force which is in the direction of the acoustic propagation and the primary lateral

radiation force, packing the objects closer to each other and keeping them in their locations (See Fig. 2.6). The primary axial radiation force transports objects to either the nodes or the anti-nodes of the acoustic wave and is stronger than the primary lateral radiation force.

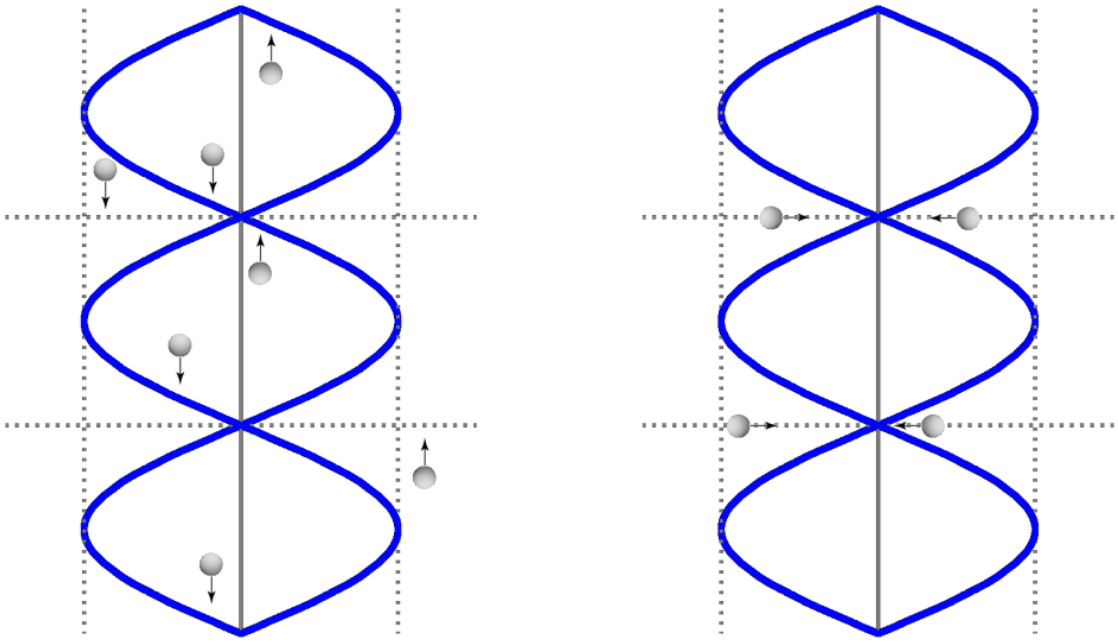

a) Primary axial radiation forces b) Primary lateral radiation forces

Figure 2-6 Primary radiation forces on particles (a) Primary axial radiation forces are perpendicular to the nodal plane and they attract or repel the particles relative to the nodal plane of the acoustic wave; (b) Primary lateral radiation forces are parallel to nodal plane that trap the objects on the nodal plane.

Primary radiation forces are applied on the objects in the medium by the incident acoustic wave. When particle radius is smaller than the wavelength of the acoustic wave, the primary radiation force on an individual particle is the gradient of the acoustic energy density with the assumption of suspended, spherical, and compressible particles in an inviscid fluid [183]. In an acoustic standing wave field, radiation forces are

much greater and big enough to carry the particles to distinctive regions of the acoustic field. The fluid pressure and velocity can be expressed as;

$$p(x,y,z,t) = p_a(y,z)\sin\left(\frac{2\pi x}{\lambda}\right)\sin(2\pi f t) \tag{2.8}$$

$$v(x,y,z,t) = v_a(y,z)\cos\left(\frac{2\pi x}{\lambda}\right)\cos(2\pi f t)\,\hat{\boldsymbol{k}} \tag{2.9}$$

where, p_a is fluid pressure, $v_a = p_a/\rho_f c$ is velocity amplitude, c is the fluid sound speed, ρ is the density of the liquid, λ is the wavelength, and f is the frequency of the acoustic standing wave.

The primary acoustic force on a single particle with a radius much smaller than the wavelength suspended in an inviscid fluid [186] can be derived as;

$$F_{PRF} = -\frac{2\pi V_p E_{ac}}{\lambda}\phi\sin\left(\frac{4\pi x}{\lambda}\right) \tag{2.10}$$

$$\phi = \frac{5\rho_p - 2\rho_f}{2\rho_p + \rho_f} - \frac{\beta_p}{\beta_f} \tag{2.11}$$

where, V_p is the volume of the particle, $E_{ac} = {p_a}^2\beta_f/4$ is the acoustic energy density, β_p is compressibility of the particle, β_f is compressibility of the liquid, and ρ_p is the density of the particle. The direction of the acoustic primary radiation force is determined by ϕ factor in Eq. 2.10 and depends on the density and compressibility of the particles and the liquid.

The Primary lateral radiation force acts on the particles, forcing them on the central axis and traps them at the pressure node when the continuous fluidic flow is aligned perpendicular to the acoustic standing wave. The Primary lateral radiation force can be derived as [189].

$$F_{PLRF} = V_p\nabla E_{ac}\left[\frac{3(\rho_p - \rho_f)}{2\rho_p + \rho_f}\cos^2\left(\frac{2\pi x}{\lambda}\right) - \frac{\beta_f - \beta_p}{\beta_f}\sin^2\left(\frac{2\pi x}{\lambda}\right)\right] \tag{2.12}$$

2.2.1.2 Secondary Radiation Forces

The secondary radiation forces are also called the interparticle forces or Bjerknes forces. They are caused by interactions between scattered acoustic field and nearby objects. When it is assumed that the object size and the distance between the objects are much smaller than the wavelength of the of the standing acoustic field, the equation of the secondary radiation forces for two identical spheres can be derived as [190];

$$F_{SRF} = 4\pi r^6 \left[\frac{\left(\rho_p - \rho_f\right)^2 (3\cos^2\theta - 1)}{6\rho_f d^4} v^2(x) - \frac{\omega^2 \rho_f \left(\beta_p - \beta_f\right)^2}{9d^2} p^2(x) \right] \quad (2.13)$$

where, r is the radius of the object, d is the distance between the objects, θ is the angle between the axis of the acoustic propagation and the centerline of the object. When the sign of the force is negative the particles attract each other; if positive, they repel each other (See Fig. 2-7).

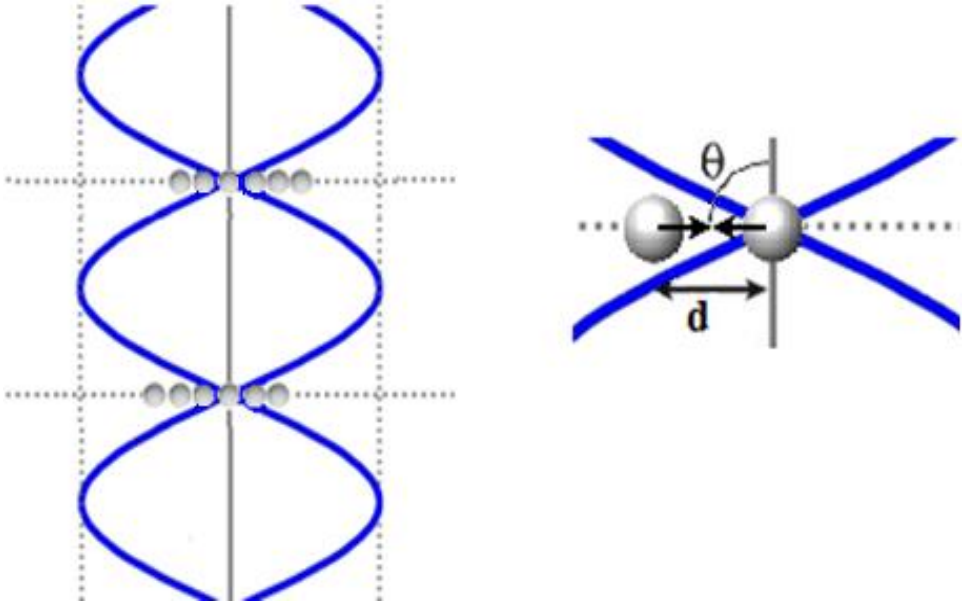

Figure 2-7 Secondary radiation forces on particles when primary radiation forces decrease the particle distances to small values

2.2.2 Acoustic streaming

Acoustic streaming is a fluidic motion induced by the acoustic standing wave in addition to the acoustic radiation forces and can be caused by viscous losses at a fluidic boundary layer or acoustic absorption in the fluid. It can be observed as large scale fluid flow, such as container scale streaming rolls called Eckart streaming, or small scale fluid flow, such as wavelength scale vortexes called Rayleigh streaming and viscous boundary layer flows called Schlichting streaming [189]. When a standing wave is parallel to the surface, the viscous dissipation creates a steady layer vorticity, which is called Schlichting streaming, and this streaming generates counter rotating vortices called Rayleigh streaming. On the other hand, the origin of large scale fluid streaming, which is called Eckart streaming, is attenuation of acoustic energy in the bulk fluid [184, 191].

Even though acoustic streaming is useful for fluid mixing and cell lysis, it is generally undesired for particle trapping or manipulation because of the ability to drag the particles or to disturb the result and therefore it is a limiting factor. Even though it is a natural result of acoustic field, it is possible to suppress the effect of acoustic streaming to have sufficient particle manipulation.

For acoustic particle trapping and manipulation, acoustic streaming is commonly considered as an undesired effect, because of the drag forces generated by the streaming flow. Drag forces on the spherical particle according to Stokes' law;

$$F_d = 6\pi\mu r_p u \tag{2.14}$$

where r_p is the radius of the particle, μ is the viscosity of the medium and u the velocity. As the drag force is proportional to the radius of the particle, compared to the primary radiation force which is proportional to the volume of the particle. It can be understood

that primary radiation force will dominate the larger particles while Stokes' drag force disturb and dominate the smaller particles.

2.2.2.1 Inner and Outer Boundary Layer Acoustic Streaming

The inner and outer boundary layer acoustic streaming are driven by viscous attenuation of an acoustic wave in the solid-fluid boundary layer due to a velocity gradient generated by the non-slip condition at the interface. High viscous dissipation of acoustic energy caused by the large viscous forces inside the boundary layer generates acoustic streaming. This boundary layer can be expressed as a function of the kinematic viscosity, v, and the angular frequency of the acoustic field, f [188];

$$\delta_v = \sqrt{2v/f} \tag{2.15}$$

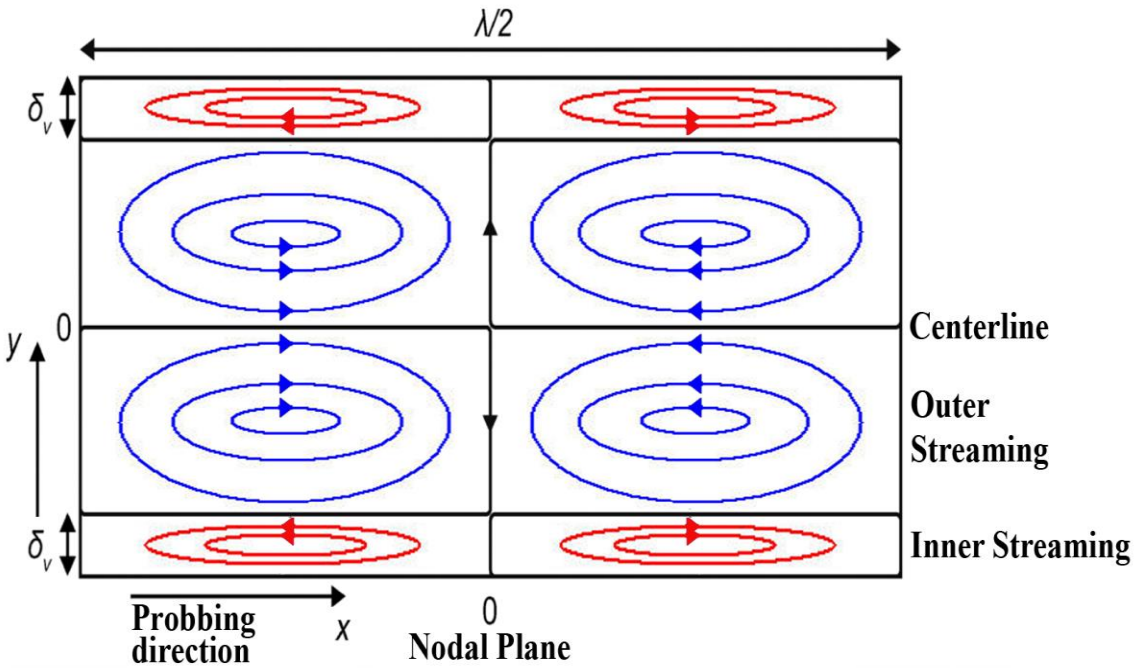

Figure 2-8 A system of inner (Schlichting) and the outer (Rayleigh) boundary layer acoustic streaming vortices in a channel with a standing wave.

The acoustic streaming inside this boundary layer is known as inner boundary streaming or Schlichting streaming, named after Hermann Schlichting. This inner boundary streaming vortices generates counter rotating vortices which is called outer boundary streaming or Rayleigh streaming. A schematic of the inner and the outer boundary layer acoustic streaming is shown in Fig. 2-8. The streaming is divergent within the pressure node x=0 and works against to the lateral radiation force which trap the particles in the pressure nodal plane [184].

According to Wiklund [184], the boundary layer driven inner and outer boundary layer acoustic streaming is particularly pronounced under the condition that

$$\lambda \gg h \gg \delta_v \tag{2.16}$$

where, λ is wavelength of acoustic wave, h is length of the chamber, and δ_v is the viscous boundary layer.

There have been extensive studies in Rayleigh streaming in the field of acoustic particle trapping and manipulation, mainly because it counteracts against the primary radiation force which manipulate and trap the particles into pressure nodes and creates a lower limit for particle size. This lower limit is proportional to $1/\sqrt{f}$ and decreases as the frequency increases. For example manipulation of approximately 1 μm even smaller would be possible with 10 MHz frequency [184].

2.2.2.2 Eckart streaming

Eckart streaming is the flow induced by the attenuation of acoustic energy into the bulk of a fluid [189]. As the acoustic wave travels through a medium, the amplitude of the acoustic wave decreases exponentially due to the absorption by the medium with the distance from sound source due to the viscous attenuation. This absorption is proportional

with the square of the frequency of the wave and the power density of the transducer. This acoustic energy loss generates a momentum flux and a jet flow in the direction of the acoustic wave propagation. In a closed chamber, this process would create a fluid circulation in the chamber (see Fig. 2-9). Both traveling waves and standing waves are capable of producing Eckart streaming, but bidirectionality of the standing wave decreases the Eckart streaming by partially counteracting it [188]. Additionally, Wiklund [184] described the Eckart streaming as a product of transducer and emitted beam profiles misalignment with the reference to Hertz [192].

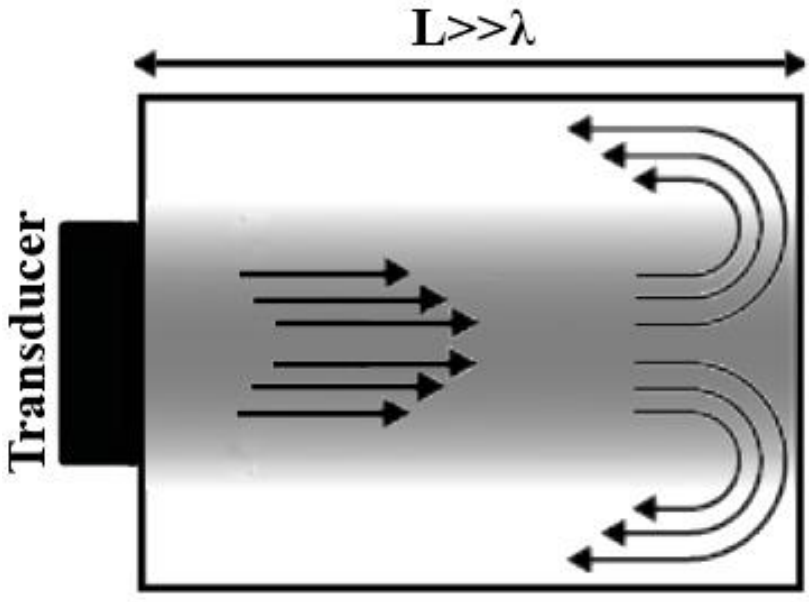

Figure 2-9 Eckart streaming with a backflow which is induced by forward streaming in a resonator much larger than the wavelength ($L \gg \lambda$).

2.2.3 Impact of Material Properties

Acoustic particle and cell manipulation is mainly dependent on frequency and pressure amplitude of the acoustic wave, on the volume and shape of the particle, and on the material properties of the particle or object. Both the compressibility and the density

are the material properties of the particle or cell which determine the acoustic force, trapping speed and location. The acoustic contrast factor ϕ, determines the material dependence of the acoustic force, see Eqn. 2.17.

$$\phi = f_1 + \frac{3}{2} f_2 = \frac{5\rho_p - 2\rho_f}{2\rho_p + \rho_f} - \frac{\beta_p}{\beta_f}$$
$$f_1 = 1 - \frac{\beta_p}{\beta_f} \quad f_2 = \frac{2(\rho_p - \rho_f)}{2\rho_p + \rho_f} \tag{2.17}$$

The acoustic contrast factor determines the primary acoustic radiation force and is a function of compared compressibility and densities of the particle and the medium. The impact of this parameter can be understood by comparing the outcome of different particle acoustic properties for cases.

2.2.4 Sound Actuation

Sound is a propagation of energy as a mechanical wave of pressure and displacement caused by the vibration of particles in the transmission medium, such as air or water. The particles oscillate back and forth in a small distance which causes a longitudinal wave to propagate in the same direction as the vibration of the particles. Vibration on a portion of an electroacoustic transducer's surface produces sound and transmits the vibration by affecting the neighboring molecules in the transmission medium. The vibrating molecules push against their next neighbors, causing them to also vibrate. This process continues and propagates a wave in which the pressures oscillate between condensation and rarefaction as it advances further far from the transducer.

2.2.4.1 Speed of Sound

The speed of sound c, is the velocity that the sound waves propagate through a transmission medium. The speed of sound is a function of the composition of the

particular medium, but slightly changes with temperature, stiffness, bulk modulus or pressure.

$$c = \sqrt{\left(\frac{\partial p}{\partial \rho}\right)_s} = \sqrt{\frac{K_s}{\rho}} \tag{2.18}$$

where K_s is coefficient of stiffness in solid and bulk modulus in air or liquid, ρ is density, and p is pressure.

2.2.4.2 Wavelengths of Sound

The wavelength of sound which is the distance between condensation peaks and is a function of both the frequency and the speed of the sound wave;

$$\lambda = \frac{c}{f} \tag{2.19}$$

where λ is wavelength and f is frequency.

2.2.5 Attenuation and Damping

Attenuation and damping, which are interchangeable terms, are the reduction in the magnitude of oscillations as a result of dissipation of energy in the medium. For acoustic, attenuation refers to a dimensional amplitude change and damping refers to a sequential amplitude change. Another way of describing the attenuation and damping in acoustic is using energy dissipation by the quality factor or Q-factor.

2.2.5.1 Attenuation Coefficient

With the assumption of complex time harmonic oscillations, the first order acoustic wave equations lead to a complex wave number;

$$k_c = k + i\alpha_s = \frac{\omega}{c_0}\sqrt{\frac{1 + i\omega\tau_s}{1 + \omega^2\tau_s^2}} \tag{2.20}$$

For most viscous liquids except highly viscous ones the viscous relaxation time τ_s is of the order of 10^{-12} s [18]; Therefore, $\omega\tau_s \ll 1$ holds and the spatial attenuation coefficient α_s can be simplified as;

$$\alpha_s \approx \frac{1}{2}\frac{\omega}{c_0}\omega\tau_s = \frac{\omega^2}{2\rho_0 c_0^3}\left(\frac{4}{3}\mu + \mu_B\right) \tag{2.21}$$

The solution to the Helmholtz equation for a plane wave traveling in positive x-direction is [18];

$$p = \hat{p}e^{i(k_c x - \omega t)} = \hat{p}e^{-\alpha_s x}e^{i(kx-\omega t)} \tag{2.22}$$

Eqn. 2.22 represents an exponential decay in space of the wave. In literature the attenuation coefficient is typically given in a logarithmic scale like decibel (dB) and normalized by the frequency squared calculated by [18];

$$\begin{aligned} \alpha_{sdB} &= \frac{10}{f^2\Delta x}\log_{10}\left(\frac{I}{I_d}\right) \\ \alpha_s &= \frac{\ln(10)}{20}\alpha_{sdB} \end{aligned} \tag{2.23}$$

where Δx is the attenuation distance and I and I_d are the acoustic intensities at reference and attenuated state. These equations provide a relation between energy dissipation the Navier–Stokes equations and a simplified model with attenuation coefficient α_s. This is very useful for comparison of damping in boundary layer driven streaming with attenuation driven streaming.

2.2.5.2 Quality Factor and Loss Factor

The attenuation coefficient α_s is independent of any geometrical dimensions. On the other hand the Q-factor is mainly used for systems with multiple parts and geometrical restraints. Both terms can be linked by using loss factor or dissipation factor η [18];

$$\eta = \frac{1}{Q} = \sum_i \frac{1}{Q_i}$$

$$Q = 2\pi \frac{Energy\ stored}{Energy\ dissipation\ per\ cycle} = \frac{2\pi}{1 - e^{-4\pi\frac{\alpha_s}{k}}} \approx \frac{k}{2\alpha_s} \tag{2.24}$$

Chapter 3: Printing Ceramic Matrix Composite with Controlled Orientation

3.1 Introduction

Traditional ceramic forming techniques, such as slip casting, shell casting, dry pressing; are not capable of producing complex parts with high accuracy without expensive molds or fixtures, or time consuming post-sinter machining [193]. Therefore, there is a demand and interest for alternative methods to produce complex ceramic pieces without the use of expensive tooling. Three dimensional printing (3DP) methods of ceramics and ceramic composites can directly produce complex parts from 3D CAD files without the use of any tooling. Fused deposition modeling (FDM) [78], selective laser sintering (SLS) [194], ceramic jet printing (CJP) [195], and stereolithography (SLA) [196] are some of the common 3DP methods which are used for additive manufacturing of ceramic and ceramic composite materials. During these processes, 3D complex objects are fabricated by rendering each layer according to CAD file and stacking them on each other.

The SLS method involves the use of high power laser beam to bond ceramic particles to each other locally [197, 198]. Localized temperature gradient during sintering process can generate high internal stresses which might cause lots of defects and micro cracks. The FDM, CJP, and SLA ceramic processing methods use a mixture of a ceramic

powder and a polymeric binder to fabricate green parts without high energy input. Fabricated green part must be sintered to remove polymeric binder and to fuse the particles. However, the extrusion of precursor filament is often disturbed by buckling failures and powder volume fraction is limited by extrusion pressure at the nozzle for FDM and CJP processes [78]. On the other hand, SLA of ceramics utilizes photosensitive resin as a binder to produce the green parts without any nozzle and high energy laser beam. Without any nozzle and high energy input, internal stresses, buckling failures, and extrusion pressure are avoided.

The use of pure ceramic materials as a structural material has been limited, due to its overall low toughness and thermal shock resistance [199, 200]. As a result, additive of reinforcement such as whiskers [201, 202], short fibers [203, 204], particles [193, 205], and nanotubes [206, 207] into ceramic matrix attracted a lot of research interest with the ability to enhance desired properties. These enhancements are influenced by the material, dimensions, and orientation of the reinforcement [203, 208]. Therefore, fiber alignment can be used to tailor the material properties of 3D printed composite pieces, such as mechanical [9] and electrical [209]. The use of shear induced alignment was demonstrated during SLA 3DP for reinforced polymer composites (RPC) at our previous study [174]. In this work, same approach was utilized for 3DP of ceramic composites. Micro scale alumina, silica, and nickel coated carbon fibers (NCCF) were used as reinforcement. Respond of reinforcement to patterned wall direction and enhancement of flexural strength of the composite material with fiber orientation were discussed.

3.2 Materials and Methods

3.2.1 Slurry Preparation

The ceramic photocurable resin used in this paper is a mixture of both ceramic powders and liquid photocurable resin. Powder part contains silica powder, Feldspar powder, Kaolin clay powder and Ball clay powder (all from Axner Co.), and liquid resin part is a mixture of Laromer 8765 (BASF Co.), Laromer HDDA (Hexane-1,6-diol diacrylate, BASF Co.), and lauryl acrylate (Esstech Inc.). Irgacure 754 (a mixture of Oxy-phenyl-acetic acid 2-[2-oxo-2-phenyl-acetoxy- ethoxy]\-ethyl ester and Oxy-phenyl-acetic acid 2-[2-hydroxy-ethoxy]-ethyl ester) and Irgacure 4265 (a mixture of Diphenyl (2,4,6-trimethylbenzoyl-phosphine oxide and 2-Hydroxy-2-methyl-1-phenyl- propan-1-one)) from BASF Co. was used as photoinitiators. 0.2 wt%. Tinopal OB (BASF Co.) is used as a UV absorber. 60 wt% of silica content was added within the resin as the ceramic filler and mixed with shear mixer for 24 hours to provide homogeneity. During the mixing process, the viscosity of the slurry was reduced as result of shear thinning behavior of the fluid. After the mixing, if the slurry was not used for 8-10 hours, ceramic fillers would settle to the bottom of the slurry as sediment and then slurry would require remixing.

While silica particles were used as the matrix, NCCF, alumina, and silica fibers were used as fiber reinforcement for the ceramic matrix composite. Carbon fiber is inclined to oxidation at temperature 500 °C and higher, as a result it requires protection from atmosphere to preserve its superior properties [210]. Nickel coating was used as the protectant in this study. NCCF with 7 µm diameter and 1 mm mean length were obtained from Tfpglobal. Alumina and silica fibers with 2.5-3 µm diameter and 2.7-3.2 mm mean

length have been obtained from Zircar Ceramics. NCCF were added in UV-curable slurry with the ratios of 0.25, 0.5, 0.75, and 1 wt% and ceramic fibers were added with the ratios of 2.5, 5, 7.5, and 10 wt% right before 24 hour shear mixing.

3.2.2 SLA Apparatus and Linear Oscillatory Mechanism

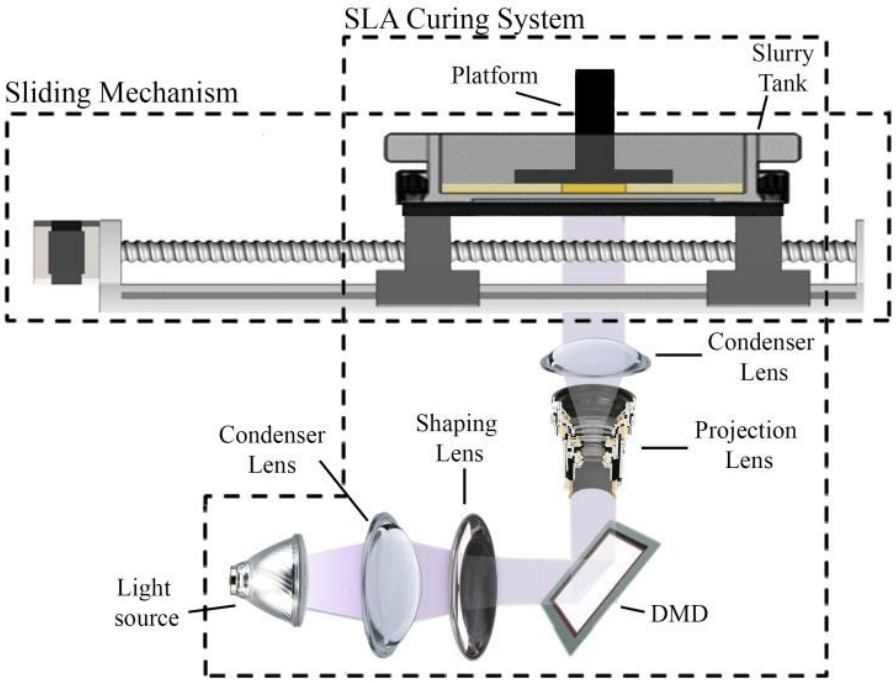

Figure 3-1 System setup of SLA Ceramic 3DP with sliding mechanism.

Production of ceramic samples and fiber alignment rely on an SLA based curing system and linear sliding mechanism. As the systems shown in the schematic (See Fig. 3-1), the SLA curing system consists of a platform, a slurry tank, and a projection unit, while linear sliding mechanism consists of a linear stage which is connected to the slurry tank. In the projection unit, light is emitted through the optical lenses onto the DMD chip to be patterned and reflected towards the projection lens and then refocused onto bottom of the slurry tank. Refocused image on the bottom of the slurry tank has the pixel size of 25 μm. Micro wall patterns are produced to generate shear induced alignment of short

fiber reinforcement into the desired orientation [174, 175]. Then linear sliding mechanism, which has a resolution of 10 µm, is actuated to generate oscillatory simple shear flow in the produced channels between the micro walls. Under simple shear flow conditions, wide channels result with skin-core morphology which is observed as the fiber alignment in the flow direction around the wall and perpendicular alignment at the center [120, 211]. Disappearance of such morphology was documented by the reduction of the channel thickness with adequate shear rate. In micro injection molding applications, core-free morphology was achieved with channel thicknesses lower than 200 µm [212-214]. In order to attain similar results, layer thickness of SLA curing system was set as 100 µm. Linear oscillation with a 100 µm layer thickness was used to generate simple shear flow and to achieve alignment of fibers onto x-y plane. Fabrication of wall pattern provides a different flow direction and was used to further align the fibers along the channel direction of the wall pattern (See Fig. 3-2).

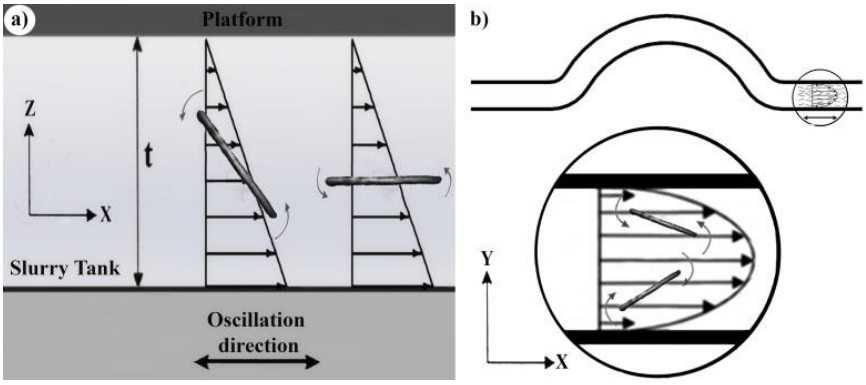

Figure 3-2 Fiber alignment process: (a) Fiber alignment in a simple shear flow as a result of linear oscillation; (b) fiber alignment in a 3d printed wall pattern.

3.2.3 Debinding and Sintering Process of Green Body

3D printed green bodies were debinded at 315 °C for 1 h with the heating rate of 1 °C/min and polymeric binder was removed. After the removal of the binder, the samples

were heated at 1035 °C with the heating rate of 1.85 °C/min, then at 1250 °C with the heating rate of 2.5 °C/min for a continuous sintering process. Finally, the sintering process was employed at 1250 °C for 1 h.

3.2.4 Characterization

In this study, silica particles were used as matrix of the samples and they were reinforced with various fractions of NCCF (0.0, 0.25, 0.5, 0.75, and 1.0 wt%) and short ceramic fibers (0.0, 2.5, 5.0, 7.5, and 10.0 wt%). Standard bar shaped samples (2 x 1.5 x 12 mm) were fabricated by the method previously described. 3-point bending tests were performed for flexural strength analyzes by using Ernest Fullam load frame (EFLF) with a micro bend fixture at room temperature with a speed of 0.5 mm/minute. Flexural strength of the samples was calculated according to equation below:

$$\sigma_F = 3FL/2bd^2 \tag{3.1}$$

where, σ_F is the flexural strength, F is the maximum load, L is span length which is distance two lower anvils, b is sample width, d is sample depth. 15 samples were tested for every fraction and material options. Additionally the microstructure and fracture surface were observed by scanning electron microscopy (SEM).

3.3 Results and Discussion

3.3.1 Fiber Alignment

To investigate the influence of wall direction on fiber alignment, ceramic slurry was subjected to shear rate profile with maximum shear rate of $250\ s^{-1}$ (see Fig. 3-3). Before the shear alignment, the distance between the platform and slurry tank was set for

100 μm and a wall pattern was printed to guide the fibers in the wall direction. Later linear oscillator was actuated to generate the time-dependent shear rate.

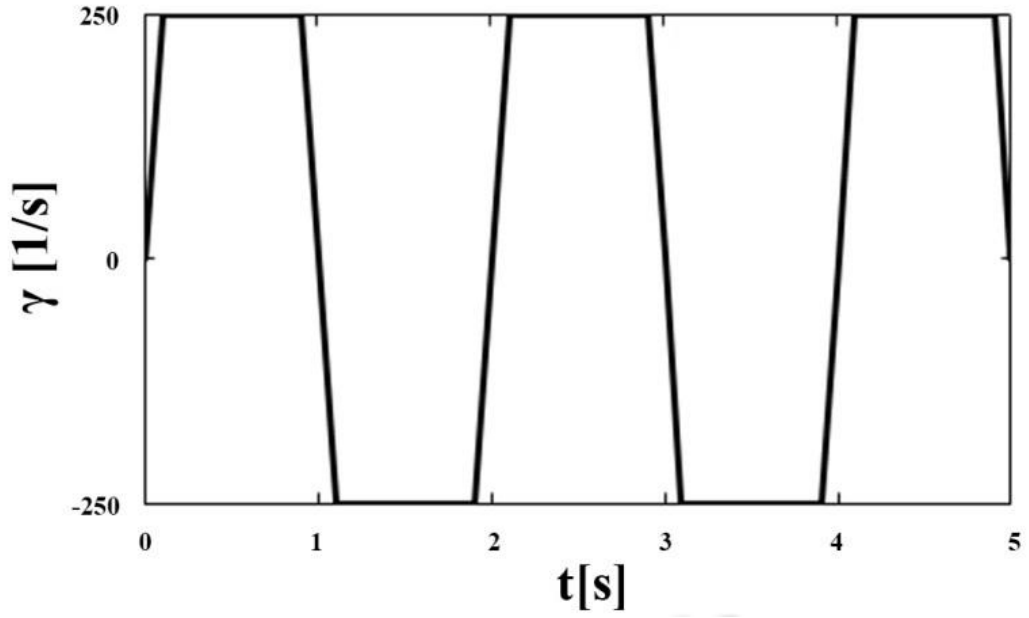

Figure 3-3 The time dependent-shear rate profile which was used during fiber alignment process.

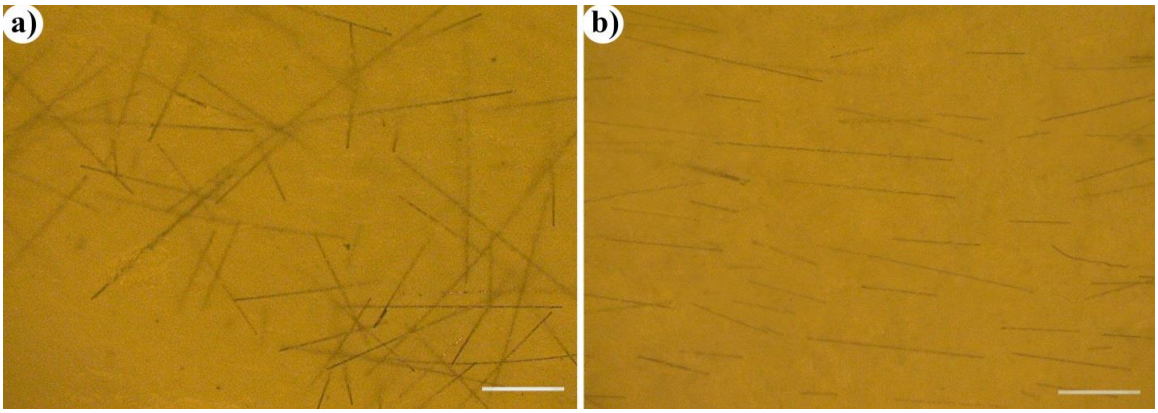

Figure 3-4 Microscope images of fiber alignment and dispersion within 3D printed green part (scale bars are 500 μm): (a) Microscope image of randomly orientated nickel coated carbon fiber; (b) microscope image of aligned nickel coated carbon fiber.

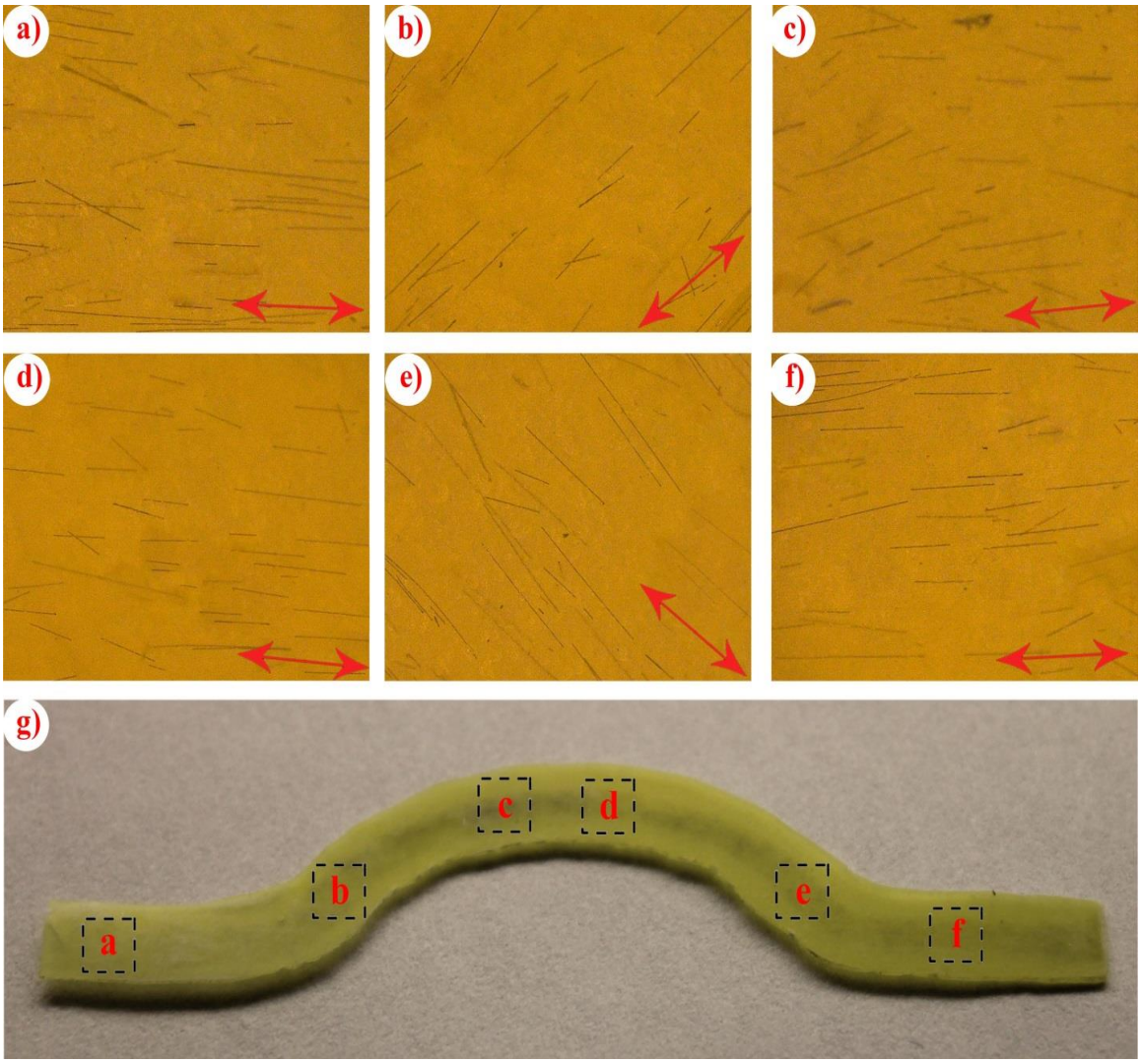

Figure 3-5. Microscope images of fiber orientation distribution along the semicircular channel with different wall angles with respect to oscillation direction: (a) 0°; (b) 45°; (c) 5° right before a quarter curve; (g) Semicircular channel design with location of microscope images of (a-f). Red letters with dashed rectangles indicates the location microscope images are taken. Red arrows on microscope images show the direction of the wall at the local region.

Linear oscillation generates simple shear flow and the flow is redirected by the walls of pattern to obtain fiber orientation direction different than oscillation direction. The direction of the flow in the channel influences the orientation of the short fibers that exist in the slurry. Therefore, it can be used to reposition the fibers and stimulate

alignment in the different direction of applied external force. Fig. 3-4 shows the distribution and alignment of the fibers in the green parts as microscope images. Effect of the oscillation is clearly demonstrated to align the fibers. Also, Fig. 3-5 shows the fiber orientation in different regions of the semicircular channel pattern. Fig. 3-5(a-f) are the microscope images of solidified pattern after linear oscillation. The orientations of the fibers were redirected by the wall pattern to align parallel to wall direction. Fig 3-5(b) and (e) show that the wall pattern aligns the fibers along the wall direction even when the angle between the wall and oscillation direction is about 45°.

3.3.2 Sintering and Microstructure

The dimensions of the green parts were reduced after the sintering process. The shrinkage of the parts was around 5-7% in all directions. Such dimensional change corresponds with 15-20% total volumetric shrinkage of the sintered parts. Fig. 3-6 shows the SEM images of the sintered 3d printed silica and silica composite samples. The microstructure of the sintered unreinforced silica sample surface is shown in Fig. 3-6(a), while Fig. 3-6(b), (c), and (d) show the microstructure of sintered reinforced silica composite sample surfaces. Fig. 3-6(b) demonstrates that fibers in randomly orientated samples are not well dispersed. In Fig. 3-6(c) and (d), it can be seen that carbon and ceramic fibers were aligned in the direction of the wall with the oscillation in similar results to each other. In contrast to randomly aligned samples, aligned fibers were found to be well dispersed. However, there was no visible difference for any influence of sintering process on the fiber orientation. The reinforced ceramic samples display anisotropy in the microstructure as a result of the fiber distribution in X-Y plane. Similar

results can be obtained with other ceramic composite fabrication methods which cannot be utilized during 3d printing [215-217].

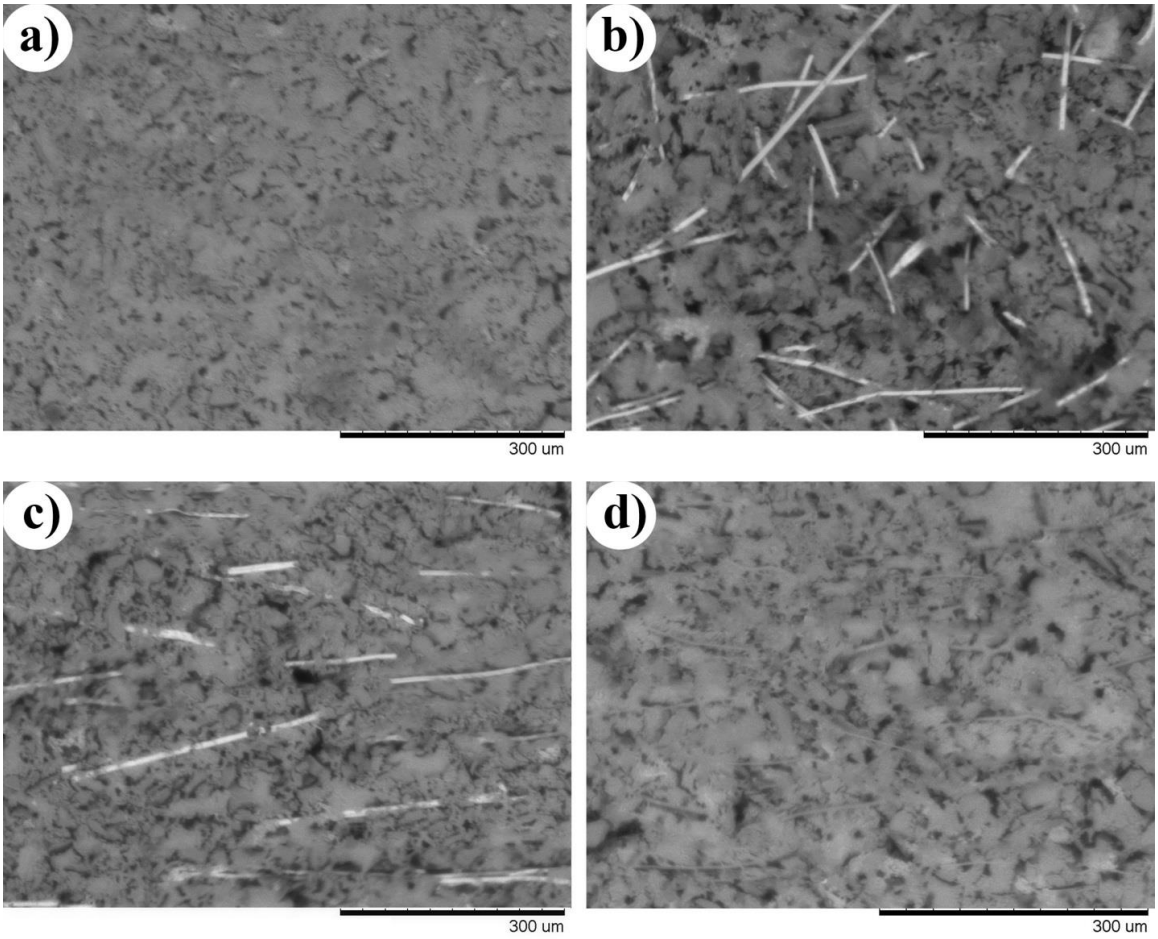

Figure 3-6 SEM images of sintered 3d printed ceramic and ceramic composite samples: (a) SEM image of unreinforced silica sample; (b) SEM image of randomly orientated nickel coated carbon fiber reinforced silica composite; (c) SEM image of aligned nickel coated carbon fiber reinforced silica composite; (d) SEM image of aligned ceramic fiber reinforced silica composite.

3.3.3 Flexural Strength of the Samples

Fig. 3-7 shows the flexural strength of the 3d printed ceramic composites by different weight contents of the carbon and ceramic fibers. The main factors which effect on the flexural strength are the sintering temperature and devitrification process of the fused silica. The flexural strength of 3d printed silica sample without any reinforcement

was obtained as 12.6 MPa. This result is in agreement with some other silica studies [218, 219]. The flexural strength of silica matrix composite increased with the carbon fiber and ceramic fiber content (See Fig. 3-7).

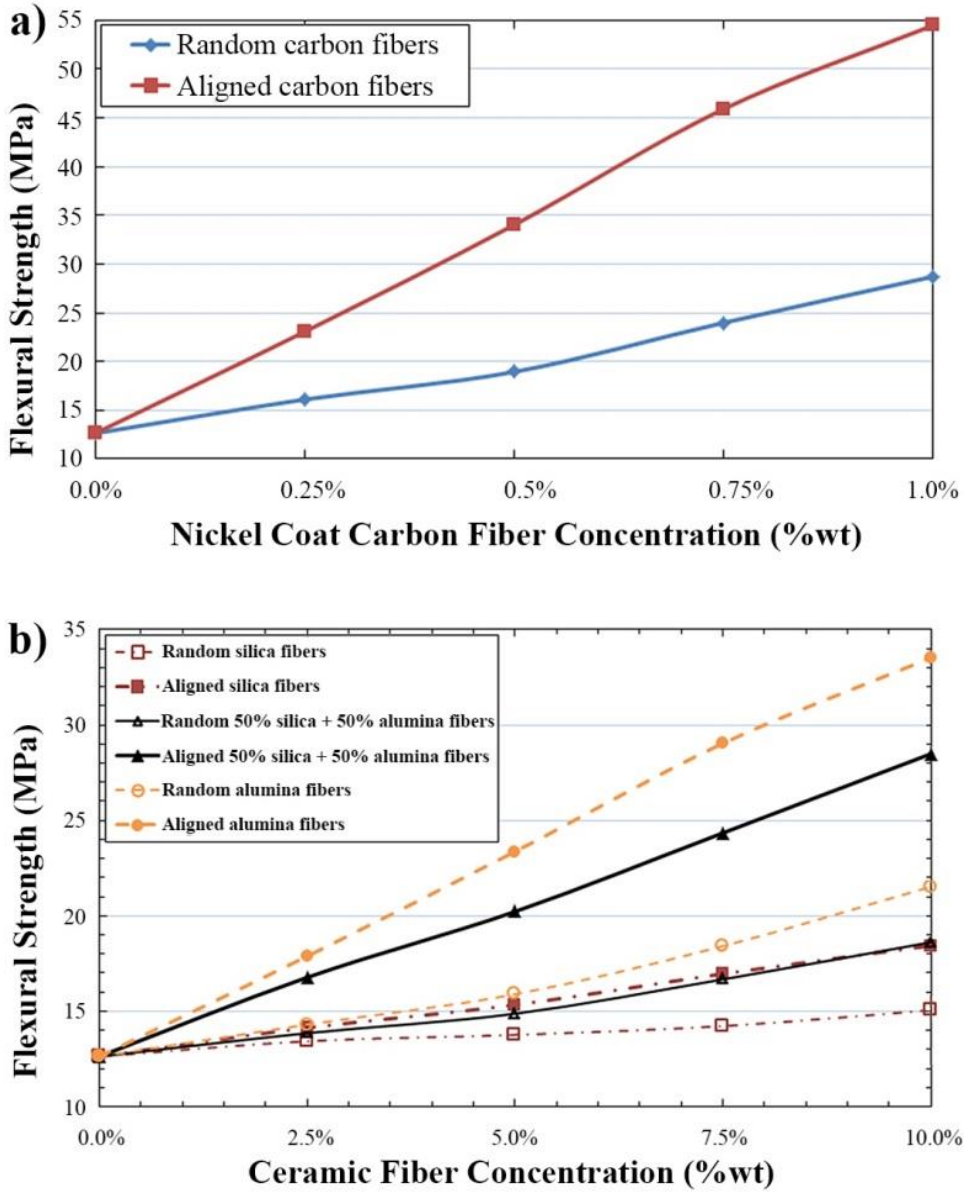

Figure 3-7 The Flexural strength of random and aligned reinforced silica matrix composites with different concentrations and materials; (a) Flexural strength values with different ceramic fiber reinforcement ; (b) Flexural strength values with nickel coated carbon fiber reinforcement.

The addition of 10.0 wt% silica fiber reinforcement enhanced the flexural strength of the samples by 19.8% to 15.1 MPa, while the addition of 10.0 wt% alumina fiber reinforcement improved the flexural strength by 70.7% to 21.5 MPa. The addition of 10.0 wt% half and half mixture of silica and alumina fiber reinforcement increased the flexural strength by 47.6% to 18.6 MPa. On the other hand, 1.0 wt% NCCF reinforcement into silica matrix provided 127.8% enhancement of the flexural strength to 28.7 MPa. The contribution of alignment on to the flexural strength can be understood by the comparison of the aligned and non-aligned samples in Fig. 3-7. The fiber alignment along the length of the test samples improved the flexural strength for all reinforcement types. Improvements were by 26.2% to 18.4 MPa with 10.0 wt% silica fiber, by 95.2% to 33.5 MPa with 10.0 wt% alumina fiber, by 78.6% to 28.5 MPa with 10.0 wt% half and half mixture of silica and alumina fiber, and by 204.8% to 54.5 MPa with 1.0 wt% carbon fiber. These improvements of the flexural strength with increasing fiber alignment and fiber concentration for both carbon fibers and ceramic fibers reinforcement were expected based on general understanding of composites.

3.3.4 Morphologies of Fracture Surface

The fracture morphology of the investigated test samples with NCCF is shown in Fig. 3-8 by SEM images of the fractured surface. The failure of fiber reinforced composite materials mainly involves matrix failure, the fiber/matrix (F/M) interface debinding, fiber failure, fiber pull-out, and delamination. When a crack grows and spreads in the matrix, the process can trigger a fiber failure or F/M interface debinding. The F/M interface debinding can also result with fiber pull-out [220, 221]. In the case of this study of fiber reinforced ceramic composite, the layers of 3d printing process were

not visible or detectable on the fracture surface. There was also no evident delamination, layering, or any crack propagation between 3d printed layers. The fracture surface consisted of both fiber pull-out and fiber failure as shown in Fig. 3-8. However, fiber pull-out was more prevalent than fiber failure. Fiber pull-out points out that the F/M interfacial bond in the samples were not durable enough to sustain the stresses until fiber failure takes place. Improvement of the interfacial bond can further improve the strength of the samples.

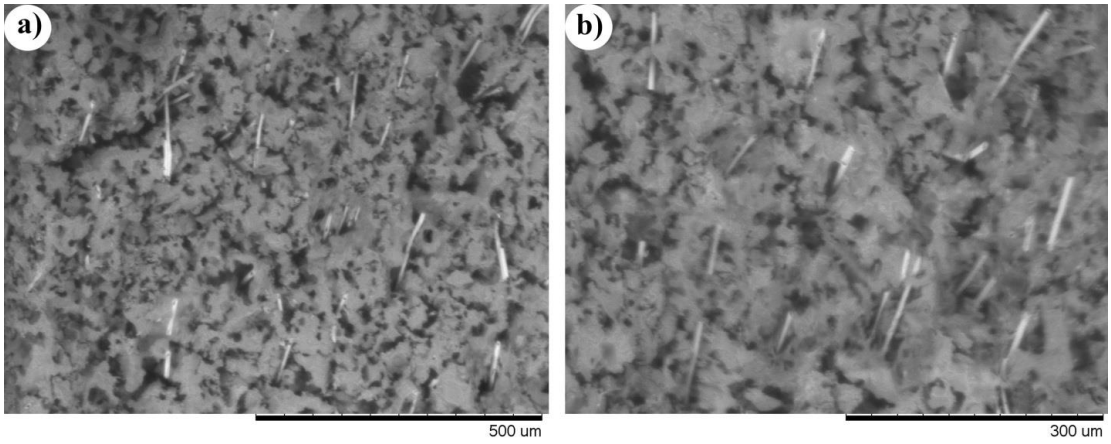

Figure 3-8 Fracture surfaces of the nickel coated short carbon fiber reinforced ceramic composite samples; (a) 180x magnification; (b) 250x magnification.

3.4 Conclusions

A DLP based SLA device, incorporated with the shear-induced fiber alignment apparatus was utilized to fabricate fiber reinforced silica matrix composites. 0.0-1.0 wt% NCCF and 0.0-10.0 wt% alumina, silica, half and half mix of alumina and silica were used as reinforcements for the silica matrix. The shear-induced fiber alignment as a result of oscillation was demonstrated. Additionally, printed wall pattern, such as channels with circular path, was shown to reorient the fibers into different directions from the oscillation direction. Up to 45° difference between alignment and oscillation direction

was successfully achieved during this study. Both ceramic fibers and NCCF responded to the alignment process similarly and got aligned along the wall direction.

The EFLF was employed for the flexural strength analyzes of the samples. The flexural strength test specified the expected increase of the strength along the alignment direction with the shear induced alignment of the reinforcement. The alignment improved the flexural strength further up by 26.2%, 95.2%, 78.6%, and 204.8% with silica, alumina, alumina-silica mix, and NCCF with used maximum weight fractions, respectively. Both fiber failure and fiber pull-out were existed in the fracture surface, but fiber pull-out was the main fracture mechanism.

In summary, shear induced alignment with oscillation and wall pattern was shown to be also viable for ceramic applications of SLA. This method can be utilized for production of anisotropic ceramic pieces with different fiber orientation and pattern on each layer.

Chapter 4: Short Nanofiber Alignment in Polymer Composites

4.1 Introduction

One dimensional (1D) nanoscale particulates (NPs) such as nanorods, nanofibers, and nanotubes have been widely used for medicine [222], electronics [223, 224], and photonic applications [225, 226]. NPs are combined with matrix in a controlled dimension and percentage to improve various properties, such as mechanical, electrical, and thermal properties, thus there is also growing interest in nanocomposites [227-232]. These improvements are directly related with the material, dimensions, and orientation distribution of fibers. Orientation distribution with respect to fiber length and concentration is one the most important factors that influences the ultimate strength of a fiber-reinforced composite structure. The influence of fiber length, orientation and distribution on tensile strength was studied by Fu and Lauke analytically [117, 233]. Analysis of Fu and Lauke showed that strength of the composites increases with increase in fiber length, interfacial adhesion strength and fiber orientation. Increase in fiber orientation was described by the decrease in mean fiber angle relative to direction of the force. Along the alignment direction, not only was the strength of material increased but also thermal and electrical conductivity of material increased [234]. Therefore, 1D NPs have become increasingly attractive for researchers. Different methods of aligning 1D nanostructures exist in literature[235], such as electric field induction [140, 141],

magnetic field induction [234, 236], chemical surface modification[237], nanoimprint lithography[238], flow induced alignment[239].

3D printing is a manufacturing process of making complex solid objects from a digital file in the form of successive layers. The addition of fiber reinforcement into 3d printing material was demonstrated successfully to produce reinforced polymer composite (RPC) for Fused deposition modelling (FDM) [8, 10], Stereolithography (SLA) [11, 12], and inkjet printing [13]. Flow induced alignment is easily achievable for FDM and inkjet printing. The FDM and inkjet printing include a nozzle where material flows through. Shear generated within the nozzle provides partial alignment of the short fibers in the direction of the extrusion [8, 10, 13]. On the other hand, alignment of the short fibers during SLA 3d printing was demonstrated by magnetic and acoustic fields [11, 12]. However alignment by electric or magnetic fields limit the material of reinforcement because they require particles with specific electrical and magnetic properties. Acoustic field is a useful method to distribute and pattern particles towards pressure nodes or anti-nodes in the matrix medium [12]. Although acoustic field manipulates the particles to form distinctive long parallel strand of lines, the individual fibers have a degree of misalignment which increases with higher particle volume fractions [21].

In this chapter, we demonstrated that shear induced alignment can be used instead of magnetic and acoustic alignment to have better distribution and orientation of fibers without material constraints. We developed a new method to use flow induced alignment during Digital Light Processing (DLP) based SLA 3D printing. Linear oscillatory actuation mechanism (LOAM) was combined with SLA device to generate Couette flow

which was used for alignment. Aluminum oxide nanofibers (AONWs) were treated with silane coupling agent and were used as an additive to enhance interfacial bond between NPs and matrix material. The printed wall pattern was also accompanied with LOAM to provide additional alignment of the nanofibers. Our method of using shear induced alignment provides a simple and cheap method for alignment of 1D NPs during SLA 3D printing.

4.2 Materials and Methods

4.2.1 Materials

Acrylate based photocurable polymer purchased from Madesolid was used as a matrix for nanofiber reinforced polymer composite (NFRPC). The density and the viscosity of the resin were provided by the supplier as $1.12\ g/cm^3$ and 361 cP at 20°C. AONWs with 2-6 nm diameter and 200-400 nm length were purchased from Sigma-Aldrich and were used as the reinforcement of the composite. AONWs and photocurable polymer are two dissimilar materials and a coupling reaction is necessary to provide a chemical bond between them. In order to couple the matrix and nanowires, 3-(Trimethoxysilyl)propyl methacrylate (TMSPMA) purchased from Sigma-Aldrich was used as a coupling agent.

Aluminum oxide is a widely used metal oxide of great importance in the industry due to its high strength, chemical stability, electrical and thermal insulation, and corrosion resistance. AONWs also attracts attention in the research field for some experimental and commercial composite application with high performance [240]. The addition of nanowires is intended to improve the mechanical, thermal, or chemical properties compared to the neat matrix. These enhancements are significantly affected by

introduction of surface coupling for better interfacial adhesion. Aluminum oxide is cheaper than other alternative options and can be functionalized to improve interfacial interaction between aluminum oxide and polymer [228, 241].

To introduce coupling agent onto the surface of AONWs, TMSPMA was dissolved in 95% ethanol – 5% water solution with acetic acid to lower pH to 4.5-5.5. The amount of silane, which was added to solution, was calculated according to Eqn. 4.1 [242]:

$$X = \frac{A_{ss} m_{nw}}{\omega} \tag{4.1}$$

where, X is the amount of silane, m_{nw} is the amount of nanowires, A_{ss} is specific surface area of nanowires, and ω is the specific wetting surface of silane. In this study, the specific wetting surface of silane was $\omega = 315\ m^2/g$ and the specific surface area of nanowires was $A_{ss} > 360\ m^2/g$. As a result, the minimum necessary amount of silane to treat 1 g of nanowire powder was calculated as 1.14 g. AONWs was initially dehydrated at 60°C for 24 hours and was silanated in the solution by stirring for 5 minutes at room temperature. Then the mixture was separated by decanting the solution. The nanowires were rinsed twice with acetone and silane layer was post cured for 2 hours at 60°C [241]. Photocurable resin combined with untreated and treated nanowires in the ratios of 1, 2, 3, 4, and 5 wt% were used for the control and test specimens. Possible existing bubbles in the suspension were removed by vacuum degassing. Additionally ultrasonic cavitation was used for better dispersion of the nanowires into photocurable resin.

4.2.2 Design Setup

Fig. 4-1 shows the designed DLP based SLA desktop 3D printer. A simple lateral harmonic motion mechanism was also incorporated to generate the Couette flow. To

manipulate the orientation of the nanofibers, we first fabricated patterns of micro channels specifically designed to align the fibers in the desired direction. Then we used linear harmonic oscillation to align the fibers. It was observed that nanowires with 2-6 nm diameter and 200-400 nm length were responding to the alignment process. The designed 3D printer can manufacture complex structure with minimum feature size of 50 μm.

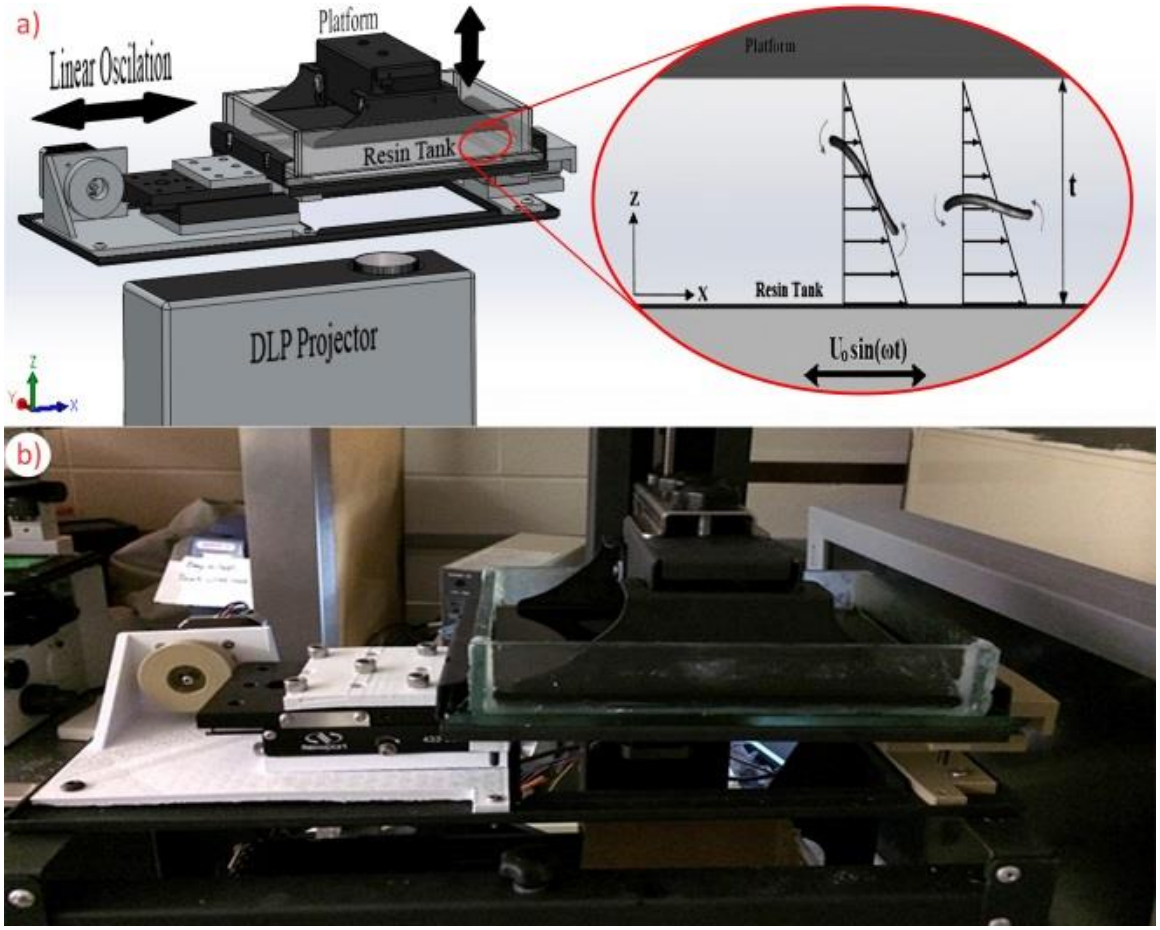

Figure 4-1 DLP based SLA desktop 3D printer and incorporated linear harmonic oscillator mechanism. (a) 3D demonstration of the system consists of linear oscillation mechanism, platform, resin tank, and DLP projector. (b) Photo of 3D printer during linear oscillation process

DLP based SLA desktop 3D printer consists of a linear sliding mechanism oscillating with $U_o \sin(\omega t)$, a resin tank with the dimensions of $140 \times 190 \times 36\ mm^3$, DLP projector and a platform with the surface dimensions of $130 \times 165\ mm^2$. A linear slide is connected to a cam mechanism which is driven by a stepper motor. A schematic demonstration of oscillatory Couette flow generated by the system is shown in Fig. 4-1a.

4.2.3 Fiber Alignment

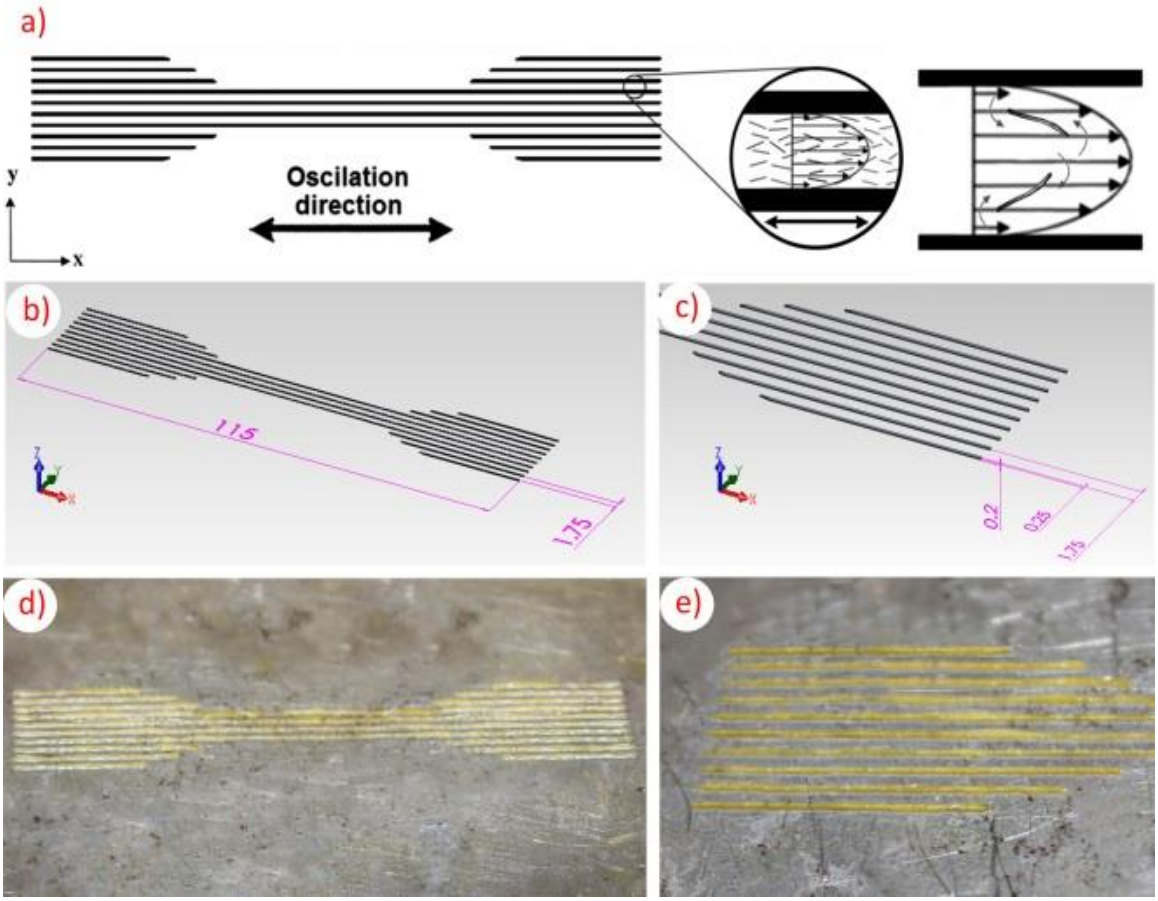

Figure 4-2 Three dimensional and optical images of wall pattern for test specimen fabrication; the width of the walls is 250 μm, the distance between walls is 1.75 mm, and the height of the wall is 200 μm

Fiber motion and orientation in a simple shear flow has been studied extensively in literature [120, 147, 243-246]. Without a solid boundary, a single fiber in the simple

shear flow will tend to align in the shear direction with periodic rotations. Such periodic tumbling motion in simple shear flow was described by Jeffery's orbit [147] and was validated for diluted suspensions [243, 244]. The characteristics of fiber motion are affected by the existence of a solid boundary. When fibers are near a solid wall, they align better and faster than what Jeffery's equation predicts [120, 245, 246]. In addition, if aspect ratio of fibers increases, they cannot be considered as rigid rod. This creates a sudden decrease in the period of the motion. General behavior of a flexible fiber in a shear flow was demonstrated by Arlov, Forgacs & Mason [246].

In a simple shear flow, channel width and thickness affect the alignment significantly. In wide channels, while fibers align in the flow direction near the walls, they orient perpendicular to the flow at the center of the channel [120, 211]. The region in the center of the channel is called core layer. The regions near the walls are called skin layers. If the channel is thin enough, the core layer will disappear and fibers will perfectly align in the flow direction. In similar studies for micro injection molding, skin-core morphology was still visible in the range of 300-500 μm [212, 247, 248]. As the thickness goes below 200 μm, it resulted with core-free morphology [212-214]. Thickness is not the only factor which effects fiber alignment. Without sufficient shear rate, even the thicknesses down to 100 μm cannot provide core-free morphology [249, 250]. In our device, we set the thickness between platform and resin tank as 200 μm. We studied different velocity and frequency settings to find optimal shear rate and frequency values for sufficient alignment. The result of experimental study for influence of shear rate on fiber orientation tensor is shown in Figure 4-4a. Figure 4-4b illustrates time dependent shear rate profile at a maximum shear rate of (γ_{max}) $314\ s^{-1}$ and frequency

(ω) of 1 Hz which used for ultimate strength tests. We also proposed the use of printed wall patterns to manipulate the local flow of resin which is driven by oscillation. While the oscillation creates simple flow which provides alignment on x-y plane, the printed wall pattern provides additional alignment along channel direction. The wall pattern is designed parallel to the oscillation direction to align fibers in same direction as shown in Fig. 4-2.

4.2.4 Fabrication of Test Specimens and Mechanical Testing

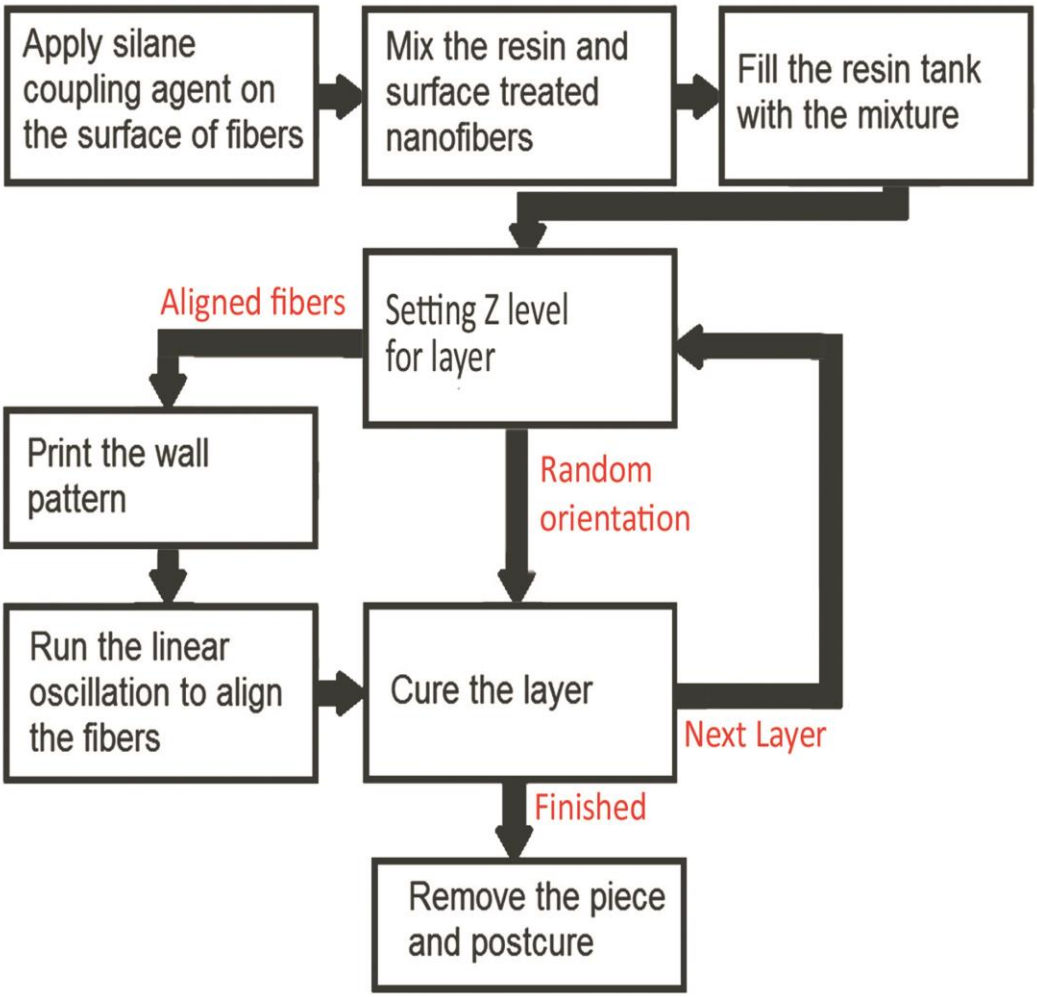

Figure 4-3 Flow chart of the fabrication process

Fig. 4-3 shows the diagram of the fabrication steps for test specimens. First, TMSPMA was applied on the surface of the AONWs as described in Section 4.2.1. Then, treated nanowires were mixed with photocurable resin with 1, 2, 3, 4, 5 wt% fraction ratios. Prepared suspensions were placed in the resin tank to fabricate test specimens. The distance between platform and the resin tank was set for the layer thickness. The layer thickness was 200 μm for these test specimens. The wall pattern shown in Fig. 4-2 was printed to guide the fibers in the oscillation direction for fabrication of the layers with aligned fibers. Lateral linear oscillator was turned on to align the fibers. Time-dependent maximum shear rate of $314\ s^{-1}$ was generated by lateral oscillation mechanism for 1000 cycles (Fig. 4-4). After that the resin was exposed to the projected image from the DLP projector and was cured. The last three processes, consisting of the wall pattern fabrication, alignment by oscillation, and finishing the layer by curing, were repeated for every layer. Following the removal of the specimens from platform, they were post-cured further and ready for mechanical testing. The fabrication steps for randomly oriented specimens do not include printing the wall pattern and linear oscillation which were only necessary to align the fibers.

Uniaxial tensile tests were performed at room temperature (20–25ºC) with constant 1 mm/min displacement rate. Nominal strain rate was 0.1 mm/mm·min at start of the test. All data was collected as an average of 5 independent printed specimens. The shape and dimensions of specimens are illustrated in Fig. 4-5. All specimens were printed with 0.2 mm layer thickness and total of 20 layers

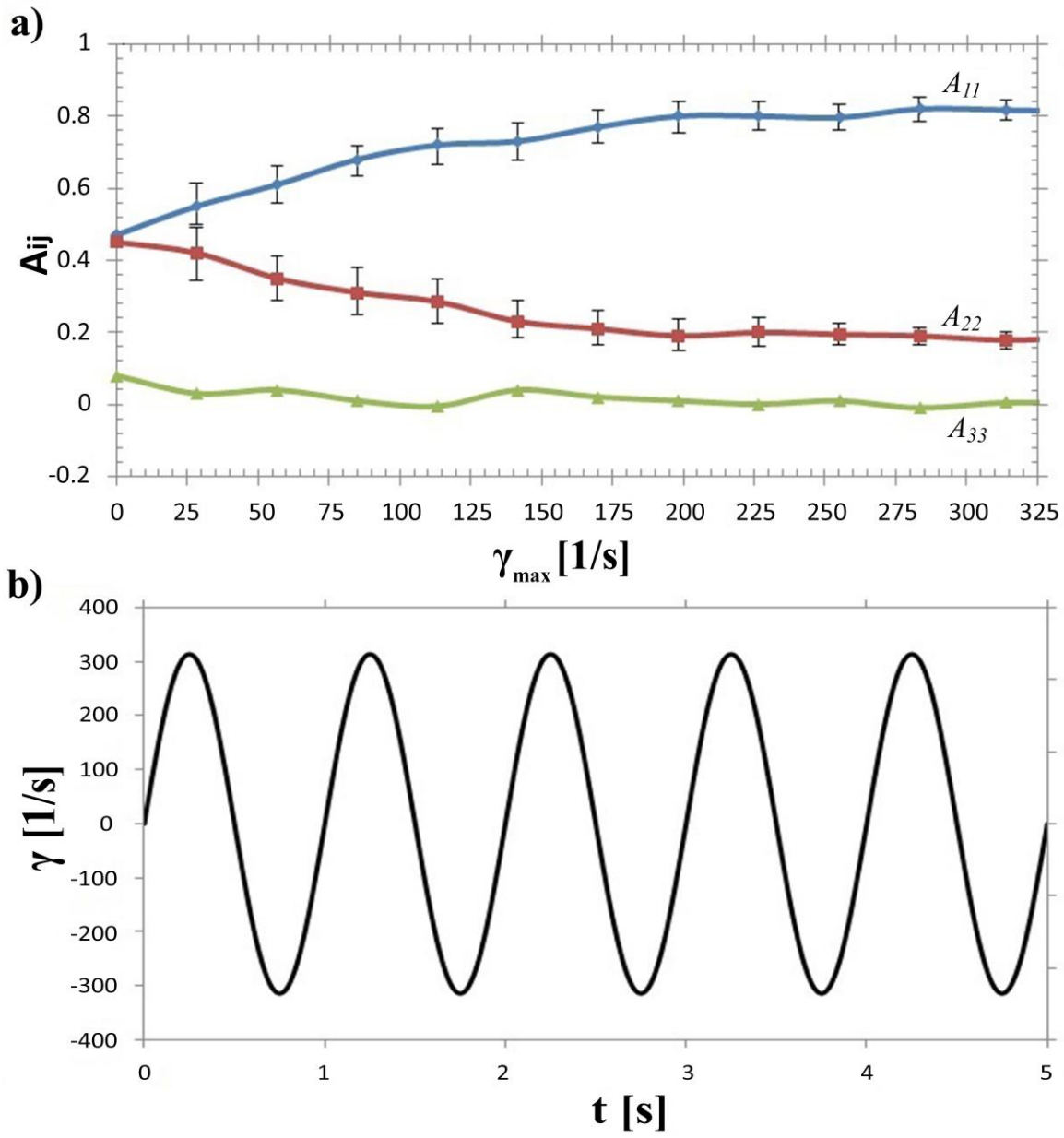

Figure 4-4 Demonstration of shear rate profile and influence of maximum shear rate and frequency on fiber orientation tensor. (a) The influence of maximum shear rate γ_{max}, on orientation tensor at frequency of f = 1Hz and 5wt% AONWs loading, (b) The time dependent- shear rate profile which was used in ultimate strength tests,

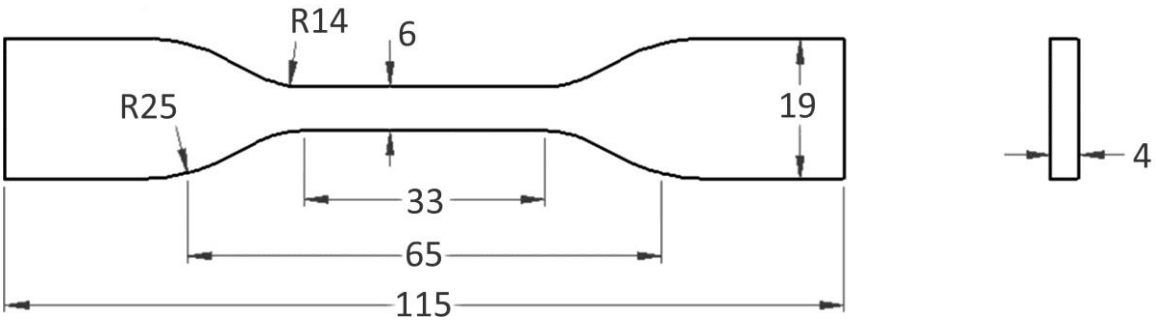

Figure 4-5 Geometry of the tensile test specimens; dimensions are in millimeters

4.3 Results and Discussion

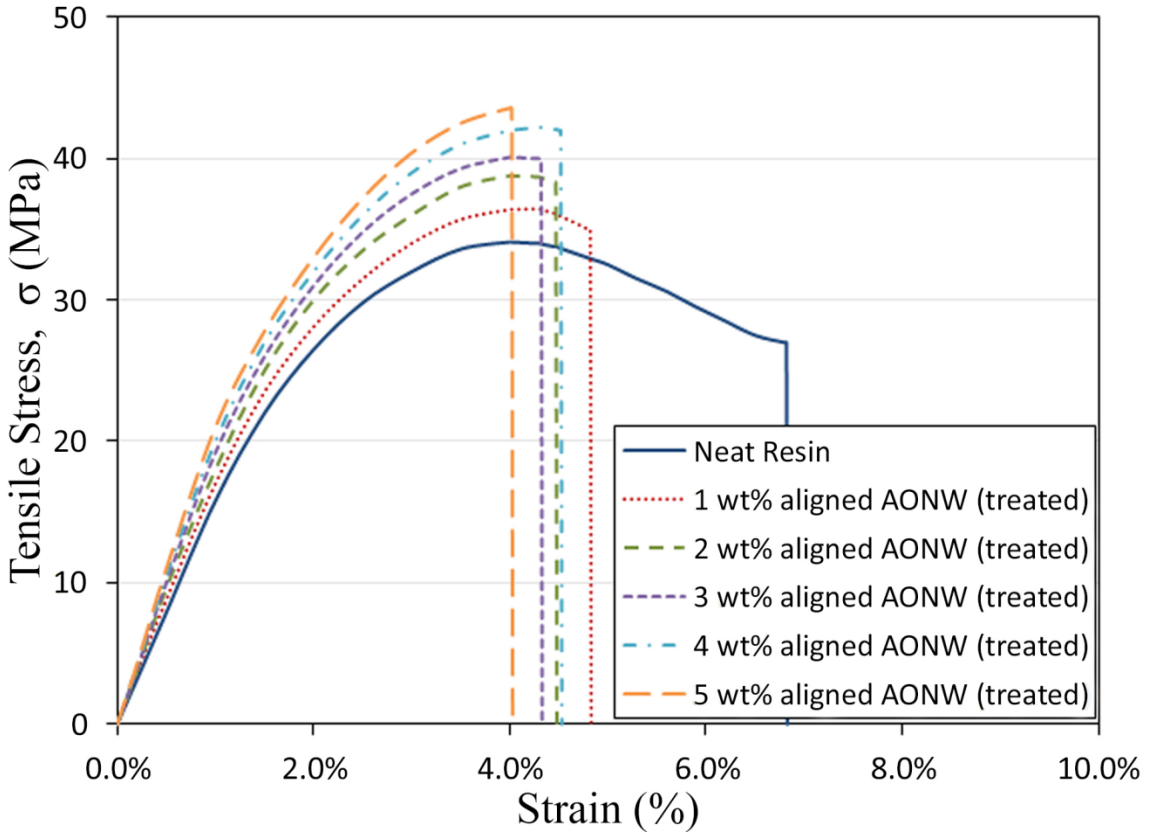

Figure 4-6 Tensile stress-strain curves of the surface treated aligned AONW reinforced nanocomposites.

Tensile stresses-strain curves of nanocomposites are plotted out in Fig. 4-6. This includes unreinforced photocurable resin for comparison and it shows that tensile strength of the specimen increases with the increasing nanofiber content.

The tensile properties of the aligned and randomly orientated nanocomposites are plotted in Fig. 4-7. Fig. 4-7(a) shows that the addition of reinforcement gradually decreases the tensile strength without surface treatment as it was expected. Significantly larger surface areas of the nanowires compared to similar masses of larger scale particles causes greater aggregation of NPs. It was observed that the use of surface coupling agent improves interfacial interaction between AONWs and polymer matrix. Subsequently it enhances the tensile strength and elastic modulus when the reinforcement has a higher stiffness than the matrix (as shown in Fig. 4-7(a)). With the use of the surface coupling agent, 5 wt% randomly orientated AONW reinforcement (1.5 % volume fraction) provides 15% improvements in tensile strength and 20% improvement in elastic modulus of the nanocomposite. The comparison between randomly orientated sample with 5wt% and the specimen with 5wt% align AONWs clearly shows the effect of orientation distribution on ultimate strength of NFRPC. The alignment of fibers provides additional 13% improvement to the elastic modulus and ultimate strength of NFRPC in the alignment direction (as shown in Fig. 4-7(a) and (b)). This enhancement of ultimate strength with the increase in fiber orientation is in line with general knowledge of composite materials. 5 wt% aligned AONWs in nanocomposite with surface treatment enhances tensile strength 28% and elastic modulus by 34%.

The dispersion and alignment of AONWs in the polymer matrix are illustrated in Fig. 4-8 as transmission electron microscopy (TEM) and in Fig. 4-9 as scanning electron microscopy (SEM) images. Fig. 4-8a,b,c,d,e,f show the TEM images illustrating dispersion and alignment of the samples which were also used for the orientation distribution analysis. The AONWs were evidently shown to change from random

orientation to being aligned along the shear direction. However, there was no visible difference in the fiber orientation distribution between aligned 1, 2, 3, 4, 5 wt% fraction ratio specimens. Analysis does not provide any evidence for influence of nanowires loading on the orientation distribution.

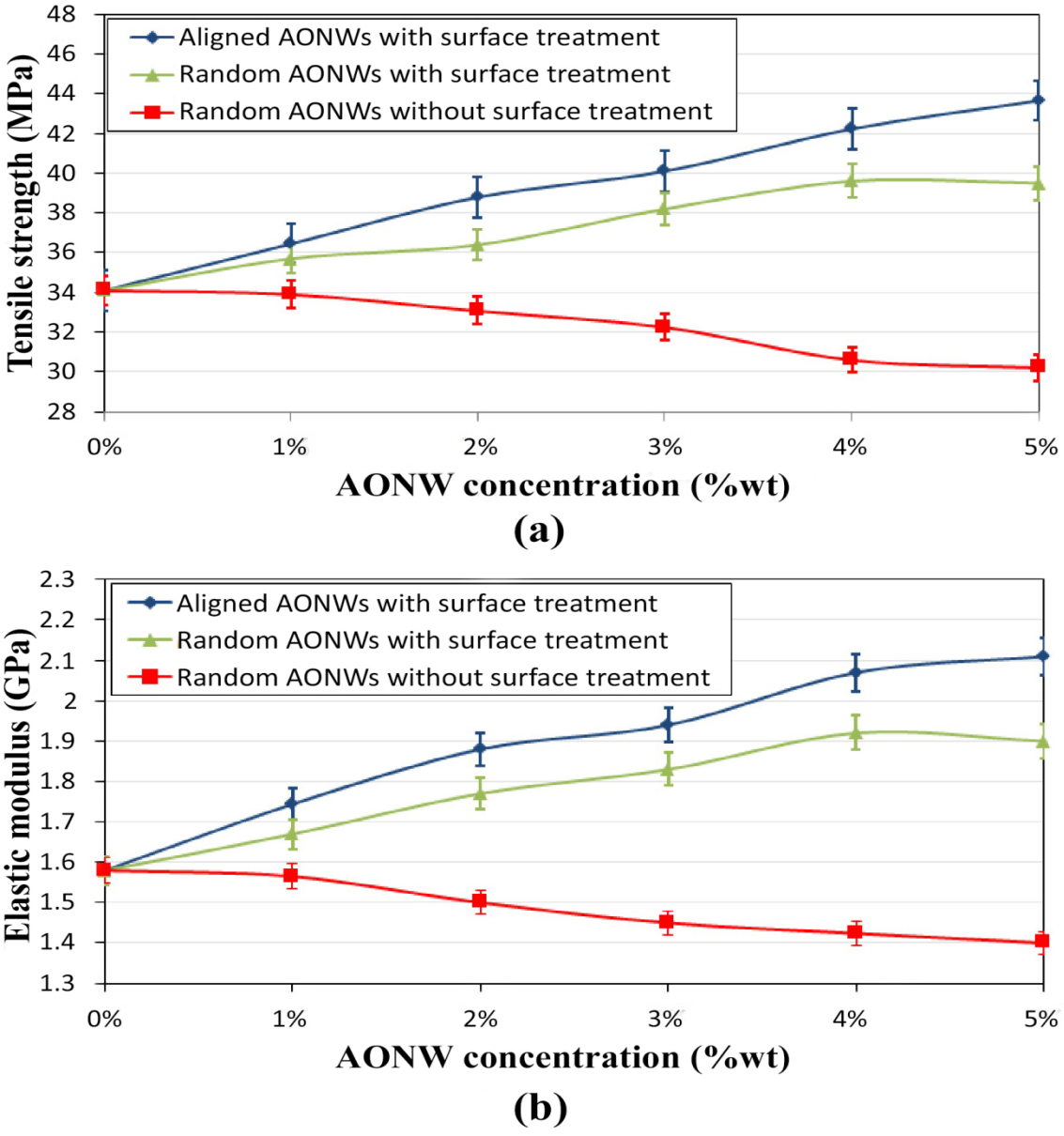

Figure 4-7 Tensile strength and elastic modulus of random and aligned AONW reinforced composites with different concentrations; (a) Tensile strength, (b) Elastic modulus.

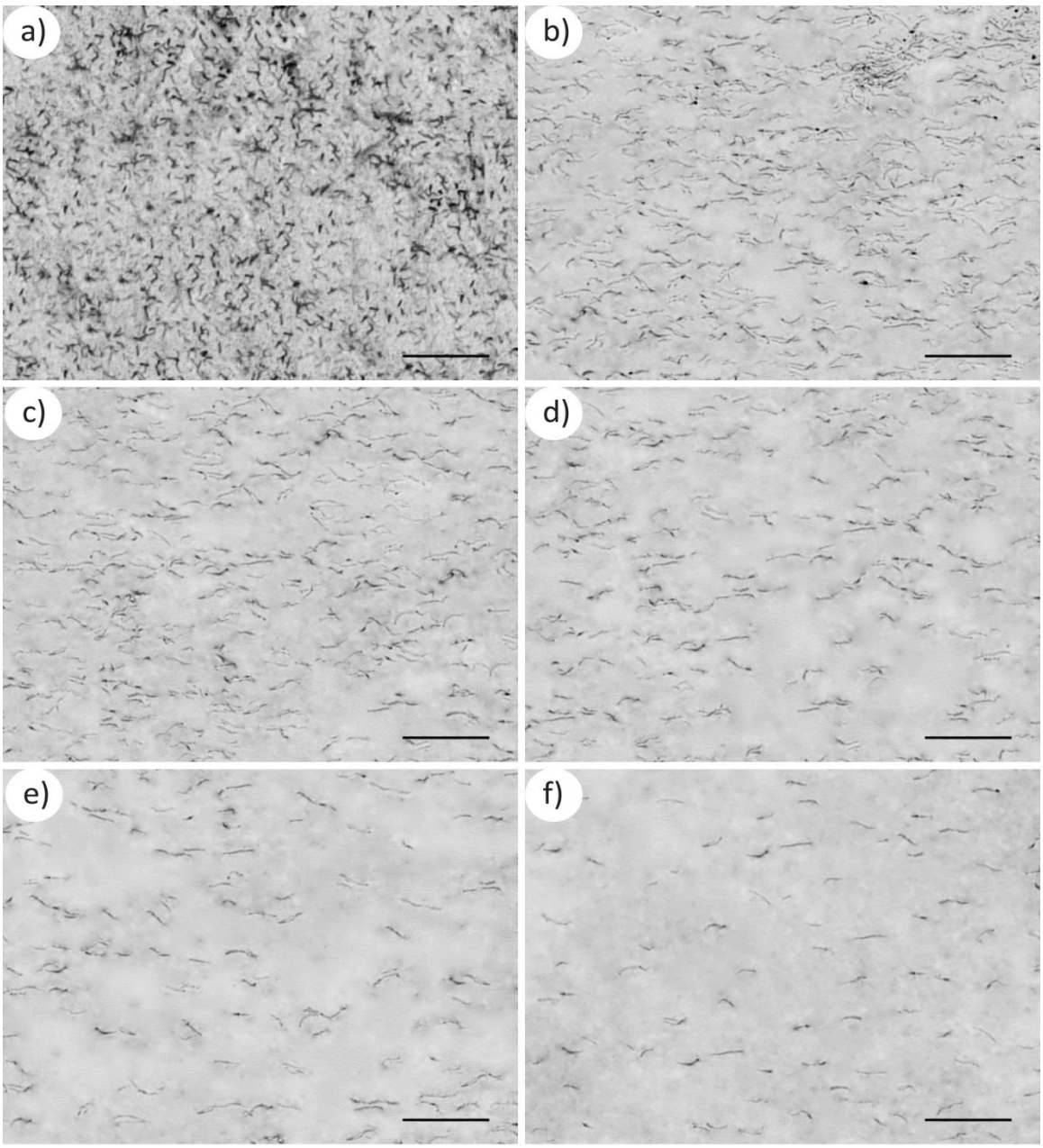

Figure 4-8 TEM images of nanowire alignment and dispersion within printed components (Scale bars are 1 µm); (a)TEM image of randomly orientated AONWs, (b)TEM image of aligned AONWs with 5wt% reinforcement, (c) TEM image of aligned AONWs with 4wt% reinforcement, (d) TEM image of aligned AONWs with 3wt% reinforcement, (e) TEM image of aligned AONWs with 2wt% reinforcement, (f) TEM image of aligned AONWs with 1wt% reinforcement..

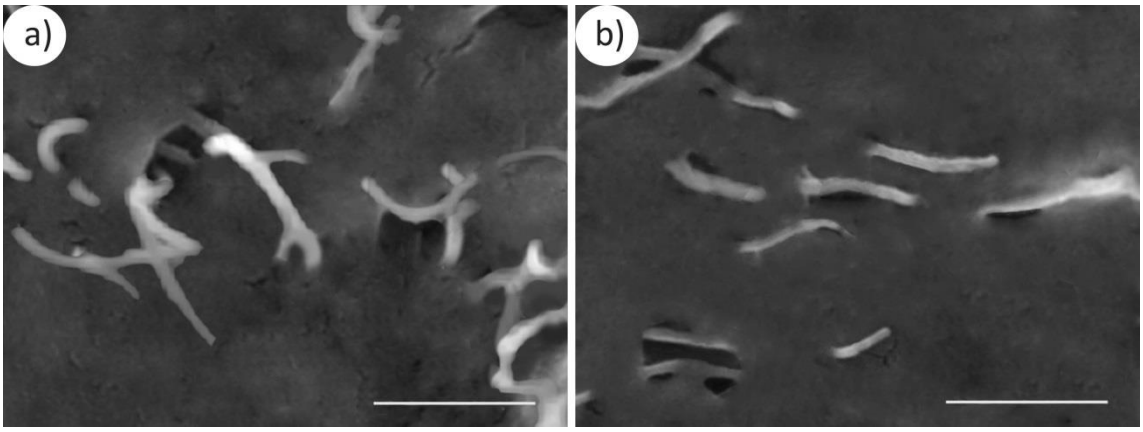

Figure 4-9 SEM images of nanowire alignment within printed components (Scale bars are 50 nm); (a) SEM image of randomly orientated AONWs, (b) SEM image of aligned AONWs with 5wt% reinforcement.

4.4 Conclusions

Shear-induced fiber alignment technique was used to fabricate AONW reinforced polymer composite. DLP based stereolithography desktop 3D printer, incorporated with lateral linear oscillation mechanism, was designed and built to demonstrate this technique. Polymer nanocomposite specimens, containing 1–5wt% of AONWs, were prepared with silane surface coupling agent to enhance interfacial interaction between nanofibers and matrix. The oscillation mechanism combined with printed wall pattern was used to generate shear induced unidirectional alignment in test specimens. Tensile tests showed that Young's modulus and the tensile strength enhances with the increase in nanowire concentration and alignment of the nanowires. Only with 5wt% (1.5% by volume) nanofiber, composite showed a 28% improvement in strength achieved through the alignment of the nanowires. Further improvement can be expected to be achieved by increasing the volume fraction of the nanofibers. Alignment of the fibers can be achieved in any direction on x-y plane by changing the wall pattern.

Comparisons between different shear rates, frequencies, AONWs loading were performed and their influence on orientation distribution of AONWs and ultimate strength investigated. The TEM images seen in Figure 4-8 show that AONWs were well dispersed in polymer matrix and were aligned in the desired direction with this shear approach. Shear rates were illustrated to have significant influence in AONWs orientation (Figure 4-4a) while frequency and AONWs loading has almost no visible effect on orientation.

In summary, this novel research demonstrates a method for nanofiber alignment during rapid prototyping. This method has potential for the production of tailored anisotropy in fiber reinforced nanocomposites. It might also be used in applications such as high strength, electronic, photonic, and flexible metamaterials.

Chapter 5: Acoustic Patterning for 3D Embedded Electrically Conductive Wire during Stereolithography

5.1 Introduction

3D printing or additive manufacturing (AM) technology is a process of manufacturing complex three dimensional (3D) structures from a digital file with various materials. Models, which are stored as digital CAD files, allow easy customizations and adjustments. Software uses cross-sections of a digital file to generate layers with finite thickness and additional layers are deposited to build the object one layer at a time [5, 24]. Recently, AM has advanced to be more affordable, very useful and widespread in manufacturing finished products. Therefore, the research attention has shifted on more sophisticated products and systems, with applications across varied industries such as, medical [4], electronics [5-7], and composites [8, 9].

Fuse deposition modeling (FDM) method is becoming fairly popular as a result of its low cost and reliability compared to the other approaches. However, its material constraints to deposit, relatively poor resolution and mechanical properties of the finished products limit the suitability of the method for practices especially for high strength applications [251]. Additive of nano- or microscale reinforcement of fiber or particles into the extruded material enhances the performance of the finished product and can deliver extra functions, such as electrical conductivity [5-8, 10]. FDM is a slower process

compared to stereolithography (SLA) and does not provide desired surface finish. Inkjet printing, which is a relatively young adaptation of AM, can provide better speed and surface finish. However, existence of particles increases the probability of clogging in the extruding or inkjet heads, which are already prone to clogging. Therefore, alternative options for spatial control of fiber or particulate positions can address some issues of existing methods.

A variety of methods for particle manipulation and patterning in suspension have been used in recent years. Particle manipulation and fiber alignment have been demonstrated with flow-induced alignment [8], magnetic alignment [11], dielectrophoresis [17], and acoustic field [12]. The use of flow-induced alignment requires a flow through nozzle which is prone to clogging [252], while magnetic alignment and dielectrophoresis require particles to have necessary magnetic or electric properties to be aligned. On the other hand acoustic alignment provides better control over the distribution and orientation of particulates without too many material and engineering limitations. In this study, a method is introduced to use acoustic alignment of nanoparticles to produce 3d printed parts with embedded conductive micro structures. Acoustic forces have been used to generate micro scale structures during SLA 3d printing by Llewellyn-Jones et. al [12]. They used a modified top down laser based SLA printer to produce 1mm thick single layer composite samples in order to investigate improvement in strength. In contrast to their study, a bottom up Digital Light Processing (DLP) based SLA printer was developed to produce multiple layered pieces with embedded conductive microstructures. A hexagon shaped acoustic tweezer was designed to spatially position and manipulate the particles. The conductivity of microstructures was

investigated for different particle materials and a method of curing partial regions of aligned pattern was applied to generate embedded, multilayered, complex conductive microstructures.

5.2 Method and Experimental Setup

5.2.1 Design concept

The DLP based SLA 3d printer which consists of DLP projector, optical system, platform, and acoustic tweezer (see Fig. 1a) was designed and manufactured. The DLP based projector was used as the source of light to cure photocurable resin inside the acoustic tweezer. The optical system reduced the size of projected image and pixel size. The reduced pixel size, which corresponds with SLA resolution, was set to 20μm. The platform is connected to a linear stage. The linear stage has 2.5 μm minimum step length and was used to set layer thickness. The 3d printer was incorporated with the hexagon shaped acoustic tweezer to align micro- or nano- particulates and generates microstructures. A hexagon shaped acoustic tweezer, which is shown in Fig. 1b, was made by assembly of glass pieces. The width which refers the distance between parallel sides of the inner cavity was design to be 50mm. The six piezo plate actuators (Steiner & Martins Inc.) were placed in the inner walls of the tweezer. The signal was generated by arbitrary waveform generator (HP Agilent 33250A) and then amplified to actuate piezo plates. The signal was generated at resonant frequency of $f = 2.33\,\text{MHz}$ with the amplitude of $V_{pp} = 100\text{V}$. Actuated piezo plates created bulk acoustic waves (BAWs) in the media to align the particulates in desired microstructure. The photocurable resin with low viscosity was chosen as a media for less acoustic attenuation. The specified actuation signal corresponds with 600 μm wavelength in the resin.

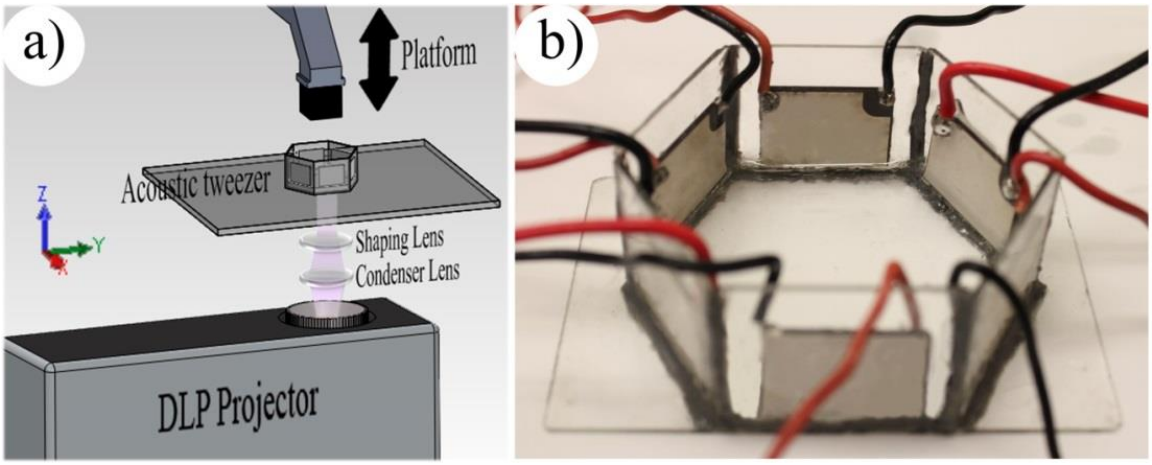

Figure 5-1 Setup of DLP based SLA 3D printer incorporated with the hexagon shaped acoustic tweezer; (a) 3d schematic of 3d printer setup, (b) the hexagon acoustic tweezer with placed piezo plate actuators.

5.2.2 Acoustic Alignment

In the acoustic tweezer, two opposite corresponding piezo plates were actuated to create a standing BAW. In a standing BAW, the acoustic radiation forces are maximized and these forces drive the particles to the closest node or anti-node of the standing BAW. This action is mainly depended on the location, size, compressibility, and density of the particles. The primary acoustic radiation force on a single particle with a radius much smaller than the wavelength suspended in an inviscid fluid can be derived as [186];

$$F_{PRF} = -\frac{2\pi V_p E_{ac}}{\lambda}\phi \sin\left(\frac{4\pi x}{\lambda}\right) \tag{5.1}$$

$$\phi = \frac{5\rho_p - 2\rho_f}{2\rho_p + \rho_f} - \frac{\beta_p}{\beta_f} \tag{5.2}$$

$$E_{ac} = \frac{{p_a}^2 \beta_f}{4} \tag{5.3}$$

where, V_p is the volume of the particle, E_{ac} is the acoustic energy density, ϕ is contrast factor, p_a is acoustic pressure, λ is the wavelength, β_p is compressibility of the particle, β_f is compressibility of the liquid, ρ_p is the density of the particle, and ρ_f is the density of

the fluid. When acoustic contrast factor ϕ is positive, the particles are driven towards the node and this is the case for every material chosen in this study.

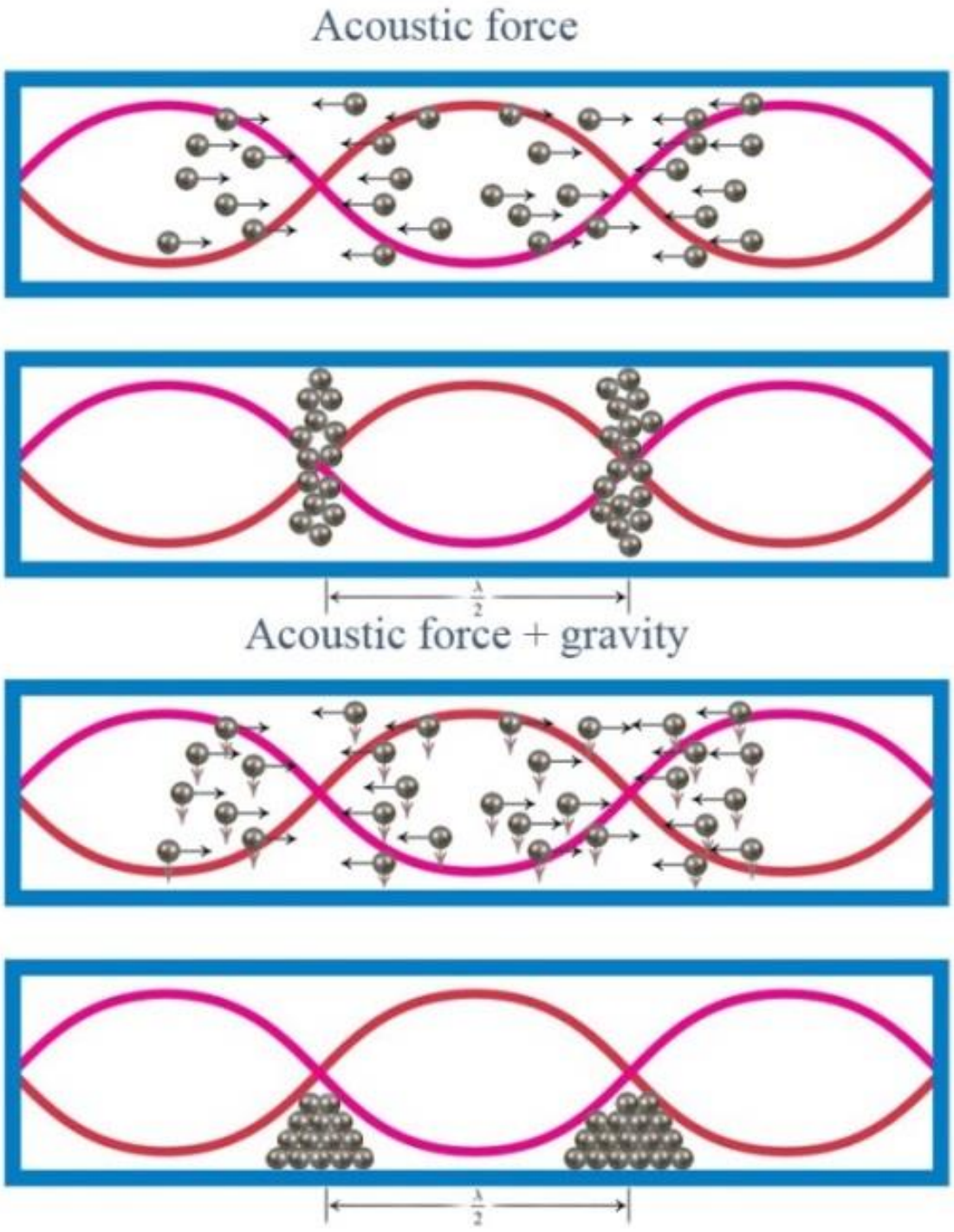

Figure 5-2 Schematic of particle alignment in an acoustic field with only acoustic force and with acoustic force and gravity.

In the designed acoustic tweezer, the particulates are mainly subjected to primary radiation force and gravity. The use of low viscosity resin reduces the undesired drag force which works against the primary radiation force. Fig. 5-2 shows a schematic demonstration of one dimensional (1D) acoustic alignment only with acoustic force and together with gravity. As it is demonstrated, the particles are accumulated at the bottom as a line along the nodal planes of the acoustic field and continuous lines equally spaced by $\lambda/2$ is produced.

5.2.3 Fabrication of Specimens

Magnetite nanoparticles (from Alpha Chemicals) with outer diameter (OD) of 300nm, copper nanoparticles (from US-nano) with OD of 300 nm, and carbon nanofibers (from US-nano) with OD of 200-600 nm and length of 5-50 μm were used as reinforcement and the source of the conductivity. Nanoparticles and nanofibers were added into low viscosity photocurable resin with different weight fractions ranging from 0.0-9.0wt% to produce suspension for the process. Fig. 5-3 shows the diagram of the 3D printing process for the fabrication. First, the prepared suspension was filled in the acoustic tweezer. Then particles were mechanically dispersed inside the container and aligned in the preferred direction by actuating the piezo plates. After the alignment, the necessary parts of the pattern were solidified by light projection from DLP projector. After that, particles were mechanically dispersed and remaining parts of the layer were solidified without any alignment. The same steps were repeated for every layer. Finally, the printed piece was removed from the platform and post-cured. The post curing process was performed 30 mm beneath a UV lamp inside a UV light oven. The fabricated pieces were placed under the lamp and were cured for 60 minutes.

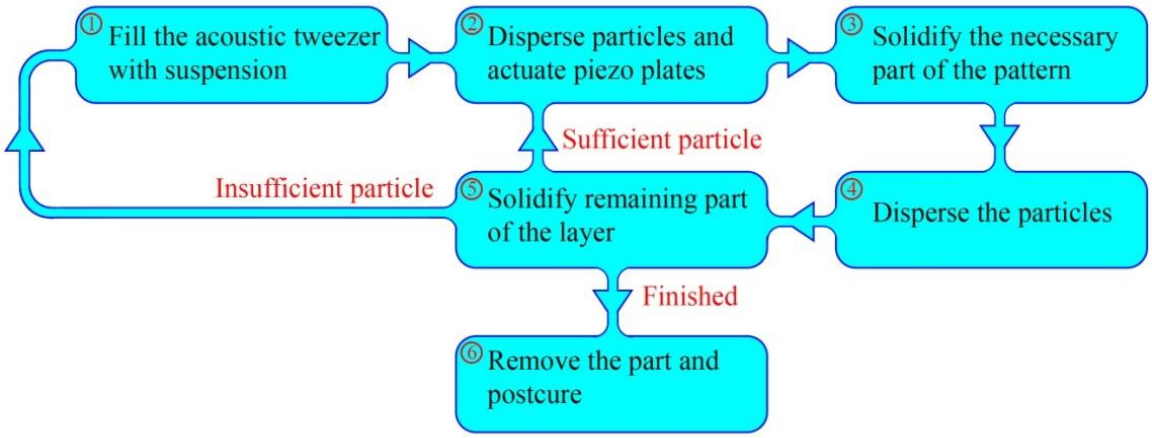

Figure 5-3 Flow diagram of the 3D printing process

5.3 Results

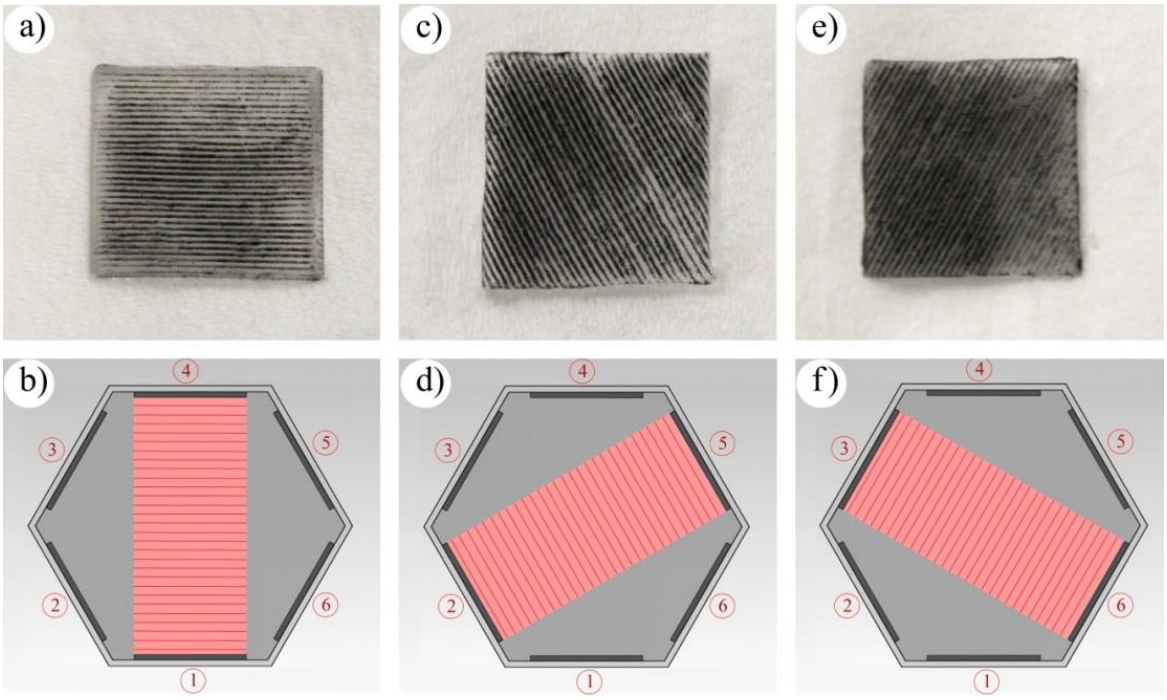

Figure 5-4 Different unidirectional pattern combinations used and their schematic acoustic tweezer setting demonstrations ; (a) horizontal, (b) acoustic tweezer setting for horizontal alignment, (c) 60º, (d) acoustic tweezer setting for 60º alignment, (e) 120º, (f) acoustic tweezer setting for 120º alignment.

At first, the fabrication method was used to produce 1D patterning of continuous lines in one layer samples with dimensions of 10 x 10 x 0.5 mm. The samples were produced with different weight fractions of carbon nanofiber, copper and magnetite nanoparticle reinforcements to measure conductivity of the produced patterns. Three different opposed piezo plate pair options were used for horizontal, 60º, and 120º alignments of line patterns (see Fig. 5-4). Conductivity on x-y plane was provided by those individual patterned lines.

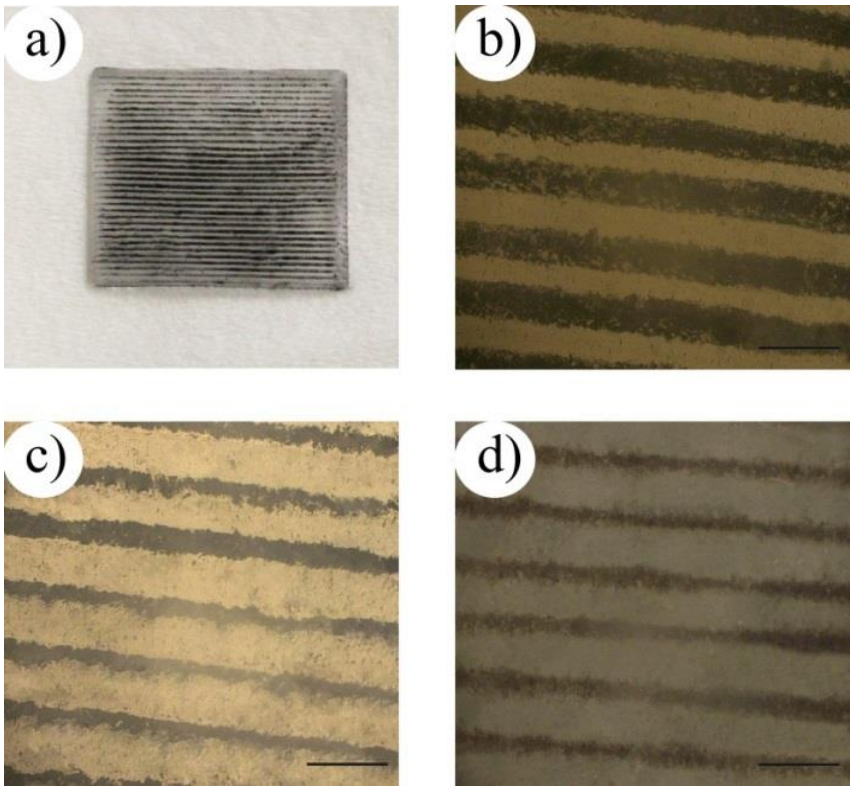

Figure 5-5 Images of patterned unidirectional conductive lines: (a) Unidirectionally patterned magnetite sample with dimensions of 10 x 10 x 0.5 mm; Images of (b) Magnetite, (c) carbon nanofiber, (d) copper reinforcements which aligned into unidirectional lines under microscope (bars: 500 μm). In each sample, lines of the pattern have an average distance of 300 μm at the operating frequency of 2.33 MHz.

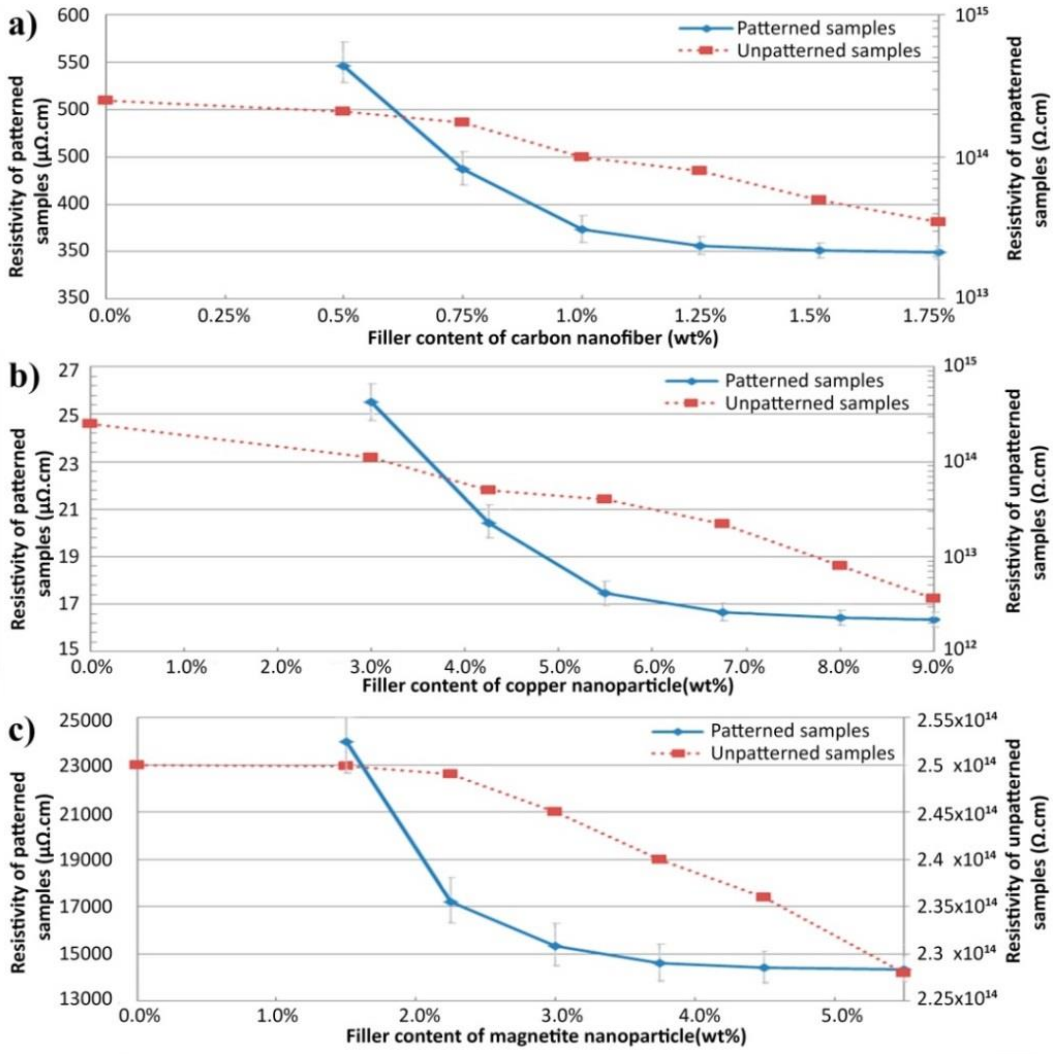

Figure 5-6 Resistivity of patterned and unpatterned samples as a function of nanoparticle weight concentration in the acoustic tweezer; (a) resistivity as a function of carbon nanofiber concentration, (b) resistivity as a function of copper nanoparticle concentration (c) resistivity as a function of magnetite nanoparticle concentration

Acoustic field with 2.33 MHz frequency and ~1400 m/s speed of sound in the photocurable media corresponds with ~600 μm wavelength. Therefore, nodal planes of the field equally spaced by $\lambda/2 \approx 300\mu m$. This value corresponds with average ~300 μm distance between lines of the pattern shown in Fig. 5-5. By acoustic focusing, particles were accumulated at the nodal planes to shape conductive lines. This results with transparency on the other parts of the layer. Samples with conductive line patterns were

used to evaluate the resistivity of patterns based on material and percentages of nanoparticulates. Figure 5-5 shows microscope images of patterned unidirectional conductive lines. While Fig. 5-5a shows the sample with aligned magnetite nanoparticles, Fig. 5-5b, c, and d show the microscope images of unidirectionally patterned reinforced magnetite, carbon nanofiber, and copper nanoparticles, respectively.

The resistivity of carbon fiber changes from 12 μΩ.cm to 104 μΩ.cm based on manufacturing method and temperature, while the resistivity of copper is 1.6 μΩ.cm in its bulk form. Those good electrical properties were used to fabricate embedded conductive wires during SLA 3d printing. The change of electrical resistivity of the photocurable resin after the addition of nanoparticles with and without acoustic focusing was investigated. Results for resistivity of the patterned lines and unpatterned samples are demonstrated in Fig. 5-6. During the fabrication of unpatterned samples, acoustic patterning was not used and particles were not allowed to settle to the bottom before curing. Filler content of the particulates refers to the percentages of reinforcement in the acoustic tweezer before acoustic alignment. Resistivity of the sample without any additive was 2.5×10^{14} Ω.cm and it decreased to 3.6×10^{12} Ω.cm, 3.5×10^{13} Ω.cm, and 2.28×10^{14} Ω.cm with 9wt% copper nanoparticles, 1.75wt% carbon nanofiber, and 5.5wt% magnetite nanoparticles, respectively. Due to very low concentration of particles, the addition of particles has very limited effect on conductivity without acoustic focusing. On the other hand, the resistivity of patterned samples are 13-15 orders of magnitudes lower than the resistivity of unpatterned sample as a result of acoustic focusing. Resistivity of the samples with acoustic patterning decreased to 16.3 μΩ.cm, 349.6 μΩ.cm, and 14340 μΩ.cm with 9wt% copper nanoparticles, 1.75wt% carbon nanofiber,

and 5.5wt% magnetite nanoparticles, respectively. This substantial change was achieved by the accumulation of nanoparticles at nodal planes of acoustic field and later by allowing particles to settle out of the resin with gravity. Similar results were achieved based on fit-to-flow method and inkjet printing with silver nanoparticles [253, 254]. However similar studies with FDM based conductive material fabrication has lower particle concentration to prevent clogging of the nozzle. Low concentration of particles results with higher resistivity values around 1-10 Ω.cm [5, 74].

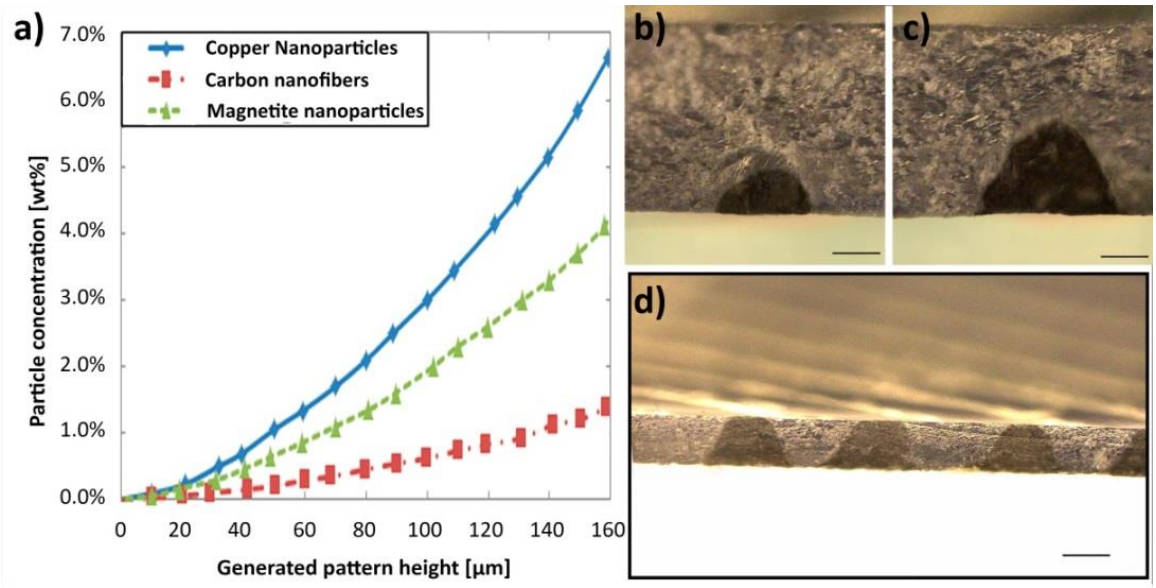

Figure 5-7 Effects of particle weight percentage on pattern height and shape; (a) relation between particle concentration and generated pattern height for different nano particles, (b) cross section of aligned pattern with 50 µm height in 200 µm layer (scale bar: 50 µm), (c) cross section of aligned pattern with 100 µm height in 200 µm layer (scale bar: 50 µm), (d) Cross-section of aligned pattern with 100 µm thickness, pattern is conductive in z direction (scale bar: 100 µm).

While electrical conductivity on x-y plane was obtained by acoustic alignment, electrical conductivity on z direction was obtained by overlapping patterned layers. The height of the pattern depends on the particle concentration. Sufficient particle concentration was used to obtain pattern height same with the layer thickness to overlap

the interlayer microstructures. Fig. 5-7a shows the relation between particle weight concentration in acoustic tweezer and the pattern height for different particle materials. Fig. 5-7b and c show the pattern cross-section with 50 µm and 100 µm height in 200 µm cured layer, with 0.65wt% and 2wt% magnetite nanoparticles. Unfortunately, those patterns cannot conduct electricity towards the next layer. In order to achieve that goal, we reduced the layer thickness to 100 µm and repeat the process with 4wt% copper nanoparticles. The result shown in Fig 5-7d has 100 µm layer thickness.

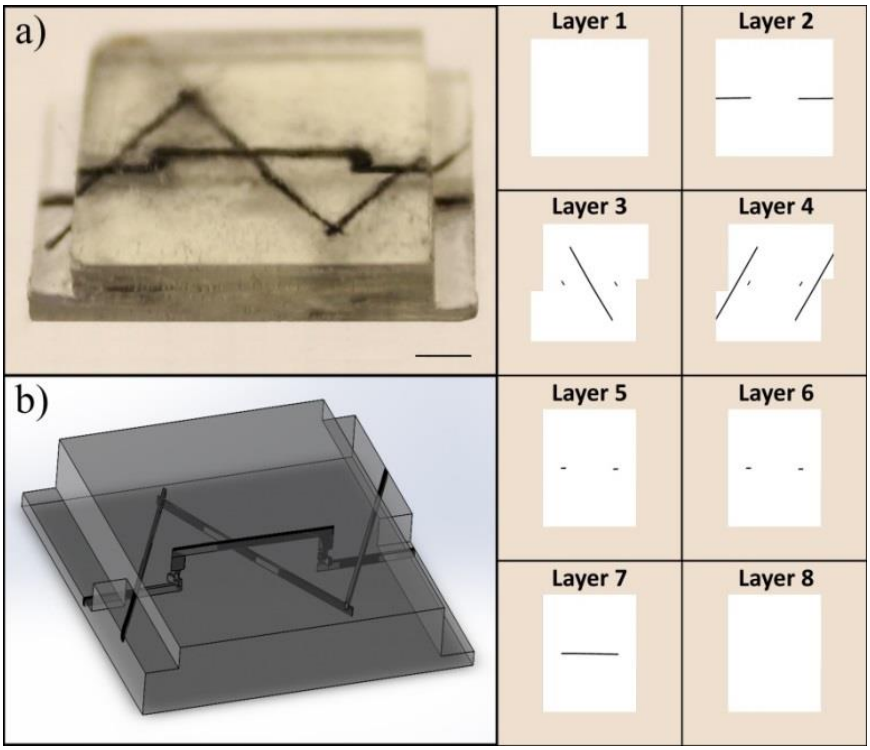

Figure 5-8 Embedded zig-zag stitch pattern. (a) The pattern consists of 8 layers to produce 2 separate conductive wires in complex 3D freeform (scale bar: 1 mm), (b) 3D illustration of the zig-zag stitch pattern. The wires are 100 µm thick in average. Layer 1, 8 are 200 µm and Layer 2-7 are 100 µm thick.

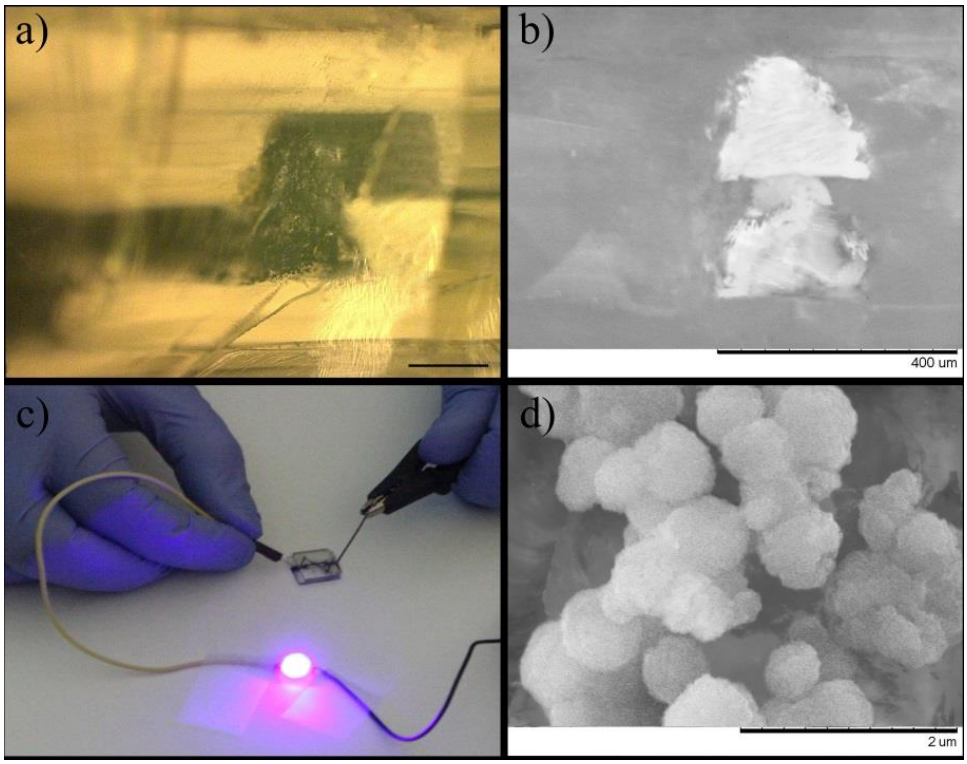

Figure 5-9 Conductivity of embedded zig-zag stitch pattern; (a) cross-sectional cut of printed piece to demonstrate interlayer microstructure contact (scale bar: 100 µm), (b) SEM image of cross-sectional cut of printed piece, (c) demonstration of conductivity in a simple LED circuit, (d) High resolution SEM image of copper nanoparticles in the conductive pattern.

The SLA printing of 3D embedded conductive structure with acoustic alignment is based on stacking layers which consists of aligned and nonaligned parts. By designing the projected images for each layer, contacts between patterns of different layers were provided. An embedded zig-zag stitch wire pattern is demonstrated in Fig. 5-8(a) as an example of a complex 3D structure and 3D illustration of the same structure is shown in Fig. 5-8(b). The zig-zag stitch pattern is consisting of two 100 µm thick conductive wires and it was fabricated with 8 layers which are also shown in Fig. 8. Contact between interlayer patterns, shown through optical and SEM images of a cross-sectional cut in Fig. 5-9(a,b), is found to be the source of the conductivity in z direction. The conductivity

provided by microstructure and interlayer contact is demonstrated with basic LED circuit in Fig. 5-9(c). Acoustic alignment provides high concentration of the particles at the nodal planes of the acoustic field. A high concentration results with direct contact between particles; therefore the conductivity of the pattern is produced. High concentration and direct contact of the nanoparticles are demonstrated in Fig. 5-9(d) with high resolution SEM image.

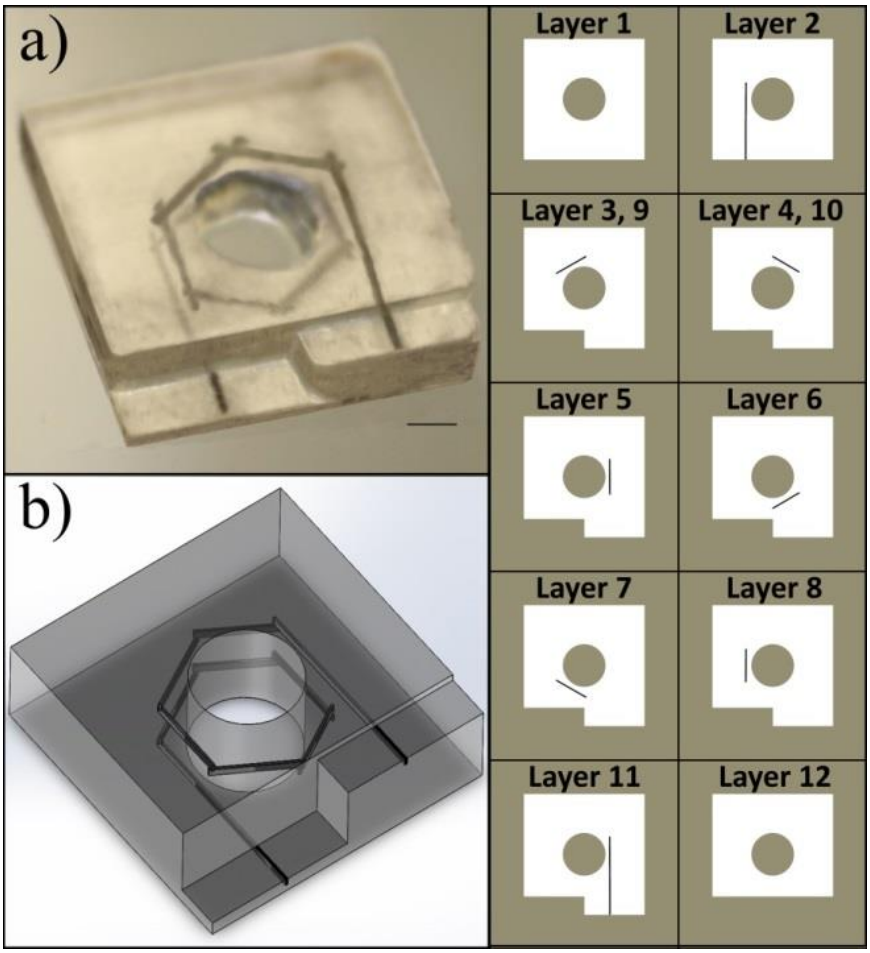

Figure 5-10 Embedded electromagnetic coil pattern. (a) The pattern consists of 12 layers to produce a wire coil surrounding magnetic core cavity (scale bar: 1 mm). (b) 3D illustration of the electromagnet pattern. The wire is 100 μm thick in average. The coil can be produced longer by repeating layers 2-8 until desired length.

The developed method is capable of producing embedded electronic component such as; electromagnetic coil, resistor, or strain sensor. An electromagnetic coil fabricated through the developed method is demonstrated in Fig. 5-10. A 100 μm thick wire is produced with 12 layers and wrapped around a core cavity. The core cavity is left empty for future assembly of a magnetic core. Total height of the piece is around 1.2 mm and it consists of 12 layers with 100 μm thickness. Similar patterns can also serve as a resistor, but the pattern needs to be designed carefully to minimize undesired inductance.

5.4 Conclusions

A new approach to fabricate embedded conductive wires and electronic components based on acoustic alignment of conductive nanoparticles was illustrated. DLP based SLA 3d printer with hexagon shaped acoustic tweezer was used for this approach. First, hexagon shaped acoustic tweezer was demonstrated to effectively align the particles into horizontal, 60º, and 120º patterns. Then, produced anisotropically conductive and transparent patterns were tested for electrical resistivity based on particle materials and filler contents.

Results show that patterned copper particles exhibits less electrical resistivity compared with carbon nanofiber and magnetite particles. Magnetite nanoparticles show ~1000 times higher electrical resistivity compared with copper nanoparticles. Despite the higher electrical resistivity, magnetite nanoparticles can still be important material for patterning magnetic microstructures. The relation between particle concentration and pattern height was also demonstrated due to its importance for the conductivity on z direction. Finally, zig-zag stitch pattern as a complex 3D form and electromagnetic coil pattern as an embedded electronic component were presented as examples of the

developed method. Conductive structures of those examples were produced with 100 μm thickness.

Chapter 6: Conclusion and Future Works

6.1 Conclusion

In this dissertation, additive manufacturing, short fiber alignment, and acoustic manipulation have been reviewed. The main focus of this dissertation was enhancement of material properties, such as tensile strength, flexural strength, and electrical conductivity, during stereolithoraphy. Patterning of electrically conductive particles by acoustic manipulation and shear induced alignment of short fibers by using lateral oscillation mechanism inspired by large amplitude oscillatory shear have been studied.

In an effort to enhance material properties and to provide functionality to the fabricated pieces, lateral oscillation mechanism and acoustic tweezer were employed and explored during stereolithography. Flow charts of the proposed new approaches for stereolithography method were produced to describe the processes. After reviewing additive manufacturing methods, stereolithography was recognized to require new techniques to align short fibers with less material restrictions. Shear induced alignment and acoustic patterning were selected to employ because of their unique advantages to fabricate functional composite materials.

The biggest obstacle for the application of the shear induced alignment to the stereolithography is that technology does not have the means to generate a flow and walls to align the fibers in the liquid resin. Literature review suggests that composite materials

can achieve desired material properties by aligning short fibers during other additive manufacturing methods, such as fuse deposition modeling, inkjet printing, and selective laser sintering. The material properties of these 3d printed composites, such as tensile strength and flexural strength have been described in this dissertation.

The most significant obstacle for acoustic patterning of embedded 3D conductive lines during stereolithography was the determination of the frequency and amplitude of the signal used to generate acoustic standing waves. While standing wave requires specific frequencies based on the cavity dimensions, amplitude of the signal needs be high enough to hold the pattern and low enough to prevent drag by acoustic streaming. Examples from literature show the feasibility of the acoustic alignment for embedded conductive patterns.

To use shear alignment during stereolithography, ceramic and polymer resin suspensions were utilized. For polymer composite fabrication, alumina nanofibers were chosen as reinforcement, while silica ceramic resin suspension was reinforced with nickel coated carbon fiber and ceramic fibers, such as silica and alumina fibers.

Alumina and polymer resin are dissimilar materials and they required surface modification to develop a strong interfacial bond during nanofiber reinforced polymer composite study. 3-(Trimethoxysilyl)propyl methacrylate was used as the surface coupling agent to develop this bond. Varying amount of alumina nanofiber, 1, 2, 3, 4, 5 wt% fractions, were added into resin with and without surface treatment to demonstrate influence of the surface treatment. In ceramic composite study, the mixture of ceramic powders, fiber reinforcement and liquid photocurable resin was used. Ceramic powder for matrix material consisted of silica particles and ceramic binder mix, while nickel

coated carbon fiber, alumina and silica fiber were used as reinforcement with various weight fractions. Polymer resin was burned out with a sintering process; therefore it was not required to apply any surface treatment.

Both ceramic slurry and nanofiber polymer mix, which display shear and strain thinning behavior, are suitable for the shear induced alignment applications. After the fabrication of the composite parts, they were characterized for their key material properties and fiber alignment. The results indicate that the shear alignment method can be deployed for stereolithography with different shear rates, filler contents, and materials.

For acoustic alignment, low viscosity polymeric resin was utilized to reduce acoustic streaming which is not desired for acoustic patterning. Carbon nanofibers, copper, and magnetite nanoparticles were used as additive for resin suspension. 2.33 MHz frequency was selected to achieve 300μm spacing between patterned lines. Patterned lines, where added particulates accumulated with higher concentration, were shown to be conductive with copper nanoparticles and carbon nanofibers.

Different samples were fabricated for characterization of the material properties. A semicircular shaped green sample which was fabricated from ceramic slurry demonstrated the alignment of fibers in the direction of the wall. The sample showed that wall could align the fibers in different direction from the oscillation direction up to 45°. The sintering process caused 15-20% volumetric shrinkage of the samples; however, the shrinkage during the process does not appear to effect the fiber orientation. Additionally, fibers were aligned to the wall direction by oscillation in both ceramic and polymer composite samples, similarly. Both of them contained aligned and well dispersed fibers. The results show improvement of the material strength with alignment in the fiber

direction compared to randomly orientated and neat samples. The alignment of the fibers increased tensile strength in alumina reinforced polymer composites by 28% with 5wt% alumina reinforcement, while the flexural strength of the carbon fiber reinforced ceramic composite increased by 204.8% with 1wt% compared to random orientated samples.

Several one layered and multiple layered samples were fabricated for demonstration of the acoustic alignment approach. One layered samples were used for conductivity analysis. Comparison between electrical resistivity of patterned and unpatterned samples showed the significant effect of the acoustic patterning. Acoustic patterning reduced electrical resistivity from values of 12-14 orders of magnitude to values of 1-4 orders of magnitude. Copper particle pattern which exhibits less electrical resistivity was ~1000 times more conductive than magnetite pattern. One layer patterns were also used for characterizing the influence of particle concentration on pattern dimensions. This data was important for conductivity on the z direction when layers were stacked on each other. By curing partial parts of the pattern and stacking them on each other complex 3d wire structures were fabricated embedded in the polymeric pieces.

SEM and TEM images were used for characterization of the microstructures of the fabricated parts. In conductive patterns, SEM image in Fig. 5-9(d) shows high concentration of copper particles and contact between them. Even though the concentration of the copper resin suspension was 4 wt%, the pattern which is shown in Fig. 5-9(d) has high concentration, 60-65% by volume. The SEM image in Fig. 5-9(b) shows contact between patterns of two stacked layers. The contact is sufficient for electrical conductivity. The SEM images of ceramic composites in Fig. 3-6 displays microstructures of unreinforced, randomly orientated, aligned carbon fiber reinforcement,

and aligned ceramic reinforcement. The shear generated by oscillation aligned the fibers and they are well dispersed. TEM (Fig. 4-8) and SEM (Fig. 4-9) images of fiber reinforced polymer composite also demonstrate alignment and dispersion of the fibers.

The fracture morphology of the carbon fiber reinforced ceramic composite is also demonstrated in Fig. 3-8. The fracture surface did not show any layering or delamination and consisted of both fiber pull-out and fiber failure. The fiber pull-out was more dominant which means interfacial bond can be improved to enhance the strength of the samples further.

6.2 Future Work

Two novel methods of fiber alignment and manipulation technologies for stereolithography were discussed during this dissertation. The first suggested method uses large amplitude oscillatory shear and wall pattern to align the fibers along the wall direction. The second method uses acoustic alignment for nanoparticle patterning. Both approaches provide fine control over the material properties with a wide range of material options and could start a new direction for functional part design and fabrication. Although the methods demonstrate good control over the alignment and patterning, they still have some disadvantages. Methods are constructed by the assembly of layers which have micron level thickness and production speed is very slow. Additionally all layers require special designing, planning, and careful assembly. The fabrication of components with tailored local material properties might allow the methods to be utilized for the production of biomedical products, dental implants, biomimetic structures, or electronic components.

Some possible future works that can be done to extend the work of this dissertation are listed below;

1. Higher fiber content to further improve the material properties

The shear induced alignment of reinforcing fibers presented in this dissertation enables the fabrication of the composite materials with improved mechanical properties as a result of unique control of microstructures. The study shows significant potential for the enhancement of desired mechanical properties. However, to achieve similar results with composite industry standards, the mechanical properties should be increased even further. Therefore, fiber concentration must be increased further while fiber alignment is still achieved with a high degree. Even though, the increase of the fiber concentration would enhance the desired properties of the fabricated piece, the viscosity of the resin will increase and obstruct the layer uniformity and renewal. Some possible solution methods from literature have been discussed in Section 1.7.1.5 and Section 1.7.2.5. The usage of wiper blade or casting mechanisms can be a viable solution to renew viscous resin as a flat and uniform layer. In this study, the weight percentage of ceramic particles was 60%, but the fiber content was limited to 1 wt% for carbon fiber, and 10wt% for ceramic fibers. A higher percentage of fiber in both ceramic and polymer matrix composites would be a worthy study to extend the research in the future.

2. Consolidation and experiment of different materials for alternative functionality

During the studies of shear induced alignment, silica particles and acrylate resin were used as matrix materials. However, there are other useful and functional materials that can be utilized and tested with the system, such as reinforced dental implants,

piezoelectric materials, alumina, zirconia, and barium titanate. Similarly, fiber reinforcement materials can be diversified for different functionality. For example, nickel or nickel coated fibers can be utilized for conductivity or EMI/RFI shielding.

3. Investigation of different fiber microstructures

As it was mention before, addition of fiber reinforcement into the photocurable resin can be utilized to achieve desired functionality and tailored material properties. By organizing and designing the orientation of those fibers, special structures can be fabricated with complex geometries to achieve unique functions and material properties. Investigation of the relation between material properties and complex structure might be an interesting topic to expand the application of the methods. For example, Bouligand structure is a naturally found in many stomatopods and provides increased impact resistance [255]. Replication of that structure might provide desired impact resistance for many composite applications.

4. Optimization of wall and layer design

The most time consuming parts of these two methods are the alignment and microstructuring processes. Additionally, the arbitrary nature of acoustic alignment makes uniform pattern thickness hard to achieve. Inconsistencies in particle concentration sometimes cause conductivity issues between layers. On the other hand, wall pattern of the alignment process requires significant effort and time during design process. Any mistakes in wall pattern design would result with unintended orientation structure. Therefore, model development and optimization for wall pattern and acoustic pattern design are significant future works which need to be done for efficient usage of the methods.

References

[1] B. Berman, 3-D printing: The new industrial revolution, Business horizons 55(2) (2012) 155-162. doi:10.1016/j.bushor.2011.11.003

[2] X. Song, Slurry based stereolithography: a solid freeform fabrication method of ceramics and composites, University of Southern California, Doctoral dissertation, (2016).

[3] S.H. Ahn, M. Montero, D. Odell, S. Roundy, P.K. Wright, Anisotropic material properties of fused deposition modeling ABS, Rapid Prototyping Journal 8(4) (2002) 248-257. doi:10.1108/13552540210441166

[4] F. Rengier, A. Mehndiratta, H. von Tengg-Kobligk, C.M. Zechmann, R. Unterhinninghofen, H.U. Kauczor, F.L. Giesel, 3D printing based on imaging data: review of medical applications, International journal of computer assisted radiology and surgery 5(4) (2010) 335-341. doi:10.1007/s11548-010-0476-x

[5] S.J. Leigh, R.J. Bradley, C.P. Purssell, D.R. Billson, D.A. Hutchins, A simple, low-cost conductive composite material for 3D printing of electronic sensors, PloS one 7(11) (2012) e49365. doi:10.1371/journal.pone.0049365

[6] W. Cui, W. Lu, Y. Zhang, G. Lin, T. Wei, L. Jiang, Gold nanoparticle ink suitable for electric-conductive pattern fabrication using in ink-jet printing technology, Colloids and Surfaces A: Physicochemical and Engineering Aspects 358(1) (2010) 35-41. doi:10.1016/j.colsurfa.2010.01.023

[7] D. Kim, J. Moon, Highly conductive ink jet printed films of nanosilver particles for printable electronics, Electrochemical and Solid-State Letters 8(11) (2005) J30-J33. doi:10.1149/1.2073670

[8] B.G. Compton, J.A. Lewis, 3D-printing of lightweight cellular composites, Advanced Materials 26(34) (2014) 5930-5935. doi:10.1002/adma.201401804

[9] H.L. Tekinalp, V. Kunc, G.M. Velez-Garcia, C.E. Duty, L.J. Love, A.K. Naskar, C.A. Blue, S. Ozcan, Highly oriented carbon fiber–polymer composites via additive manufacturing, Composites Science and Technology 105 (2014) 144-150. doi:10.1016/j.compscitech.2014.10.009

[10] W. Zhong, F. Li, Z. Zhang, L. Song, Z. Li, Short fiber reinforced composites for fused deposition modeling, Materials Science and Engineering: A 301(2) (2001) 125-130. doi:10.1016/S0921-5093(00)01810-4

[11] T. Nakamoto, S. Kojima, Layered Thin Film Micro Parts Reinforced with Aligned Short Fibers in Laser Stereolithography by Applying Magnetic Field, Journal of Advanced Mechanical Design, Systems, and Manufacturing 6(6) (2012) 849-858. doi:10.1299/jamdsm.6.849

[12] T.M. Llewellyn-Jones, B.W. Drinkwater, R.S. Trask, 3D printed components with ultrasonically arranged microscale structure, Smart Materials and Structures 25(2) (2016) 02LT01. doi:10.1088/0964-1726/25/2/02LT01

[13] H. Lee, B. Seong, J. Kim, Y. Jang, D. Byun, Direct Alignment and Patterning of Silver Nanowires by Electrohydrodynamic Jet Printing, Small 10(19) (2014) 3918-3922. doi:10.1002/smll.201400936

[14] F. Fischer, FDM and Polyjet 3D Printing, *Full text paper retrieved from http://web.stratasys.com/rs/objet/images/SSYS-WP-SSYS-InkjetComparison-07-13.pdf* (2013).
[15] A.V. Kumar, A. Dutta, Electrophotographic Layered Manufacturing, ASME Journal of Manufacturing Science and Engineering 126(3) (2004) 571-576. doi:10.1115/1.1765146
[16] A.V. Kumar, A. Dutta, J.E. Fay, Electrophotographic printing of part and binder powders, Rapid Prototyping Journal 10(1) (2004) 7-13. doi:10.1108/13552540410512480
[17] P.J. Lipowicz, H.C. Yeh, Fiber dielectrophoresis, Aerosol science and technology 11(3) (1989) 206-212. doi:10.1080/02786828908959313
[18] D.B. Möller, Acoustically driven particle transport in fluid chambers, Doctoral dissertation, ETH-Zürich, (2013).
[19] C. Witte, Micromanipulation in microfluidics using optoelectronic and acoustic tweezing, Doctoral dissertation, University of Glasgow, (2015).
[20] K. Moradi, Acoustic Manipulation and Alignment of Particles for Applications in Separation, Micro-Templating, and Device Fabrication, Doctoral dissertation, Florida international University (2015).
[21] M.S. Scholz, B. Drinkwater, R. Trask, Ultrasonic assembly of anisotropic short fibre reinforced composites, Ultrasonics 54(4) (2014) 1015-1019. doi:10.1016/j.ultras.2013.12.001
[22] ASTM F2792-12a, Standard Terminology for Additive Manufacturing Technologies, ASTM International, West Conshohocken, PA, (2012).
[23] G. Costabile, M. Fera, F. Fruggiero, A. Lambiase, D. Pham, Cost models of additive manufacturing: A literature review, International Journal of Industrial Engineering Computations 8(2) (2017) 263-283. doi:10.5267/j.ijiec.2016.9.001
[24] R. Noorani, Rapid prototyping: principles and applications, John Wiley & Sons Incorporated (2006).
[25] P.J. Bártolo, Stereolithography: materials, processes and applications, Springer Science & Business Media (2011). doi:10.1007/978-0-387-92904-0_1
[26] C.K. Chua, K.F. Leong, C.S. Lim, Rapid prototyping: principles and applications, World Scientific (2010). doi:10.1142/6665
[27] A.K. Kamrani, E.A. Nasr, Engineering design and rapid prototyping, Springer Science & Business Media (2010). doi:10.1007/978-0-387-95863-7
[28] N. Chalotra, A. Singh, Rapid Growth and Development of 3D Printing, International Journal of Engineering Science 6305 (2016).
[29] R. Liu, Z. Wang, T. Sparks, F. Liou, J. Newkirk, Aerospace applications of laser additive manufacturing 13, Laser Additive Manufacturing: Materials, Design, Technologies, and Applications (2016) 351. doi:10.1016/B978-0-08-100433-3.00013-0
[30] P.S. D'Urso, D.J. Effeney, W.J. Earwaker, T.M. Barker, M.J. Redmond, R.G. Thompson, F.H. Tomlinson, Custom cranioplasty using stereolithography and acrylic, British Journal of Plastic Surgery 53(3) (2000) 200-204. doi:10.1054/bjps.1999.3268
[31] Y. Yap, W. Yeong, Additive manufacture of fashion and jewellery products: a mini review: This paper provides an insight into the future of 3D printing

industries for fashion and jewellery products, Virtual and Physical Prototyping 9(3) (2014) 195-201. doi: 10.1080/17452759.2014.938993
[32] E. Macdonald, R. Salas, D. Espalin, M. Perez, E. Aguilera, D. Muse, R.B. Wicker, 3D printing for the rapid prototyping of structural electronics, IEEE Access 2 (2014) 234-242. doi:10.1109/ACCESS.2014.2311810
[33] D. Bak, Rapid prototyping or rapid production? 3D printing processes move industry towards the latter, Assembly Automation 23(4) (2003) 340-345. doi:10.1108/01445150310501190
[34] W. Shi, R. He, Y. Liu, 3D printing scaffolds with hydrogel materials for biomedical applications, European Journal of BioMedical Research 1(3) (2015) 3-8. doi:10.18088/ejbmr.1.3.2015.pp3-8
[35] R. He, S. Wang, G. Andrews, W. Shi, Y. Liu, Generation of Customizable Micro-wavy Pattern through Grayscale Direct Image Lithography, Scientific reports 6 (2016). doi:10.1038/srep21621
[36] S. Wang, S. Sohrabi, J. Xu, J. Yang, Y. Liu, Geometry design of herringbone structures for cancer cell capture in a microfluidic device, Microfluidics and Nanofluidics 20(11) (2016) 148. doi:10.1007/s10404-016-1813-3
[37] R. He, D. Yunus, C. Uhl, W. Shi, S. Sohrabi, Y. Liu, Fabrication of circular microfluidic channels through grayscale dual-projection lithography, Microfluidics and Nanofluidics 21(1) (2017) 13. doi:10.1007/s10404-017-1851-5
[38] A.A.S. Bhagat, S.S. Kuntaegowdanahalli, I. Papautsky, Inertial microfluidics for continuous particle filtration and extraction, Microfluidics and nanofluidics 7(2) (2009) 217-226. doi:10.1007/s10404-008-0377-2
[39] M.P. Howard, A. Gautam, A.Z. Panagiotopoulos, A. Nikoubashman, Axial dispersion of Brownian colloids in microfluidic channels, Physical Review Fluids 1(4) (2016) 044203. doi:10.1103/PhysRevFluids.1.044203
[40] S. Sohrabi, D.E. Yunus, J. Xu, J. Yang, Y. Liu, Characterization of nanoparticle binding dynamics in microcirculation using an adhesion probability function, Microvascular Research 108 (2016) 41-47. doi:10.1016/j.mvr.2016.07.005
[41] S. Sohrabi, S. Wang, J. Tan, J. Xu, J. Yang, Y. Liu, Nanoparticle transport and delivery in a heterogeneous pulmonary vasculature, Journal of Biomechanics 50 (2017) 240-247. doi:10.1016/j.jbiomech.2016.11.023
[42] S. Sohrabi, J. Zheng, E.A. Finol, Y. Liu, Numerical simulation of particle transport and deposition in the pulmonary vasculature, Journal of biomechanical engineering 136(12) (2014) 121010. doi:10.1115/1.4028800
[43] A.M. Phatak, S. Pande, Optimum part orientation in rapid prototyping using genetic algorithm, Journal of manufacturing systems 31(4) (2012) 395-402. doi:10.1016/j.jmsy.2012.07.001
[44] G. Jin, W. Li, C. Tsai, L. Wang, Adaptive tool-path generation of rapid prototyping for complex product models, Journal of manufacturing systems 30(3) (2011) 154-164. doi:10.1016/j.jmsy.2011.05.007
[45] W.C. Lee, C.C. Wei, S.-C. Chung, Development of a hybrid rapid prototyping system using low-cost fused deposition modeling and five-axis machining, Journal of Materials Processing Technology 214(11) (2014) 2366-2374. doi:10.1016/j.jmatprotec.2014.05.004

[46] C.W. Hull, Apparatus for production of three-dimensional objects by stereolithography, US Patent 4575330, (1986).
[47] E.V. Fudim, Method and apparatus for production of three-dimensional objects by photosolidification, US Patent 4801477, (1988).
[48] W.E. Masters, Computer automated manufacturing process and system, US Patent 4665492, (1987).
[49] P.F. Jacobs, Fundamentals of stereolithography, Proceedings of the solid freeform fabrication symposium, (1992), pp. 196-211.
[50] C. Zhou, Y. Chen, Z. Yang, B. Khoshnevis, Digital material fabrication using mask-image-projection-based stereolithography, Rapid Prototyping Journal 19(3) (2013) 153-165. doi:10.1108/13552541311312148
[51] X. Song, Y. Chen, T.W. Lee, S. Wu, L. Cheng, Ceramic fabrication using mask-image-projection-based stereolithography integrated with tape-casting, Journal of Manufacturing Processes 20 (2015) 456-464. doi:10.1016/j.jmapro.2015.06.022
[52] M.M. Emami, F. Barazandeh, F. Yaghmaie, Scanning-projection based stereolithography: Method and structure, Sensors and Actuators A: Physical 218 (2014) 116-124. doi:10.1016/j.sna.2014.08.002
[53] Y. Liu, R. He, W. Shi, All Dimension Fabrication Apparatus and Methods, US Patent 20160303795, (2016).
[54] C. Decker, Photoinitiated crosslinking polymerisation, Progress in Polymer Science 21(4) (1996) 593-650. doi:10.1016/0079-6700(95)00027-5
[55] C. Decker, T.N.T. Viet, D. Decker, E. Weber-Koehl, UV-radiation curing of acrylate/epoxide systems, Polymer 42(13) (2001) 5531-5541. doi:10.1016/S0032-3861(01)00065-9
[56] P. Visakh, S. Thomas, A.K. Chandra, A.P. Mathew, Advances in elastomers I: blends and interpenetrating networks, Springer Science & Business Media (2013). doi:10.1007/978-3-642-20925-3
[57] A.K. O'Brien, N.B. Cramer, C.N. Bowman, Oxygen inhibition in thiol–acrylate photopolymerizations, Journal of Polymer Science Part A: Polymer Chemistry 44(6) (2006) 2007-2014. doi:10.1002/pola.21304
[58] J. Chen, M.D. Soucek, Ultraviolet curing kinetics of cycloaliphatic epoxide with real-time fourier transform infrared spectroscopy, Journal of applied polymer science 90(9) (2003) 2485-2499. doi:10.1002/app.12898
[59] C.E. Hoyle, Calorimetric analysis of photopolymerization, Radiation Curing, Springer (1992), pp. 57-133. doi:10.1007/978-1-4899-0712-7_3
[60] J. Fouassier, An introduction to the basic principles in UV-curing, Radiation curing in polymer science and technology 1 (1993) 49.
[61] P.F. Jacobs, Rapid prototyping & manufacturing: fundamentals of stereolithography, Society of Manufacturing Engineers (1992).
[62] D.W. Rosen, Stereolithography and rapid prototyping, BioNanoFluidic MEMS, Springer2008, pp. 175-196. doi:10.1007/978-0-387-46283-7_7
[63] A.S. Limaye, Multi-objective process planning method for Mask Projection Stereolithography, Doctoral dissertation, Georgia Institute of Technology, (2007).
[64] D. Lee, T. Miyoshi, Y. Takaya, T. Ha, 3D microfabrication of photosensitive resin reinforced with ceramic nanoparticles using LCD microstereolithography, J. Laser Micro/Nanoeng. 1 (2006) 142-148. doi:10.2961/jlmn.2006.02.0011

[65] C. Zhou, Y. Chen, Additive manufacturing based on optimized mask video projection for improved accuracy and resolution, Journal of Manufacturing Processes 14(2) (2012) 107-118. doi:10.1016/j.jmapro.2011.10.002
[66] M. Yakout, M. Elbestawi, Additive Manufacturing of Composite Materials: An Overview. 6th International Conference on Virtual Machining Process Technology (2017).
[67] B. Xu, S. Yin, Y. Wang, H. Li, B. Zhang, R.O. Ritchie, Long-fiber reinforced thermoplastic composite lattice structures: Fabrication and compressive properties, Composites Part A: Applied Science and Manufacturing 97 (2017) 41-50. doi:10.1016/j.compositesa.2017.03.002
[68] A. Kamyshny, S. Magdassi, Metallic Nanoinks for Inkjet Printing of Conductive 2D and 3D Structures, Nanomaterials for 2D and 3D Printing, Wiley-VCH (2017). doi:10.1002/9783527685790.ch7
[69] Y. Aw, C. Yeoh, M. Idris, H. Amali, S. Aqzna, P. Teh, A study of tensile and thermal properties of 3D printed conductive ABS–ZnO composite, AIP Conference Proceedings, AIP Publishing, 2017, p. 020008. doi:10.1063/1.4981830
[70] S.Y. Chung, D. Stephan, M.A. Elrahman, T.-S. Han, Effects of anisotropic voids on thermal properties of insulating media investigated using 3D printed samples, Construction and Building Materials 111 (2016) 529-542. doi:10.1016/j.conbuildmat.2016.02.165
[71] R. Matsuzaki, M. Ueda, M. Namiki, T.-K. Jeong, H. Asahara, K. Horiguchi, T. Nakamura, A. Todoroki, Y. Hirano, Three-dimensional printing of continuous-fiber composites by in-nozzle impregnation, Scientific reports 6 (2016). doi:10.1038/srep23058
[72] S. Kenzari, D. Bonina, J. Dubois, V. Fournée, Quasicrystal–polymer composites for selective laser sintering technology, Materials & Design 35 (2012) 691-695. doi:10.1016/j.matdes.2011.10.032
[73] D. Klosterman, R. Chartoff, M. Agarwala, I. Fiscus, J. Murphy, S. Cullen, M. Yeazell, Direct Fabrication of Polymer Composite Structures with Cuwed LOM, Proc. Solid Freeform Fabrication Symposium Proceedings, University of Texas at Austin (1999) 401-409.
[74] G. Postiglione, G. Natale, G. Griffini, M. Levi, S. Turri, Conductive 3D microstructures by direct 3D printing of polymer/carbon nanotube nanocomposites via liquid deposition modeling, Composites Part A: Applied Science and Manufacturing 76 (2015) 110-114. doi:10.1016/j.compositesa.2015.05.014
[75] G. Zak, A. Chan, C. Park, B. Benhabib, Viscosity analysis of photopolymer and glass-fibre composites for rapid layered manufacturing, Rapid Prototyping Journal 2(3) (1996) 16-23. doi:10.1108/13552549610129773
[76] S. Kumar, M. Hofmann, B. Steinmann, E.J. Foster, C. Weder, Reinforcement of stereolithographic resins for rapid prototyping with cellulose nanocrystals, ACS applied materials & interfaces 4(10) (2012) 5399-5407. doi:10.1021/am301321v
[77] M. Shofner, K. Lozano, F. Rodríguez-Macías, E. Barrera, Nanofiber-reinforced polymers prepared by fused deposition modeling, Journal of applied polymer science 89(11) (2003) 3081-3090. doi:10.1002/app.12496

[78] H. Giberti, M. Strano, M. Annoni, An innovative machine for fused deposition modeling of metals and advanced ceramics, MATEC Web of Conferences, EDP Sciences, New York, USA, (2016). doi:10.1051/matecconf/20164303003
[79] Y. de Hazan, M. Thänert, M. Trunec, J. Misak, Robotic deposition of 3d nanocomposite and ceramic fiber architectures via UV curable colloidal inks, Journal of the European Ceramic Society 32(6) (2012) 1187-1198. doi:10.1016/j.jeurceramsoc.2011.12.007
[80] L.L. Lebel, B. Aissa, M.A.E. Khakani, D. Therriault, Ultraviolet-Assisted Direct-Write Fabrication of Carbon Nanotube/Polymer Nanocomposite Microcoils, Advanced Materials 22(5) (2010) 592-596. doi:10.1002/adma.200902192
[81] A.S. Gladman, E.A. Matsumoto, R.G. Nuzzo, L. Mahadevan, J.A. Lewis, Biomimetic 4D printing, Nature materials (2016). doi:10.1038/nmat4544
[82] T. Serra, J.A. Planell, M. Navarro, High-resolution PLA-based composite scaffolds via 3-D printing technology, Acta biomaterialia 9(3) (2013) 5521-5530. doi:10.1016/j.actbio.2012.10.041
[83] J.S. Lee, J.M. Hong, J.W. Jung, J.H. Shim, J.H. Oh, D.W. Cho, 3D printing of composite tissue with complex shape applied to ear regeneration, Biofabrication 6(2) (2014) 024103. doi:10.1088/1758-5082/6/2/024103
[84] H. Liu, J. Mo, Study on nanosilica reinforced stereolithography resin, Journal of Reinforced Plastics and Composites 29(6) (2010) 909-920. doi:10.1177/0731684409102838
[85] Z. Lu, F. Lu, J. Cao, D. Li, Manufacturing properties of turbine blades of carbon fiber-reinforced SiC composite based on stereolithography, Materials and Manufacturing Processes 29(2) (2014) 201-209. doi:10.1007/s00170-013-5049-z
[86] J. Lee, R. Prud'homme, I. Aksay, Processing of Organic/Inorganic Composites by Stereolithography, MRS Proceedings, Cambridge Univ Press, (2000), p. 165. doi:10.1557/PROC-625-165
[87] W.R. McCall, K. Kim, C. Heath, G. La Pierre, D.J. Sirbuly, Piezoelectric Nanoparticle–Polymer Composite Foams, ACS applied materials & interfaces 6(22) (2014) 19504-19509. doi:10.1021/am506415y
[88] Z. Weng, Y. Zhou, W. Lin, T. Senthil, L. Wu, Structure-property relationship of nano enhanced stereolithography resin for desktop SLA 3D printer, Composites Part A: Applied Science and Manufacturing 88 (2016) 234-242. doi:10.1016/j.compositesa.2016.05.035
[89] T. Chartier, C. Hinczewski, S. Corbel, UV curable systems for tape casting, Journal of the European Ceramic Society 19(1) (1999) 67-74. doi:10.1016/S0955-2219(98)00177-0
[90] A. Goswami, K. Ankit, N. Balashanmugam, A.M. Umarji, G. Madras, Optimization of rheological properties of photopolymerizable alumina suspensions for ceramic microstereolithography, Ceramics International 40(2) (2014) 3655-3665. doi:10.1016/j.ceramint.2013.09.059
[91] A. Badev, Y. Abouliatim, T. Chartier, L. Lecamp, P. Lebaudy, C. Chaput, C. Delage, Photopolymerization kinetics of a polyether acrylate in the presence of ceramic fillers used in stereolithography, Journal of Photochemistry and Photobiology A: Chemistry 222(1) (2011) 117-122. doi:10.1016/j.jphotochem.2011.05.010

[92] S.H. Chiu, I. Ivan, C.L. Wu, K.T. Chen, S.T. Wicaksono, Mechanical properties of urethane diacrylate/bamboo powder composite fabricated by rapid prototyping system, Rapid Prototyping Journal 22(4) (2016) 676-683. doi:10.1108/RPJ-08-2014-0097
[93] J. Wilkes, Y.-C. Hagedorn, W. Meiners, K. Wissenbach, Additive manufacturing of ZrO2-Al2O3 ceramic components by selective laser melting, Rapid Prototyping Journal 19(1) (2013) 51-57. doi:10.1108/13552541311292736
[94] M. Jafari, W. Han, F. Mohammadi, A. Safari, S. Danforth, N. Langrana, A novel system for fused deposition of advanced multiple ceramics, Rapid Prototyping Journal 6(3) (2000) 161-175. doi:10.1108/13552540010337047
[95] M. Mott, J.R. Evans, Solid freeforming of silicon carbide by inkjet printing using a polymeric precursor, Journal of the American Ceramic Society 84(2) (2001) 307-13. doi:10.1111/j.1151-2916.2001.tb00655.x
[96] C.M. Gomes, C.R. Rambo, A.P.N. De Oliveira, D. Hotza, D. Gouveˆa, N. Travitzky, P. Greil, Colloidal processing of glass–ceramics for laminated object manufacturing, Journal of the American Ceramic Society 92(6) (2009) 1186-1191. doi:10.1111/j.1551-2916.2009.03035.x
[97] W. Zhou, D. Li, H. Wang, A novel aqueous ceramic suspension for ceramic stereolithography, Rapid Prototyping Journal 16(1) (2010) 29-35. doi:10.1108/13552541011011686
[98] T. McNulty, F. Mohammadi, A. Bandyopadhyay, D. Shanefield, S. Danforth, A. Safari, Development of a binder formulation for fused deposition of ceramics, Rapid Prototyping Journal 4(4) (1998) 144-150. doi:10.1108/13552549810239012
[99] U. Scheithauer, A. Bergner, E. Schwarzer, H.-J. Richter, T. Moritz, Studies on thermoplastic 3D printing of steel–zirconia composites, Journal of Materials Research 29(17) (2014) 1931-1940. doi:10.1557/jmr.2014.209
[100] T. Huang, M.S. Mason, X. Zhao, G.E. Hilmas, M.C. Leu, Aqueous-based freeze-form extrusion fabrication of alumina components, Rapid Prototyping Journal 15(2) (2009) 88-95. doi:10.1108/13552540910943388
[101] J. Ebert, E. Özkol, A. Zeichner, K. Uibel, Ö. Weiss, U. Koops, R. Telle, H. Fischer, Direct inkjet printing of dental prostheses made of zirconia, Journal of dental research 88(7) (2009) 673-676. doi:10.1177/0022034509339988
[102] J. Suwanprateeb, R. Sanngam, W. Suvannapruk, T. Panyathanmaporn, Mechanical and in vitro performance of apatite–wollastonite glass ceramic reinforced hydroxyapatite composite fabricated by 3D-printing, Journal of Materials Science: Materials in Medicine 20(6) (2009) 1281. doi:10.1007/s10856-009-3697-1
[103] W. Bian, D. Li, Q. Lian, X. Li, W. Zhang, K. Wang, Z. Jin, Fabrication of a bio-inspired beta-Tricalcium phosphate/collagen scaffold based on ceramic stereolithography and gel casting for osteochondral tissue engineering, Rapid Prototyping Journal 18(1) (2012) 68-80. doi:10.1108/13552541211193511
[104] B. Thavornyutikarn, P. Tesavibul, K. Sitthiseripratip, N. Chatarapanich, B. Feltis, P.F. Wright, T.W. Turney, Porous 45S5 Bioglass®-based scaffolds using stereolithography: Effect of partial pre-sintering on structural and mechanical properties of scaffolds, Materials Science and Engineering: C 75 (2017) 1281-1288. doi:10.1016/j.msec.2017.03.001

[105] M. Schwentenwein, J. Homa, Additive manufacturing of dense alumina ceramics, International Journal of Applied Ceramic Technology 12(1) (2015) 1-7. doi:10.1111/ijac.12319
[106] H.H. Tang, M.L. Chiu, H.C. Yen, Slurry-based selective laser sintering of polymer-coated ceramic powders to fabricate high strength alumina parts, Journal of the European Ceramic Society 31(8) (2011) 1383-1388. doi:10.1016/j.jeurceramsoc.2011.02.020
[107] H.C. Yen, Experimental studying on development of slurry-layer casting system for additive manufacturing of ceramics, The International Journal of Advanced Manufacturing Technology 77(5-8) (2015) 915-925. doi:10.1007/s00170-014-6534-8
[108] Z.C. Eckel, C. Zhou, J.H. Martin, A.J. Jacobsen, W.B. Carter, T.A. Schaedler, Additive manufacturing of polymer-derived ceramics, Science 351(6268) (2016) 58-62. doi:10.1126/science.aad2688
[109] E. Zanchetta, M. Cattaldo, G. Franchin, M. Schwentenwein, J. Homa, G. Brusatin, P. Colombo, Stereolithography of SiOC ceramic microcomponents, Advanced Materials 28(2) (2016) 370-376. doi: 10.1002/adma.201503470
[110] L. Lü, J. Fuh, Y.-S. Wong, Laser-induced materials and processes for rapid prototyping, Springer (2013). doi:10.1007/978-1-4615-1469-5
[111] G. Zak, M. Haberer, C. Park, B. Benhabib, Mechanical properties of short-fibre layered composites: prediction and experiment, Rapid Prototyping Journal 6(2) (2000) 107-118. doi:10.1108/13552540010323583
[112] R.M. Taib, Cellulose fiber reinforced thermoplastic composites: processing and product charateristics, Master Thesis, Virginia Polytechnic Institute and State University (1998).
[113] D. Hull, T. Clyne, An introduction to composite materials, Cambridge university press (1996). doi:10.1017/CBO9781139170130
[114] S.Y. Fu, B. Lauke, E. Mäder, C.Y. Yue, X. Hu, Tensile properties of short-glass-fiber-and short-carbon-fiber-reinforced polypropylene composites, Composites Part A: Applied Science and Manufacturing 31(10) (2000) 1117-1125. doi:10.1016/S1359-835X(00)00068-3
[115] L. Harper, T. Turner, J. Martin, N. Warrior, Fiber alignment in directed carbon fiber preforms—a feasibility study, Journal of Composite Materials 43(1) (2009) 57-74. doi:10.1177/0021998308098151
[116] T. Flemming, G. Kress, M. Flemming, A new aligned short-carbon-fiber-reinforced thermoplastic prepreg, Advanced Composite Materials 5(2) (1996) 151-159. doi:10.1163/156855196X00068
[117] S.Y. Fu, B. Lauke, Effects of fiber length and fiber orientation distributions on the tensile strength of short-fiber-reinforced polymers, Composites Science and Technology 56(10) (1996) 1179-1190. doi:10.1016/S0266-3538(96)00072-3
[118] J. Thomason, The influence of fibre length and concentration on the properties of glass fibre reinforced polypropylene: 5. Injection moulded long and short fibre PP, Composites Part A: Applied Science and Manufacturing 33(12) (2002) 1641-1652. doi:10.1016/S1359-835X(02)00179-3

[119] N. Choi, K. Takahashi, Stress fields on and beneath the surface of short-fiber-reinforced composites and their failure mechanisms, Composites science and technology 43(3) (1992) 237-244. doi:10.1016/0266-3538(92)90094-J
[120] T. Papthanasiou, D.C. Guell, Flow-induced alignment in composite materials, Elsevier (1997).
[121] C. Bowen, A. Dent, R. Stevens, M. Cain, M. Stewart, Determination of critical and minimum volume fraction for composite sensors and actuators, 4M2005 Conference on Multi-Material Micro Manufacture, (2005).
[122] J. Epaarachchi, H. Ku, K. Gohel, A simplified empirical model for prediction of mechanical properties of random short fiber/vinylester composites, Journal of composite materials 44(6) (2010) 779-788. doi:10.1177/0021998309346383
[123] T.F. MacLaughlin, R. Barker, Effect of modulus ratio on stress near a discontinuous fiber, Experimental Mechanics 12(4) (1972) 178-183. doi:10.1007/BF02330270
[124] B. Mouhmid, A. Imad, N. Benseddiq, S. Benmedakhène, A. Maazouz, A study of the mechanical behaviour of a glass fibre reinforced polyamide 6, 6: Experimental investigation, Polymer Testing 25(4) (2006) 544-552. doi:10.1016/j.polymertesting.2006.03.008
[125] C. Price, P. Hine, B. Whiteside, A. Cunha, I. Ward, Modelling the elastic and thermoelastic properties of short fibre composites with anisotropic phases, Composites science and technology 66(1) (2006) 69-79. doi:10.1016/j.compscitech.2005.05.024
[126] P. Hine, R. Duckett, N. Davidson, A. Clarke, Modelling of the elastic properties of fibre reinforced composites. I: Orientation measurement, Composites Science and Technology 47(1) (1993) 65-73. doi:10.1016/0266-3538(93)90097-Z
[127] S. Dul, L. Fambri, A. Pegoretti, Fused deposition modelling with ABS–graphene nanocomposites, Composites Part A: Applied Science and Manufacturing 85 (2016) 181-191. doi:10.1016/j.compositesa.2016.03.013
[128] T. Itoh, H. Hirai, R.I. Isomura, Aluminum alloy matrix composites with discontinuous fibers oriented uniaxially by electrostatic method, Japan Institute of Light Metals, Journal 38 (1988) 620-625. doi:10.2464/jilm.38.620
[129] L. Kacir, M. Narkis, O. Ishai, Oriented short glass-fiber composites. I. Preparation and statistical analysis of aligned fiber mats, Polymer Engineering & Science 15(7) (1975) 525-531. doi:10.1002/pen.760150708
[130] N. Jameson, Production of aligned short-fibre composites, Master Thesis, University of Birmingham, 2014.
[131] D.C. Guell, A.L. Graham, Improved mechanical properties in hydrodynamically aligned, short-fiber composite materials, Journal of composite materials 30(1) (1996) 2-12.
[132] S. Fara, A. Pavan, Fibre orientation effects on the fracture of short fibre polymer composites: on the existence of a critical fibre orientation on varying internal material variables, Journal of materials science 39(11) (2004) 3619-3628. doi:10.1023/B:JMSC.0000030714.13161.f6
[133] P. Calvert, T.L. Lin, H. Martin, Extrusion freeform fabrication of chopped-fibre reinforced composites, High Performance Polymers 9(4) (1997) 449-456.

[134] H. Cox, The elasticity and strength of paper and other fibrous materials, British journal of applied physics 3(3) (1952) 72.
[135] H. Fukuda, K. Kawata, On Young's modulus of short fibre composites, Fibre science and technology 7(3) (1974) 207-222. doi:10.1016/0015-0568(74)90018-9
[136] Y. Sanomura, K. Hayakawa, M. Mizuno, M. Kawamura, Effect of process conditions on Young's modulus and strength of extrudate in short-fiber-reinforced polypropylene, Seikei-Kakou 18(4) (2006) 293-299. doi:10.1002/pc.20300
[137] A. Rothen-Weinhold, K. Besseghir, E. Vuaridel, E. Sublet, N. Oudry, F. Kubel, R. Gurny, Injection-molding versus extrusion as manufacturing technique for the preparation of biodegradable implants, European journal of pharmaceutics and biopharmaceutics 48(2) (1999) 113-121. doi:10.1016/S0939-6411(99)00034-X
[138] P.A. Santos, M.A. Spinacé, K.K. Fermoselli, M.A. De Paoli, Polyamide-6/vegetal fiber composite prepared by extrusion and injection molding, Composites Part A: Applied Science and Manufacturing 38(12) (2007) 2404-2411. doi:10.1016/j.compositesa.2007.08.011
[139] W.M. Chirdon, W.J. O'Brien, R.E. Robertson, Fraunhofer diffraction of short-fiber-reinforced composites aligned by an electric field, Dental Materials 22(2) (2006) 107-111. doi:10.1016/j.dental.2005.04.006
[140] M. Sakar, S. Balakumar, P. Saravanan, S.N. Jaisankar, Electric field induced formation of one-dimensional bismuth ferrite (BiFeO 3) nanostructures in electrospinning process, Materials & Design 94 (2016) 487-495. doi:10.1016/j.matdes.2016.01.029
[141] Y. Liu, J.H. Chung, W.K. Liu, R.S. Ruoff, Dielectrophoretic assembly of nanowires, The Journal of Physical Chemistry B 110(29) (2006) 14098-14106. doi:10.1021/jp061367e
[142] J. Ciambella, D.C. Stanier, S.S. Rahatekar, Magnetic alignment of short carbon fibres in curing composites, Composites Part B: Engineering 109 (2017) 129-137. doi:10.1016/j.compositesb.2016.10.038
[143] R.M. Erb, R. Libanori, N. Rothfuchs, A.R. Studart, Composites reinforced in three dimensions by using low magnetic fields, Science 335(6065) (2012) 199-204. doi:10.1126/science.1210822
[144] S. Takeyama, S. Nakamura, K. Uchida, Dynamical orientation of carbon nanotubes by pulsed magnetic fields, Journal of Physics: Conference Series, IOP Publishing, 2006, p. 446. doi:10.1088/1742-6596/51/1/102
[145] S. Yamashita, H. Hatta, T. Sugano, K. Murayama, Fiber orientation control of short fiber composites: experiment, Journal of composite materials 23(1) (1989) 32-41. doi:10.1177/002199838902300103
[146] S. Sohrabi, Y. Liu, A Cellular Model of Shear-Induced Hemolysis, Artificial organs (2016). doi:10.1111/aor.12832
[147] G.B. Jeffery, The motion of ellipsoidal particles immersed in a viscous fluid, Proceedings of the Royal Society of London A: Mathematical, Physical and Engineering Sciences, The Royal Society, 1922, pp. 161-179. doi:10.1098/rspa.1922.0078
[148] F. Folgar, C.L. Tucker III, Orientation behavior of fibers in concentrated suspensions, Journal of reinforced plastics and composites 3(2) (1984) 98-119. doi:10.1177/073168448400300201

[149] J.H. Phelps, C.L. Tucker, An anisotropic rotary diffusion model for fiber orientation in short-and long-fiber thermoplastics, Journal of Non-Newtonian Fluid Mechanics 156(3) (2009) 165-176. doi:10.1016/j.jnnfm.2008.08.002
[150] J. Wang, J.F. O'Gara, C.L. Tucker III, An objective model for slow orientation kinetics in concentrated fiber suspensions: Theory and rheological evidence, Journal of Rheology 52(5) (2008) 1179-1200. doi:10.1122/1.2946437
[151] J. Férec, G. Ausias, M. Heuzey, P. Carreau, Modeling fiber interactions in semiconcentrated fiber suspensions, Journal of Rheology 53(1) (2009) 49-72. doi:10.1122/1.3000732
[152] U. Strautins, A. Latz, Flow-driven orientation dynamics of semiflexible fiber systems,Rheologica Acta 46(8) (2007) 1057-1064 doi:10.1007/s00397-007-0194-7
[153] M. Rajabian, C. Dubois, M. Grmela, Suspensions of semiflexible fibers in polymeric fluids: rheology and thermodynamics, Rheologica acta 44(5) (2005) 521-535. doi:10.1007/s00397-005-0434-7
[154] S. Le Corre, D. Caillerie, L. Orgéas, D. Favier, Behavior of a net of fibers linked by viscous interactions: theory and mechanical properties, Journal of the Mechanics and Physics of Solids 52(2) (2004) 395-421. doi:10.1016/S0022-5096(03)00090-5
[155] W. Tang, S.G. Advani, Dynamic simulation of long flexible fibers in shear flow, CMES 8(2) (2005) 165-176. doi:10.1063/1.468746
[156] E. Hinch, The distortion of a flexible inextensible thread in a shearing flow, Journal of Fluid Mechanics 74(2) (1976) 317-333. doi:10.1017/S002211207600181X
[157] G. Wang, W. Yu, C. Zhou, Optimization of the rod chain model to simulate the motions of a long flexible fiber in simple shear flows, European Journal of Mechanics-B/Fluids 25(3) (2006) 337-347. doi:10.1016/j.euromechflu.2005.09.004
[158] M.J. Cieslinski, Using a Sliding Plate Rheometer to Obtain Material Parameters for Simulating Long Fiber Orientation in Injection Molded Composites, Doctoral dissertation, Virginia Polytechnic Institute and State University (2015).
[159] S.M. Dinh, R.C. Armstrong, A rheological equation of state for semiconcentrated fiber suspensions, Journal of Rheology 28(3) (1984) 207-227. doi:10.1122/1.549748
[160] M. Keshtkar, M.-C. Heuzey, P. Carreau, M. Rajabian, C. Dubois, Rheological properties and microstructural evolution of semi-flexible fiber suspensions under shear flow, Journal of Rheology 54(2) (2010) 197-222. doi:10.1122/1.3301245
[161] H. Laun, Orientation effects and rheology of short glass fiber-reinforced thermoplastics, Colloid & Polymer Science 262(4) (1984) 257-269. doi:10.1007/BF01410464
[162] A.P. Eberle, D.G. Baird, P. Wapperom, G.M. Vélez-García, Using transient shear rheology to determine material parameters in fiber suspension theory, Journal of Rheology 53(3) (2009) 685-705. doi:10.1122/1.3099314
[163] S. Mazahir, G. Vélez-García, P. Wapperom, D. Baird, Evolution of fibre orientation in radial direction in a center-gated disk: Experiments and simulation, Composites Part A: Applied Science and Manufacturing 51 (2013) 108-117. doi:10.1016/j.compositesa.2013.04.008

[164] S.M. Mazahir, Improvement in Orientation Predictions of High-Aspect Ratio Particles in Injection Mold Filling Simulations, Doctoral dissertation, Virginia Polytechnic Institute and State University (2013).
[165] K.J. Meyer, J.T. Hofmann, D.G. Baird, Initial conditions for simulating glass fiber orientation in the filling of center-gated disks, Composites Part A: Applied Science and Manufacturing 49 (2013) 192-202. doi:10.1016/j.compositesa.2013.03.004
[166] K. Ortman, D. Baird, P. Wapperom, A. Whittington, Using startup of steady shear flow in a sliding plate rheometer to determine material parameters for the purpose of predicting long fiber orientation, Journal of Rheology 56(4) (2012) 955-981. doi:10.1122/1.4717496
[167] J.M. Dealy, K.F. Wissbrun, Melt rheology and its role in plastics processing: theory and applications, Springer (2012). doi:10.1007/978-94-009-2163-4
[168] K. Hyun, M. Wilhelm, C.O. Klein, K.S. Cho, J.G. Nam, K.H. Ahn, S.J. Lee, R.H. Ewoldt, G.H. McKinley, A review of nonlinear oscillatory shear tests: Analysis and application of large amplitude oscillatory shear (LAOS), Progress in Polymer Science 36(12) (2011) 1697-1753. doi:10.1016/j.progpolymsci.2011.02.002
[169] J.A. Yosick, A.J. Giacomin, P. Moldenaers, A kinetic network model for nonlinear flow behavior of molten plastics in both shear and extension, Journal of non-newtonian fluid mechanics 70(1) (1997) 103-123. doi:10.1016/S0377-0257(96)01535-2
[170] K. Hyun, S.H. Kim, K.H. Ahn, S.J. Lee, Large amplitude oscillatory shear as a way to classify the complex fluids, Journal of Non-Newtonian Fluid Mechanics 107(1) (2002) 51-65. doi:10.1016/S0377-0257(02)00141-6
[171] G. Harrison, G. Franks, V. Tirtaatmadja, D. Boger, Suspensions and polymers-Common links in rheology, Korea-Australia Rheology Journal 11(3) (1999) 197-218.
[172] A.A. Salifu, C. Lekakou, F.H. Labeed, Electrospun oriented gelatin-hydroxyapatite fiber scaffolds for bone tissue engineering, Journal of Biomedical Materials Research Part A 105(7) (2017) 1911-1926. doi:10.1007/s12306-011-0097-8
[173] Y. Chen, C. Xu, J. Huang, D. Wu, Q. Lv, Rheological properties of nanocrystalline cellulose suspensions, Carbohydrate polymers 157 (2017) 303-310. doi:10.1016/j.carbpol.2016.10.002
[174] D.E. Yunus, W. Shi, S. Sohrabi, Y. Liu, Shear induced alignment of short nanofibers in 3D printed polymer composites, Nanotechnology 27(49) (2016) 495302. doi:10.1088/0957-4484/27/49/495302
[175] D.E. Yunus, R. He, W. Shi, O. Kaya, Y. Liu, Short fiber reinforced 3d printed ceramic composite with shear induced alignment, Ceramics International (2017). doi:10.1016/j.ceramint.2017.06.012
[176] T. Inoue, K. Osaki, Rheological properties of poly (vinyl alcohol)/sodium borate aqueous solutions, Rheologica acta 32(6) (1993) 550-555. doi:10.1007/BF00369071
[177] V. Tirtaatmadja, K. Tam, R. Jenkins, Rheological properties of model alkali-soluble associative (HASE) polymers: Effect of varying hydrophobe chain length, Macromolecules 30(11) (1997) 3271-3282. doi:10.1021/ma961202b

[178] S.R. Raghavan, S.A. Khan, Shear-induced microstructural changes in flocculated suspensions of fumed silica, Journal of rheology 39(6) (1995) 1311-1325. doi:10.1122/1.550638
[179] M. Parthasarathy, D.J. Klingenberg, Large amplitude oscillatory shear of ER suspensions, Journal of non-newtonian fluid mechanics 81(1) (1999) 83-104. doi:10.1016/S0377-0257(98)00096-2
[180] J.J. Martin, M.S. Riederer, M.D. Krebs, R.M. Erb, Understanding and overcoming shear alignment of fibers during extrusion, Soft matter 11(2) (2015) 400-405. doi:10.1039/C4SM02108H
[181] A. Ashkin, Acceleration and trapping of particles by radiation pressure, Physical review letters 24(4) (1970) 156. doi:10.1103/PhysRevLett.24.156
[182] L. Johansson, Acoustic manipulation of particles and fluids in microfluidic systems, Doctoral dissertation, Acta Universitatis Upsaliensis, (2009).
[183] A. Setayeshgar, M.G. Lipsett, C.R. Koch, D.S. Nobes, Particle motion in a macroscale, multiwavelength acoustic field, Journal of Fluids Engineering 137(1) (2015) 011302. doi:10.1115/1.4027777
[184] M. Wiklund, R. Green, M. Ohlin, Acoustofluidics 14: Applications of acoustic streaming in microfluidic devices, Lab on a Chip 12(14) (2012) 2438-2451. doi:10.1039/C2LC40203C
[185] M. Settnes, H. Bruus, Forces acting on a small particle in an acoustical field in a viscous fluid, Physical Review E 85(1) (2012) 016327. doi:10.1103/PhysRevE.85.016327
[186] H. Bruus, Acoustofluidics 7: The acoustic radiation force on small particles, Lab on a Chip 12(6) (2012) 1014-1021. doi:10.1039/C2LC21068A
[187] L.V. King, On the acoustic radiation pressure on spheres, Proceedings of the Royal Society of London A: Mathematical, Physical and Engineering Sciences, The Royal Society, (1934), pp. 212-240. doi:10.1098/rspa.1934.0215
[188] M. Ohlin, Ultrasonic Fluid and Cell Manipulation, Doctoral dissertation, KTH Royal Institute of Technology, 2015.
[189] B. Hammarström, T. Laurell, J. Nilsson, Seed particle-enabled acoustic trapping of bacteria and nanoparticles in continuous flow systems, Lab on a Chip 12(21) (2012) 4296-4304. doi:10.1039/c2lc40697g
[190] T. Laurell, F. Petersson, A. Nilsson, Chip integrated strategies for acoustic separation and manipulation of cells and particles, Chemical Society Reviews 36(3) (2007) 492-506. doi:10.1039/b601326k
[191] A. Hancock, Observation of forces on microparticles in acoustic standing waves, Master Thesis, University of California, Davis, 2001.
[192] H. Hertz, Standing-wave acoustic trap for nonintrusive positioning of microparticles, Journal of applied physics 78(8) (1995) 4845-4849. doi:10.1063/1.359770
[193] H. Wu, W. Liu, R. He, Z. Wu, Q. Jiang, X. Song, Y. Chen, L. Cheng, S. Wu, Fabrication of dense zirconia-toughened alumina ceramics through a stereolithography-based additive manufacturing, Ceramics International 43(1) (2017) 968-972. doi:10.1016/j.ceramint.2016.10.027
[194] K. Liu, H. Sun, Y. Tan, Y. Shi, J. Liu, S. Zhang, S. Huang, Additive manufacturing of traditional ceramic powder via selective laser sintering with cold

isostatic pressing, The International Journal of Advanced Manufacturing Technology (2016) 1-8. doi:10.1007/s00170-016-9441-3
[195] J.H. Lee, H.J. Hwang, J.H. Kim, K.T. Hwang, K.S. Han, Ceramic Ink-jet Printing on Glass Substrate Using Oleophobic Surface Treatment, Journal of the Korean Ceramic Society 53(1) (2016) 75-80. doi:10.4191/kcers.2016.53.1.75
[196] J.W. Halloran, Ceramic Stereolithography: Additive Manufacturing for Ceramics by Photopolymerization, Annual Review of Materials Research 46 (2016) 19-40. doi:10.1146/annurev-matsci-070115-031841
[197] J. Jue, D. Gu, K. Chang, D. Dai, Microstructure evolution and mechanical properties of Al-Al 2 O 3 composites fabricated by selective laser melting, Powder Technology (2016). doi:10.1016/j.powtec.2016.12.079
[198] J.P. Deckers, K. Shahzad, L. Cardon, M. Rombouts, J. Vleugels, Shaping ceramics through indirect selective laser sintering, Rapid Prototyping Journal 22(3) (2016) 544-558. doi:10.1108/RPJ-10-2014-0143
[199] R. Sambell, D. Bowen, D. Phillips, Carbon fibre composites with ceramic and glass matrices, Journal of Materials Science 7(6) (1972) 663-675. doi:10.1007/BF00549378
[200] F. Ye, J.M. Yang, L.T. Zhang, W.C. Zhou, Y. Zhou, T.C. Lei, Fracture Behavior of SiC-Whisker-Reinforced Barium Aluminosilicate Glass-Ceramic Matrix Composites, Journal of the American Ceramic Society 84(4) (2001) 881-883. doi:10.1111/j.1151-2916.2001.tb00759.x
[201] W. Nakao, M. Ono, S.-K. Lee, K. Takahashi, K. Ando, Critical crack-healing condition for SiC whisker reinforced alumina under stress, Journal of the European Ceramic Society 25(16) (2005) 3649-3655. doi:10.1016/j.jeurceramsoc.2004.09.021
[202] N. Song, H.b. Zhang, H. Liu, J.Z. Fang, Effects of SiC whiskers on the mechanical properties and microstructure of SiC ceramics by reactive sintering, Ceramics International (2017). doi:10.1016/j.ceramint.2017.02.095
[203] Y. Shi, J.M. Hausherr, H. Hoffmann, D. Koch, Inspection of geometry influence and fiber orientation to characteristic value for short fiber reinforced ceramic matrix composite under bending load, Journal of the European Ceramic Society (2016). doi:10.1016/j.jeurceramsoc.2016.11.042
[204] J.S. Park, H. Nishimura, D. Hayasaka, J.H. Yu, H. Kishimoto, A. Kohyama, Fabrication of short SiC fiber reinforced SiC matrix composites with high fiber volume fraction, Fusion Engineering and Design 109 (2016) 1174-1178. doi:10.1016/j.fusengdes.2015.12.060
[205] P. Hariharasakthisudhan, J. Swaminathan, Characterizing the Compression Behavior of Al2O3/Si3N4 Nano Sized Particulate Reinforced Ceramic Matrix Composites, Indian Journal of Science and Technology 9(43) (2016). doi:10.17485/ijst/2016/v9i43/104586
[206] K. Ahmad, W. Pan, Dramatic effect of multiwalled carbon nanotubes on the electrical properties of alumina based ceramic nanocomposites, Composites Science and Technology 69(7) (2009) 1016-1021. doi:10.1016/j.compscitech.2009.01.015
[207] W.L. Wang, J.Q. Bi, S.R. Wang, K.N. Sun, M. Du, N.N. Long, Y.J. Bai, Microstructure and mechanical properties of alumina ceramics reinforced by boron

nitride nanotubes, Journal of the European Ceramic Society 31(13) (2011) 2277-2284. doi:10.1016/j.jeurceramsoc.2011.05.042
[208] Y. Shi, K. Tushtev, J.M. Hausherr, D. Koch, K. Rezwan, Oxidation Kinetics and Its Impact on the Strength of Carbon Short Fiber Reinforced C/SiC Ceramics, Advanced Engineering Materials 15(1-2) (2013) 19-26. doi:10.1002/adem.201200130
[209] D.E. Yunus, S. Sohrabi, R. He, W. Shi, Y. Liu, Acoustic patterning for 3D embedded electrically conductive wire in stereolithography, Journal of Micromechanics and Microengineering 27(4) (2017) 045016. doi:10.1088/1361-6439/aa62b7
[210] P. He, D. Jia, B. Zheng, S. Yan, J. Yuan, Z. Yang, X. Duan, J. Xu, P. Wang, Y. Zhou, SiC fiber reinforced geopolymer composites, part 2: Continuous SiC fiber, Ceramics International 42(10) (2016) 12239-12245. doi:10.1016/j.ceramint.2016.04.168
[211] A.N. Oumer, O. Mamat, A Review of Effects of Molding Methods, Mold Thickness and Other Processing Parameters on Fiber Orientation in Polymer Composites, Asian Journal of Scientific Research 6(3) (2013) 401. doi:10.1016/j.compositesa.2015.09.003
[212] C. Yang, X.-H. Yin, G.-M. Cheng, Microinjection molding of microsystem components: new aspects in improving performance, Journal of Micromechanics and Microengineering 23(9) (2013) 093001. doi:10.1088/0960-1317/23/9/093001
[213] J. Giboz, T. Copponnex, P. Mélé, Microinjection molding of thermoplastic polymers: morphological comparison with conventional injection molding, Journal of Micromechanics and Microengineering 19(2) (2009) 025023. doi:10.1088/0960-1317/19/2/025023
[214] C. Yang, Flow-induced morphology evolution of uniformly miniaturized high-density polyethylene parts prepared by micro-injection molding, The International Journal of Advanced Manufacturing Technology 68(5-8) (2013) 1745-1755. doi:10.1007/s00170-013-4972-3
[215] J. Sha, J. Li, S. Wang, Z. Zhang, Y. Zu, S. Flauder, W. Krenkel, Improved microstructure and fracture properties of short carbon fiber-toughened ZrB 2-based UHTC composites via colloidal process, International Journal of Refractory Metals and Hard Materials 60 (2016) 68-74. doi:10.1016/j.ijrmhm.2016.07.010
[216] Y. Shi, J.-M. Hausherr, H. Hoffmann, D. Koch, Inspection of geometry influence and fiber orientation to characteristic value for short fiber reinforced ceramic matrix composite under bending load, Journal of the European Ceramic Society 37(4) (2017) 1291-1303. doi:10.1016/j.jeurceramsoc.2016.11.042
[217] W. Mingchao, Z. Zuoguang, S. Zhijie, L. Min, Effect of fiber type on mechanical properties of short carbon fiber reinforced B_4C composites, Ceramics International 35(4) (2009) 1461-1466. doi:10.1016/j.ceramint.2008.07.023
[218] C.J. Bae, J.W. Halloran, Integrally cored ceramic mold fabricated by ceramic stereolithography, International Journal of Applied Ceramic Technology 8(6) (2011) 1255-1262. doi:10.1111/j.1744-7402.2010.02568.x
[219] A. Kazemi, M. Faghihi-Sani, H. Alizadeh, Investigation on cristobalite crystallization in silica-based ceramic cores for investment casting,

Journal of the European Ceramic Society 33(15) (2013) 3397-3402. doi:10.1016/j.jeurceramsoc.2013.06.025
[220] C. Li, Z. Chen, J. Zhu, Y. Liu, Y. Jiang, T. Guan, B. Li, L. Lin, Mechanical properties and microstructure of 3D orthogonal quartz fiber reinforced silica composites fabricated by silicasol-infiltration-sintering, Materials & Design (1980-2015) 36 (2012) 289-295. doi:10.1016/j.matdes.2011.11.022
[221] M. Baghi, B. Niroumand, R. Emadi, Fabrication and characterization of squeeze cast A413-C SF composites, Journal of Alloys and Compounds (2017). doi:10.1016/j.jallcom.2017.03.136
[222] W.J. Chung, J.W. Oh, K. Kwak, B.Y. Lee, J. Meyer, E. Wang, A. Hexemer, S.W. Lee, Biomimetic self-templating supramolecular structures, Nature 478(7369) (2011) 364-368. doi:10.1038/nature10513
[223] S. Lee, S. Shin, S. Lee, J. Seo, J. Lee, S. Son, H.J. Cho, H. Algadi, S. Al-Sayari, D.E. Kim, Ag nanowire reinforced highly stretchable conductive fibers for wearable electronics, Advanced Functional Materials 25(21) (2015) 3114-3121. doi:10.1002/adfm.201500628
[224] Z. Zheng, L. Gan, T. Zhai, Electrospun nanowire arrays for electronics and optoelectronics, Science 59(3) (2016) 201. doi:10.1007/s40843-016-5026-4
[225] X. Duan, C. Niu, V. Sahi, J. Chen, J.W. Parce, S. Empedocles, J.L. Goldman, High-performance thin-film transistors using semiconductor nanowires and nanoribbons, Nature 425(6955) (2003) 274-278. doi:10.1038/nature01996
[226] R. Yan, D. Gargas, P. Yang, Nanowire photonics, Nature Photonics 3(10) (2009) 569-576. doi:10.1038/nphoton.2009.184
[227] G.C. Xu, J. Wang, X.L. Ji, J.Y. Xiong, F. Li, Effect of nano-silicon nitride on the mechanical and electric properties of polypropylene nanocomposite, Journal of Composite Materials 41 (2007) 2213-2223. doi:10.1177/0021998307074185
[228] Z. Guo, T. Pereira, O. Choi, Y. Wang, H.T. Hahn, Surface functionalized alumina nanoparticle filled polymeric nanocomposites with enhanced mechanical properties, Journal of Materials Chemistry 16(27) (2006) 2800-2808. doi:10.1039/B603020C
[229] M. Kirca, A.C. To, Mechanics of CNT Network Materials, Pittsburgh, PA, USA, 2016. doi:10.1002/9781119068921.ch2
[230] J. Yin, M. Retsch, E.L. Thomas, M.C. Boyce, Collective mechanical behavior of multilayer colloidal arrays of hollow nanoparticles, Langmuir 28(13) (2012) 5580-5588. doi:10.1021/la300039v
[231] F. Deng, M. Ito, T. Noguchi, L. Wang, H. Ueki, K.I. Niihara, Y.A. Kim, M. Endo, Q.S. Zheng, Elucidation of the reinforcing mechanism in carbon nanotube/rubber nanocomposites, ACS nano 5(5) (2011) 3858-3866. doi:10.1021/nn200201u
[232] Y. Xia, P. Yang, Y. Sun, Y. Wu, B. Mayers, B. Gates, Y. Yin, F. Kim, H. Yan, One-dimensional nanostructures: synthesis, characterization, and applications, Advanced materials 15(5) (2003) 353-389. doi:10.1002/adma.200390087
[233] S.Y. Fu, B. Lauke, The elastic modulus of misaligned short-fiber-reinforced polymers, Composites science and technology 58(3) (1998) 389-400. doi:10.1016/S0266-3538(97)00129-2
[234] J. Hone, M. Llaguno, N. Nemes, A. Johnson, J. Fischer, D. Walters, M. Casavant, J. Schmidt, R. Smalley, Electrical and thermal transport properties of magnetically

aligned single wall carbon nanotube films, Applied physics letters 77(5) (2000) 666-668. doi:10.1063/1.127079
[235] B. Su, Y. Wu, L. Jiang, The art of aligning one-dimensional (1D) nanostructures, Chemical Society Reviews 41(23) (2012) 7832-7856. doi:10.1039/C2CS35187K
[236] X. Jiang, J. Feng, L. Huang, Y. Wu, B. Su, W. Yang, L. Mai, L. Jiang, Bioinspired 1D Superparamagnetic Magnetite Arrays with Magnetic Field Perception, Advanced Materials (2016). doi:10.1002/adma.201601609
[237] G. Kwak, M. Seol, Y. Tak, K. Yong, Superhydrophobic ZnO nanowire surface: chemical modification and effects of UV irradiation, The Journal of Physical Chemistry C 113(28) (2009) 12085-12089. doi:10.1021/jp900072s
[238] S.G. Rao, L. Huang, W. Setyawan, S. Hong, Nanotube electronics: large-scale assembly of carbon nanotubes, Nature 425(6953) (2003) 36-37. doi:10.1038/425036
[239] Y. Li, Y. Wu, Coassembly of graphene oxide and nanowires for large-area nanowire alignment, Journal of the American Chemical Society 131(16) (2009) 5851-5857. doi:10.1021/ja9000882
[240] P.K. Mallick, Fiber-reinforced composites: materials, manufacturing, and design, Boca Raton, FL, CRC Press (2007). doi:10.1201/9781420005981
[241] M.R. Noordin, K.Y. Liew, Synthesis of alumina nanofibers and composites, INTECH Open Access Publisher (2010). doi:10.5772/8165
[242] Applying a Silane Coupling Agent (Gelest Reference Library) http://www.gelest.com/wp-content/uploads/09Apply.pdf
[243] S. Mason, R.S.J. Manley, Particle motions in sheared suspensions: orientations and interactions of rigid rods, Proceedings of the Royal Society of London A: Mathematical, Physical and Engineering Sciences, The Royal Society, 1956, pp. 117-131. doi:10.1098/rspa.1956.0207
[244] C. Joung, N. Phan-Thien, X. Fan, Direct simulation of flexible fibers, Journal of non-newtonian fluid mechanics 99(1) (2001) 1-36. doi:10.1016/S0377-0257(01)00113-6
[245] K.B. Moses, S.G. Advani, A. Reinhardt, Investigation of fiber motion near solid boundaries in simple shear flow, Rheologica Acta 40(3) (2001) 296-306. doi:10.1007/s003970000135
[246] A. Carlsson, Near wall fibre orientation in flowing suspensions, Department of Mechanics, Doctoral Thesis, KTH Royal Institute of Technology, Stockholm (2009).
[247] H. Ito, Y. Yagisawa, T. Saito, T. Yasuhara, T. Kikutani, Y. Yamagiwa, Fundamental study on structure development of thin-wall injection molded products, Theoretical and Applied Mechanics Japan 54 (2005) 263-268. doi:10.11345/nctam.54.263
[248] J. Chu, A. Hrymak, M. Kamal, Microstructural characteristics of micro-injection molded thermoplastics, Antec-Conf. Proc. (Society of Plastics Engineers) (2007) 1985–9.
[249] Z. Lu, K. Zhang, Morphology and mechanical properties of polypropylene micro-arrays by micro-injection molding, The International Journal of Advanced Manufacturing Technology 40(5-6) (2009) 490-496. doi:10.1007/s00170-007-1364-6

[250] Z. Lu, K. Zhang, Crystal distribution and molecule orientation of micro injection molded polypropylene microstructured parts, Polymer Engineering & Science 49(8) (2009) 1661-1665. doi:10.1002/pen.21167
[251] A. Bellini, S. Güçeri, Mechanical characterization of parts fabricated using fused deposition modeling, Rapid Prototyping Journal 9(4) (2003) 252-264. doi:10.1108/13552540310489631
[252] A. Lee, K. Sudau, K.H. Ahn, S.J. Lee, N. Willenbacher, Optimization of experimental parameters to suppress nozzle clogging in inkjet printing, Industrial & Engineering Chemistry Research 51(40) (2012) 13195-13204. doi:10.1021/ie301403g
[253] Y. Tao, Y. Tao, L. Wang, B. Wang, Z. Yang, Y. Tai, High-reproducibility, flexible conductive patterns fabricated with silver nanowire by drop or fit-to-flow method, Nanoscale research letters 8(1) (2013) 147. doi:10.1186/1556-276X-8-147
[254] H.H. Lee, K.S. Chou, K.C. Huang, Inkjet printing of nanosized silver colloids, Nanotechnology 16(10) (2005) 2436. doi:10.1088/0957-4484/16/10/074
[255] Y. Yang, Z. Chen, X. Song, Z. Zhang, J. Zhang, K.K. Shung, Q. Zhou, Y. Chen, Biomimetic Anisotropic Reinforcement Architectures by Electrically Assisted Nanocomposite 3D Printing, Advanced Materials 29(11) (2017). doi: 10.1002/adma.201605750

Vita

Doruk Erdem Yunus was born in Istanbul, Turkey on November 23, 1986 to Semseddin Yunus and Samira Koc. He received his Bachelor Degree in 2008 in Mechanical Engineering from Ege University. After receiving his Bachelor Degree, he worked in IB-ER Prosthetic Components as a Research and Development Engineer between 2009 and 2011 and also received his Master Degree in 2011 in Mechanical Engineering from Ege University.

After working in industry and attaining Master Degree, he received Ministry of National Education of Republic of Turkey's scholarship for his Ph.D. education and he began his Ph.D. degree in the Mechanical Engineering and Mechanics Department at Lehigh University. He has been working under the supervision of Professor Yaling Liu during his Ph.D. education.